Buoyancy-Driven Exchange Flow with Applications to Architectural Fluid Mechanics

by

Saleh Nabi

A thesis submitted in partial fulfillment of the requirements for the degree of

Doctor of Philosophy

Department of Mechanical Engineering
University of Alberta

Abstract

Buoyancy driven flow between two finite zones containing fluid of slightly different density is investigated. Two zones separated by (i) a single common doorway, and, (ii) top and bottom vents.

In the former case, a two-layer exchange flow develops once the barrier is removed. In the zone that initially contained dense fluid, a buoyant plume of light fluid mixes with the dense fluid leading, over time, to the development of non-trivial ambient density stratification. Meanwhile, dense fluid flows as a gravity current into the zone that initially contained light fluid. This gravity current reflects from the end wall and propagates back toward the opening in the form of an internal bore. When the bore reaches the opening the dynamics of the exchange flow are substantially altered. Such coupled dynamics of the two zones are modeled using elements of gravity current, internal bore and plume theory. Depending on the geometric parameters two scenarios are possible. Either the terminal position of the first front lies above the bottom of the barrier, or it lies below. In the latter case, the associated complications are (i) the nature of the exchange flow changes once the downward-propagating first front surpasses the bottom of the barrier, and, (ii) the terminal stratification in the zone that initially contains the light fluid now includes an intermediate layer. We also present a model that presumes that both zones remain well-mixed.

When the two zones are separated by top and bottom vents, two oppositely directed exchange flows are generated. The transient evolution of the interface, stratification and buoyancy in each zone are estimated both for the case where the light zone does and does not contain a source of buoyancy. Attention is focused

on the influence of the effective area, source buoyancy flux and the time during which the source is switched on.

Similitude experiments help to identify the limitations of the analytical models for each scenario. The implications of our results on the design of multi-zone buildings that exploit passive heat gains are also discussed.

Preface

This thesis is an original work by Saleh Nabi. The technical apparatus referred to in Chapters 2, 3 and 4 was designed by myself, with the assistance of Dr. M.R. Flynn and University of Alberta, Department of Mechanical Engineering Technical Resources Group.

Chapter 2 of this thesis has been published as S. Nabi, M.R. Flynn, "The hydraulics of exchange flow between adjacent confined building zones," Journal of Building and Environment, vol. 59, 2013, 56-90. Chapter 3 of this thesis has been published as S. Nabi, M.R. Flynn, "Influence of geometric parameters on the eventual buoyancy stratification that develops due to architectural exchange flow," Journal of Building and Environment, vol. 71, 2014, 33-46. I was responsible for the data collection and analysis as well as the manuscript composition. M.R. Flynn was the supervisory author and was involved with concept formation and manuscript composition.

Mathematics reveals its secrets only to those who approach it with pure love, for its own beauty. Of course, those who do this are also rewarded with results of practical importance.

- ARCHIMEDES

To my mother, Farahnaz, and my father, Mohammad, for their eternal love and support

Acknowledgements

First and foremost, I would like to extend my sincere thanks to my supervisor Dr. Morris Flynn for his exceptional guidance in the completion of this thesis. After years of continuous research, I can't think of a moment that I ask for his assistance and my request is not ensued by an insightful and productive meeting. His dedication to research and his expertise in various aspects of theoretical and experimental fluid mechanics has been a source of inspiration and motivation throughout the course of my Ph.D.

I also enjoyed several mind provoking discussions with Dr. Bob Koch and Dr. Sushanta Mitra, through our committee meetings. I had the opportunity to have infrequent communications with Dr. Andreas Athienitis through SNEBRN annual meetings. I owe much gratitude to many professors at University of Alberta, explicitly Dr. Richard Craster (now at Imperial College of London), Dr. Bruce Sutherland, and Dr. Tian Tang.

A big shout out to all my fellow students with whom I have shared this big adventure. The wonderful people who patiently listened and helped me with my many and never ending questions. You know who you are! The assistance of the University of Alberta, Department of Mechanical Engineering Technical Resources Group is also acknowledged with thanks.

Financial support for this study was provided by NSERC through the Discovery Grant Program and also through the Smart Net-zero Energy Buildings Strategic Research Network. As a recipient of Sadler Graduate Scholarship in Mechanical Engineering and RR Gilpin Memorial Scholarship, I should thank the Sadler and Gilpin families for their generosity.

Finally, I searched for the words that can convey my feelings toward my family and loved ones. I could not find such words…

Table of Contents

List of Tables

List of Figures

List of Symbols

Symbols

A^*	effective area (m^2)
b	non-dimensional buoyancy
b_p	effective half-width of the plume (m)
C_d	discharge coefficient
Cr	Courant number
D	diameter
$g_0{}'$	initial reduced gravity (m^2/s)
g'	reduced gravity (m^2/s)
Fr_1	Froude number (dense gravity current)
Fr_2	Froude number (light gravity current)
Fr_b	Froude number (internal bore)
h	height of removal (m) (in Chapters 2 and 3)
	vertical distance between the bottom of the bottom vent and the floor (m) (in Chapter 4)
I	terminal buoyancy of the intermediate layer
h_b, h_t	interface height (m) in light and dense zone, respectively
k	function in exchange flow equation (3-16)

Q_s	source buoyancy flux (m^2/s)
Q_e, F_e	exchange volume (m^2/s) and buoyancy (m^3/s^3) flux per unit width
N_b, N_t	number of bottom and top open vents, respectively
P	pressure (Pa)
R	non-dimensional distance indicating the terminal elevation of the first front
t	time (s)
t_E	ending time (s)
t_1	time taken for the gravity current to reach to the end-wall (s)
t_2	time taken for the internal bore to reach the doorway (s)
t_3	time taken for the first front to reach the top of the doorway (s)
t_s	time during which the source is switched on (s)
T_0, T_c	initial temperature of the dense and light zone (K), respectively
U	velocity of the descending layers in the dense zone ambient (m/s)
α	entrainment coefficient

λ	empirical factor for density profile within plume
ρ	density (kg/m^3)
ρ_{00}	reference density (kg/m^3)
ℓ	lock length (m)
H, L, W	height, length and width of the rooms (tank), respectively (m)
$Q,$	volume (m^2/s), momentum (m^3/s^2) and buoyancy (m^3/s^3) flux within plume, respectively
$M,$	
F	
u_{01}, h_{01}	velocity (m/s) and depth (m) of the bottom layer at doorway, respectively
u_{02}, h_{02}	velocity (m/s) and depth (m) of the upper layer at doorway, respectively
u_1, h_1	dense gravity current velocity (m/s) and depth (m), respectively
u_2, h_2	light gravity current velocity (m/s) and depth (m), respectively
u_b, h_b	internal bore velocity (m/s) and depth (m), respectively
x, z	horizontal and vertical coordinates (m)
$\bar{w}, \Delta$	characteristic axial velocity (m/s) and reduced gravity (m/s^2) within plume,

	respectively
ρ_a	density (kg/m^3) and reduced gravity (m/s^2) of the ambient, respectively
Δ_a	
Π_s	source strength
τ	characteristic draining time
z_{bal}	elevation where the plume goes to zero buoyancy flux (m)
z_{ff}	elevation of the descending first front (m)

Subscripts

0	dense zone
wm	well-mixed
c	light zone
tot	total

Superscripts

f	final state
∞	terminal quantity

Chapter 1

Introduction

1.1 Background and motivation

The built environment is a primary consumer of energy and contributor of greenhouse gas (GHG) emissions in North America. In Canada, about one-third of GHG emissions and about one-half of electricity consumption are attributed to buildings [1]. The environmental demands and limited sources of energy urge us to find new strategies for energy savings in buildings. Thus exceptions to Santamouris' observation that “energy consumption defines the quality of urban life…” [2] need to be found and exploited. As though to underscore the point, the Canada Mortgage and Housing Corporation [3] carried out a survey in 2004 to assess the benefits of ventilation systems in new Ontario houses. They found that "in mid-summer, almost 10% do not open windows at all, which may indicate continuous use of air conditioning systems. These houses would benefit from mid-summer ventilation to provide fresh air".

We spend about 90% of our lives indoors. Poor indoor air quality (IAQ) has been linked to lung diseases and affects other parts of the body [4]. Improvement of indoor environmental quality and comfort increases the productivity of occupants and provides an inviting healthy environment. Moreover, it is a common phenomenon that people find it necessary to dress more warmly in air-conditioned buildings in the summer than they would if they were outside. In such cases, mechanical ventilation systems produce an uncomfortable environment for occupants in some circumstances. Aside from concerns about building energy efficiency and climate change, enhancing indoor air quality is also an important task to be addressed by architectural fluid dynamists [5].

In this spirit, the building industry must accommodate three interrelated objectives: (i) reduce and optimize the energy required for heating, cooling, ventilation; (ii) increase IAQ and comfort for building occupants; (iii) promote sustainable design through the use of environmentally friendly and renewable energy sources.

In light of the above objectives, there are many strategies for improving architectural design and practice, among which the importance of passive solar design is well-recognized [6]. Passive solar design encourages the adaptation of architectural strategies such as using wide south-facing windows and attached solaria [7, 8]. However, making efficient use of the heat collected by solaria by redistributing this heat to other zones within the building requires a detailed understanding of architectural exchange flow.

Buoyancy-driven flows arise due to inevitable temperature disparities between building zones which in turn result from a difference of zone orientation relative to the sun or because of heat-generating electrical devices in one zone but not another. The dynamics of buoyancy-driven flows between two interior zones are, as we shall demonstrate, tightly linked to thermal plumes. Knowledge of the mixing processes associated with plumes is therefore important for the proper design of air-conditioning systems or for increasing the efficiency of natural ventilation (Linden [9]; Liu et al. [10]; Linden et al. [11]).

Moreover, as indicated by Fang et al. [12, 13], people perceive the same air as being of poor quality in a warm condition but of better quality at lower temperature. Hence, knowledge of the time evolution of the temperature profiles within a given building zone has an impact both on IAQ and also energy performance [14].

Caulfield and Woods [15] identify a pair of other industrial examples of flows due to buoyancy forces within (industrial) buildings, namely the storage of liquid natural gas or of liquid chlorine, which is used to purify water; both are volatile fluids stored under pressure. If a rupture occurs in the storage network, the liquid vaporizes and the so-produced gas then represents a threat to workers. Knowledge of mixing in such process is vital for (i) evaluating the amount of the contaminated air which may escape through the vents located in the building and (ii) informing decisions concerning gas detector placement. Another example for architectural interest includes the ventilation of smoke from a fire (Merci and Maele [16]). Fires generate hot gases and other combustion products, usually at temperatures above 1000ºC. The low density of the hot gases produce strong buoyancy forces, which carry particles and smoke far away from the fire itself. After reaching the ceiling, the smoke plume spreads as a gravity current and afterwards fills the room as a filling box flow [17]. For purposes of adequate fire safety planning it is important to estimate how quickly the smoke fills the space and also how the concentration of smoke in the occupied zone changes with time (Rooney and Linden [18]).

Motivated by such applications, there has been substantial interest in understanding the details of buoyant convection from isolated or distributed sources. In their classical work, Morton et al. [19] proposed a quantitative model for the dynamics of a Boussinesq buoyant turbulent plume and tested it against laboratory experimental data. In contrast to our focus here, they assumed that the ambient density remains constant in time, i.e. the environment is effectively infinite compared to the scale of the plume flowing through it. However, if the ambient is not infinite, this assumption cannot be applied. Fluid which has been in the plume soon spreads out along the ceiling and modifies the ambient, and due to

re-entrainment, it changes the behavior of the plume. Thus, a time-dependent solution which takes into account the interaction between the buoyant plume and the evolving ambient is required. Baines and Turner [17] proposed a "filling-box" model in which the details of such an interaction are outlined. They solved the governing equations asymptotically and described the late time stratification assuming that the buoyancy inside the control volume increases linearly in time. Worster and Huppert [20] further developed the model due to Baines and Turner [17] and presented an approximate analytical expression for the density profile in a filling box as it evolves with time.

In both the works of Worster and Huppert [20] and Baines and Turner [17] however, the source is assumed to be ideal, i.e. the source volume flux is zero. In many real problems, the source of buoyancy may also involve a source of mass. Germeles [21] introduced a numerical scheme to solve the governing equations for both the plume and the ambient, in the case of such non-ideal plume. His approach gives the ambient density profile as a function of depth and time. Caulfield and Woods [15], using Germeles's numerical scheme, have considered the flow within an enclosed space with a single vent and a localized continuous source of buoyant fluid which is modeled as a plume. Kuesters and Woods [22] examined an enclosed volume of buoyant fluid connected to the exterior through two openings at the top of enclosure. An exchange flow is established, with the outflow through one opening being matched by an equal and opposite inflow through the other. They proposed a mathematical model to quantify these effects and validated their model with laboratory experimental results.

In all of the above studies, the interior consists of a single zone. In the architectural case, however, buildings rarely are single interior spaces. On the contrary, buildings are typically characterized by multiple rooms and corridors. Therefore, it is of interest to investigate the exchange flow between two building zones connected through an opening. Extending the work of Linden et al. [11] on the ventilation in a single space, Lin and Linden [23] developed a model for the ventilation of two chambers of equal height connected by two openings, one located at the bottom of the space and the other at the top. They also investigated

the effect of a heat source, modeled as a turbulent plume, on the mixing process and presented experimental results to compare with their theoretical model. When, as with Lin and Linden [23], building zones are connected by two (or more) openings, the flow through any individual opening can typically be modeled as unidirectional. If, however, there is only a single opening, then a bi-directional exchange flow must result. This case is more complicated because the exchange flow is a two-layer flow and one therefore needs to determine the velocity and depth of each layer. Moreover, Lin and Linden [23] did not explicitly consider the horizontal flows in their study. Finally, Lin and Linden [23] assume that both zones have the same density at the initial instant. In practice, the two zones may have different initial temperatures which, as we shall argue below, can contribute significantly to the exchange flow.

In light of the gaps of knowledge identified above, our principal objective is to model the exchange flow between two interior building zones. These are separated by a doorway or a number of top and bottom vents. Due to the complexity of the flow, we decompose the problem into various elemental pieces such as a turbulent plume, internal bore, gravity current and volumetric exchange flow. In this spirit, we construct a composite model consisting of various elements studied by others e.g. Baines and Turner [17] who developed the theory for describing evolution of density in a confined region, Germeles [21] who devised a an efficient numerical scheme to solve the filling box equations, Benjamin [24] who proposed an analytical model for the propagation of the gravity current(s) and Klemp et al. [25] who studied the motion of the internal bore. We modify the associated governing equations as necessary to ensure that they are consistent with the physics of our particular circumstance, which entails a dynamic coupling between the adjacent zones. In the absence of a composite approach of the type studied in this thesis, it is unlikely that the predictions of the lower-order model(s) would accurately describe the transfer of buoyancy from one zone to the other. The specific research gap our work aims to fill is to analyze better the flow rates, stratification and buoyancy distribution for a two zone building separated by a doorway or a pair of top and bottom vents. As independent parameters, we shall

focus much attention on those related to geometry e.g. the doorway height, the relative length of the two zones, the number of top and bottom vents, and the height of the building.

1.2 Methodologies for modeling air flow in confined zones

If the goal of ventilation is to create a thermally comfortable environment with suitable IAQ, it is essential to have the appropriate tools to be able to predict ventilation performance and the associated energy costs. This section provides an overview of those methods for predicting ventilation performance, i.e. analytical models, small-scale (similitude) experiments, full-scale experiments and Computational Fluid Dynamics (CFD) [26].

Before outlining the methodologies, it is necessary to define some terminology for a ventilation problem. For simplicity, and consistent with Linden et al. [11], we shall here consider a single zone building, however, the underlying ideas and terminology may easily be applied to more complicated geometries as we demonstrate later. Depending on the position and number of vents, two types of ventilation flow between an interior and exterior may arise, namely mixing and displacement ventilation -- see Figure 1-1 [9]. If the outside temperature is colder (warmer) than that of the interior, by opening a single opening at the top (bottom) of the building zone the buoyancy forces cause cold (warm) exterior air to descend (rise) within the interior. This air mass will accumulate in the lower (upper) part of the space. This type of ventilation, which is characterized by nearly uniform temperature stratification and a two-layer exchange flow through the vent, is referred to as mixing ventilation. In contrast, if the interior is connected to the cold (warm) environment by means of upper and lower vents, there will develop two opposite unidirectional flows; the warm (cold) air of the interior leaves the space through the upper (lower) vent while it is replaced by exterior cold (warm) air that flows through the lower (upper) vent. A stable density interface forms between the warm, upper layer and the cooler, incoming air. This type of ventilation is referred to as displacement ventilation.

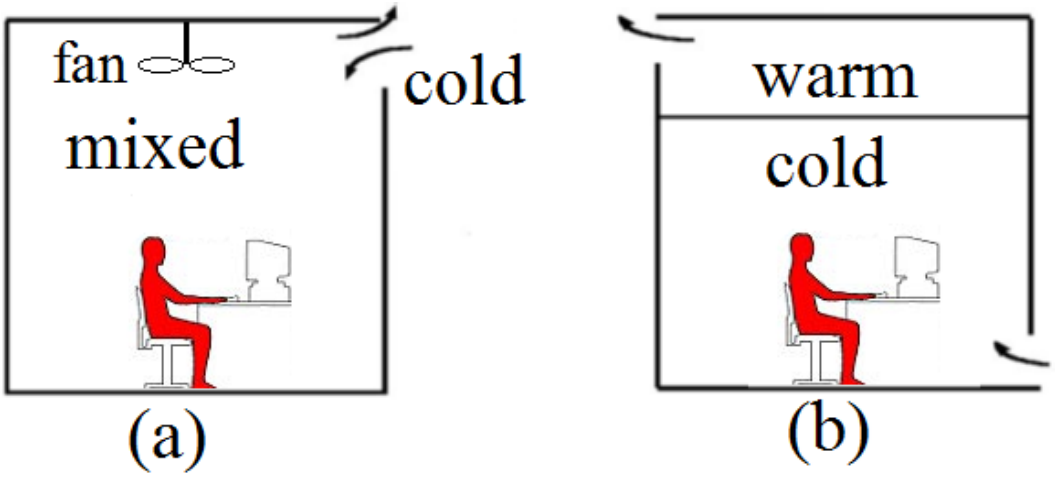

Figure 1-1. Schematics of mixing ventilation (a) and displacement ventilation (b). Based on Figure 1 of Linden [9]. In panel (a) a fan is added to Linden's original figure to emphasize that the zone remains well-mixed during the exchange of interior with the outside.

1.2.1 Analytical models

Analytical models are derived from the fundamental equations of fluid mechanics and heat transfer, such as the mass, momentum, energy, and chemical-species conservation equations. However, to make the equations mathematically tractable, these models often use simplifications of both building geometry and flow properties in order to obtain a closed-form solution.

In case of displacement ventilation with no internal source of buoyancy, the room air is, after a finite time, fully drained and is replaced with the exterior ambient air. Linden et al. [9] derived an analytical equation to calculate such an ending time for a single building zone, which depends on top and bottom vent areas, cross sectional area and depth of the building zone.

Conversely, by including a single source of buoyancy, a steady state interface develops. Sandberg and Lindstrom [27, 28] and Linden et al. [11] showed that, pressure differences between the exterior and interior produce a natural flow that leads to a simple stratification comprising two layers separated by a horizontal interface.

Qualitatively similar ventilation states are realized if the single source is replaced by n sources of equal strength [9, 11]. However, if there are n sources of buoyancy of unequal strength, $n + 1$ well mixed layers will develop in the room at steady state with each plume terminating in its corresponding layer [29]. Thus, the source with the largest value of the buoyancy flux ascends to the highest layer while the source with the smallest value for the buoyancy flux ascends to the lowest layer.

There are many situations, especially involving solar gains, where the sources of buoyancy are distributed over a surface. When the surface is horizontal certain key details of stratification due to single source of buoyancy can be adopted with only minor modifications [30].

The models described above only focus on the properties of the terminal state and therefore ignore the transient evolution of the interface in the zone. This is a nontrivial simplification: if one wishes to compute the steady state interface height, it can be shown that this parameter depends only on the areas of the top and bottom vent and the cross-sectional area and the height of the building. The source parameters do not come into play.

Kaye and Hunt [31] studied the initial transient that associated with an 'emptying filling box' which consists of a control volume with top and bottom vents and a source of buoyancy along the floor. They identified two important time scales: the filling box time, representative of the time taken by discharged plume fluid to fill the control volume; and the draining box time, representative of the time required for a ventilated box to drain the buoyant fluid. They showed that the steady-state elevation of the interface depends on the ratio of these two timescales, which are themselves functions of geometrical parameters, e.g. the room height, cross-sectional area and number of open vents, as well as the strength, number and distribution of the sources of buoyancy.

In the above models, it is assumed that these separate layers remain well mixed. Stratification in realistic cases does not generally exhibit a sharp change in density between two internally well-mixed layers as presumed above. Instead, a more gradual variation of stratification is observed from the bottom, to the top of

the control volume [32-34]. Thus there is a benefit to employing models that can account for such a continuous stratification of fluid density, particularly if one is interested in the early time evolution [35].

Regarding the exchange flow that develops between interior and exterior, a seminal theoretical and experimental work is that of Brown and Solvason [36, 39]. They considered a rectangular opening in a vertical wall and introduced a discharge coefficient to account for the deviation of the actual exchange flow rate from its maximum (ideal) value. Such a deviation is due, say, to cross-stream mixing in the counterflowing shear layer or viscosity effects. Similar results were obtained by others, e.g. Shaw and Whyte [38] and Linden and Simpson [39], most of which are applicable to an opening with symmetrical geometry. Dalziel and Lane-Serff [40] showed that the flow at the opening is critical (and maximal).

Although most of the papers described above fall under the category of "classical studies", similar methodologies continue to be applied in contemporaneous investigations. In particular, the analytical approach continues to offer simplicity, rich physical meaning, and modest computational requirements. To highlight more recent advances, a brief literature review is provided below that deliberately samples different aspects of buoyancy-driven ventilation flows.

Chenvidyakarna and Woods [41] studied the natural ventilation between an occupied interior with the ambient through top and bottom vents. Occupants are modeled as heat sources each with constant buoyancy flux. They posed two important questions regarding the associated buoyancy-driven exchange flow with the exterior: (i) what flow regimes are possible depending on the geometrical parameters, e.g. the plan area or relative position and area of the vents? (ii) In each regime, what is the rate of ventilation and how can one estimate the temperature profiles at steady state? Regarding the former question, they identified three regimes of exchange flow at steady state. For each regime it was possible to predict the temperature profile in the space.

Fitzgerald and Woods [42] investigated the steady state ventilation of an enclosed space containing two vents that are above the floor level. One vent is

connected to the (infinite) exterior via a stack of a finite length while the other is connected directly to the outside. To account for the impact of the heat source within the building, Fitzgerald and Woods [42] considered both distributed and point sources of buoyancy at the floor. In case of a distributed source, they characterized three regimes of exchange flow depending on the relative height of the two vents and the length of the stack. They found that if the vent connected to the stack is above the other vent then there is a unique exchange flow while for the opposite case two further regimes of exchange flow are possible. Regarding the point source of buoyancy, however, the problem is more complicated and they identified seven different exchange flow regimes. In each case, exchange flow rates and stratification profiles are obtained. Moreover, Fitzgerald and Woods [42] developed closed-form expressions in terms of building height and the vent and stack areas, to predict the transitions between these flow regimes.

Coffey and Hunt [43] developed different analytical models for calculating the ventilation effectiveness, which is defined as the ability of a flow to flush buoyancy from a ventilated space be it well mixed or stratified. They extended their research in a follow up study [44] and identified four flow patterns (one- or two-layer flow through the openings with weak or string interfacial mixing) for the case where buoyant fluid drains from a confined zone into a quiescent ambient. They found that the three most important geometrical parameters are the ratio of initial layer depths (in case the interior is initially stratified with cold fluid underlying hotter fluid), the effective vent area and the horizontal length scale of the top opening relative to the initial dense layer depth. They considered the transient evolution of the interface until it reaches steady state. Coffey and Hunt [43] showed that their predictions of interface height converges to the predictions of Linden et al. [11] provided that the interior is initially well-mixed.

Aside from the stack flow problem, analytical models are also developed to address questions concerning other realms of ventilation. For instance, Holford and Woods [45] used analytical models to study the thermal buffering of naturally ventilated buildings containing internal thermal mass. In a well-insulated

building, the function of thermal mass is to even out temperature variations due to solar gains, which have a more intense and variable pattern. A thermal mass thus acts as a heat sink during the day. Stored heat is released to the interior after the sun has set to regulate interior conditions. They solved the conduction problem through the thermal mass imposed by a harmonic variation in the environmental temperature. They further characterized the important time scales caused by various heat transfer processes in the space and discovered how each parameter impacts the fluctuations in the interior temperature. Such information is useful in guiding the application of thermal buffering material in order to minimize the temperature fluctuations perceived by the occupants.

The solar chimney design entails absorbing solar gains and thereby producing an air breeze inside the space. By analyzing chimney-assisted ventilation, Bassiouny and Koura [46] obtained a simple relationship between solar intensity and room air temperature. Bassiouny and Koura [46] investigated the influence of the chimney inlet size and width on the space ventilation. They found that chimney width has a greater influence on flow rate compared to the inlet area size.

Because of the importance of understanding the details of the indoor environment vis-a-vis indoor air quality, Bolster and Linden studied the steady state [47] and transient [48] transport of particulate contaminants in a displacement-ventilated space. Analytical models were developed to compare the average efficiency of contaminant removal between traditional and modern low-energy systems. It was found that whereas the spatially-averaged concentration of particles for traditional mixing systems (with one vent for the ventilation) and low energy displacement systems (with multiple vents for ventilation) are similar, local concentrations vary significantly.

To conclude this sub-section, we now focus on the relevance of the research to analysis and modeling of sunspaces. Shearer and Porteous [49] provided field evidence that attached sunspaces can be net energy contributors in moderate climates such as Scotland, even in winter season with low solar gains. Mottard and Fissore [50] provided reports of models of sunspaces validated with

full-scale field data. In particular, Mottard and Fissore [50] considered radiation exchanges in the long infrared and the distribution of solar radiation in the sunspace. They also included the conduction through the wall. They showed that the view factor weighted approach is not adequate for modeling building zones for which a large fraction of the incident solar radiation eventually is lost, e.g. in spaces that have highly-glazed windows.

Oliveti et al. [51] calculated the solar gains of the sunspace and the adjacent air-conditioned zones for some Italian localities. The parameters they considered are the exposure, the optical properties and the thermal capacity of the opaque surfaces, the capacity of ventilation and the shading equipment. Using their numerical solution to the optical problem of incident solar radiation absorption through the windows, the operative temperature of the sunspace was determined considering the thermal comfort of occupants at the adjacent spaces.

However, the above works did not consider the air flow patterns with the level of details that are achieved by using filling-box type's solutions. For instance, Mottard, and Fissore [50] used the Newton's law of cooling, which depends only on the convective heat coefficient and the average temperature differences of the two zones. Such modeling is equivalent to approaches that assume both zones remain well-mixed and does not take into account the zonal stratification. Therefore, as we see in Chapters 2 and 3 (for the exchange flow with bottom doorway between the two adjacent zones), many important features such as the sudden change in the exchange flow once the internal bore reaches the doorway or, as we see in Chapter 4 (for the exchange flow with top and bottom vents between the two adjacent zones and in the presence of a source of buoyancy), the stratification induced in the dense zone after a finite time cannot be described by their analysis. Likewise, the dynamics of horizontal currents (the bottom and top gravity currents or the internal bore) have not been considered in any of the works cited above. Nonetheless, their analysis can be incorporated with filling-box type modeling to give a more realistic description of the problem insofar as the radiation is considered.

1.2.2 Experimental models

At full scale, high quality measured data can be difficult to obtain due to the complexity of airflow patterns associated with building ventilation. This is more pronounced for in-situ measurements where experimentalists may not even know the boundary conditions in their tests [26]. (In-situ experiments are those carried out in large indoor environments such as theatres or athletic halls, which are heavily instrumented to measure the quantities of interest [52]). Moreover, full-scale experiments can be very expensive and time consuming to construct and may not even be practical.

Small-scale experiments are much more economical and can, if conducted carefully, still offer meaningful quantitative data for full-scale design. An appropriate caution was, however, added by Linden [9]. He noted that carrying out bench-top experiments for naturally ventilated buildings is more difficult than for mechanically forced buildings because of the increased effects of viscosity at small scale. In order to solve this problem, a group at the University of Cambridge developed the methodology of small-scale modeling using water as the working fluid [11, 53]. Density differences are then created by adjusting the salt content rather than the temperature of the water. The rationality behind this approach is as follows: the buoyancy force can be expressed in terms of the reduced gravity, g', defined as $g' = g\,\Delta\rho/\rho$ with g as gravity and ρ as density [9]. If we assume that compressibility is weak so that the density is only a function of temperature, the density variation is linearly proportional to the temperature disparity in the flow field. The reduced gravity can then be expressed as $g' = g\frac{\Delta\rho}{\rho} = g\frac{\Delta T}{T}$ where T, is measured in Kelvin. The relevant dimensionless parameters are the Reynolds number $\mathrm{Re} = \frac{UH}{\nu}$ and the Peclet number $\mathrm{Pe} = \frac{UH}{\kappa}$, where ν and κ are the kinematic viscosity and thermal diffusivity, respectively, and U is the (buoyancy) velocity, which scales as $\sqrt{g'H}$ and H is the height of building. Hence, $\mathrm{Re} = \frac{\sqrt{g'H}H}{\nu}$ and $\mathrm{Pe} = \frac{\sqrt{g'H}H}{\kappa}$. If both Re and Pe have values larger than 10^3 the flow can be considered to be independent of viscous and diffusive effects. Provided reduced-

scale experiments are run in this parametric regime, they are therefore dynamically similar to real architectural flows [9, 57]. Water is used as the working fluid because the corresponding values of ν and α are smaller than for the associated air flow; in addition, it is easy to achieve relatively large values of g'. Moreover, flow visualization is easier in case of water, say, by adding dye or food coloring. In addition to saline and fresh water, select researchers have used hot and cold liquids [61, 37], or gases [63] as the working fluid. In the latter case in particular, however, matching the relevant non-dimensional numbers is always a challenging task [26, 37].

Mott and Woods [65] investigated the natural displacement ventilation of a space connected to a body of warm fluid through high- and low-level vents. The space was also exposed to periodic gusts of wind entering at high level from a cold exterior. Due to temperature difference between the cold wind and the air in the building zone, they simulated gusts of wind with identical turbulent buoyant thermals that were added at regular intervals in their numerous water bath laboratory experiments. As an implementation of their study, they discussed how the results could be used for the ventilation of a shopping mall subject to gusts of wind. Their experimental results confirmed that the steady state interface height depends on the frequency and average buoyancy flux of wind gusts, and the top and bottom vent area.

Fitzgerald and Woods [66] focused on a ventilated room with a distributed heat source and accounted for the effect of penetrative entrainment across two layers. They illustrated that three different ventilation modes may develop depending on the initial temperature of the room relative to the final equilibrium temperature and the exterior temperature. In order to simulate the impact of a heat source they added a heater to their experimental setup. Hence, they supplemented their salt bath experiments with thermocouple measurements to record the temperature of water as a function of time. The shadowgraph technique was used as the visualization method.

Chenvidyakarn and Woods [61] investigated the transient natural ventilation of a warm room connected to a cool exterior through an upper stack on

the ceiling, and into which air is drawn through a lower vent connected to a cooling unit beneath the room. They carried out analogue experiments to observe the transient draining of a room with pre-cooling using the salt-bath technique. The results from their proposed analytical model and the small-scale model were in close agreement.

Livermore and Woods [62] used a similar experimental technique to study the natural ventilation of a building with heating at multiple elevations. The experimental prototype consisted of a small acrylic tank of height 31 cm with two floors connected to a common space, which may resemble a tall atrium. A shadowgraph technique enhanced by tracer dyes was used to measure the flow direction and magnitude through the openings and within the tank.

With several 1:10 scale models, Morsing et al. [63] determined the effects of internal airflow and floor design on gaseous emissions from animal houses. In their paper, and using ammonia as a tracer gas emissions, the results of experiments with different floor layouts were presented and their impact on the resulting bulk airflow patterns discussed.

Phillips and Woods [64] analyzed the exchange flow between an interior space and the external ambient through a single doorway. They carried out similitude experiments that characterized the room filling time as a function of the doorway and room geometry. They concluded that in typical buildings 5–100 min is required for the exchange flow to fill a room once a door has been opened. They also examined the impact of the buoyancy source on the interface height. According to Philips and Woods [64], the depth of this interface depends on the ratio of the width to length of the doorway, but may typically extend over one-half of the doorway height.

1.2.3 CFD models

Computational Fluid Dynamics (CFD) algorithms numerically solve the Navier–Stokes equations, i.e. conservation of mass, momentum and energy.. Advanced numerical techniques also include conservation of chemical-species in case of air pollution investigations. Many important parameters related to internal and external flows within and around buildings are resolved by CFD analysis,

including air pressure, air velocity, air temperature, the concentrations of water vapor (relative humidity) and contaminants, and turbulence parameters [67, 41].

Commercial software such as FLUENT [68] or CFX [69], as well as open source package such as OpenFOAM are also popular among researchers and practitioners. For instance, Abantoa et al. [70] numerically studied air flow and predicted comfort properties in the visualization room of a research centre using FLUENT. They solved the aforementioned conservation equations along with equations that parameterized the influence of clothing insulation and metabolic activity measures to obtain standard indoor air quality indices such as the mean age of air, the predicted mean vote (as a recognized thermal comfort model) and the predicted percentage of dissatisfied room occupants. Using commercial software allowed them to consider relatively fine details, which, in turn, resulted in greater simulation accuracy.

Turbulent flows are associated with fluctuations in the key flow parameters such as velocity, temperature, density, etc. Turbulent fluctuations occur over a wide range of length and time scales. The large scales can be of the order of length scale of the problem, which in the case of flow within buildings can be quite significant. On the other hand, fluctuations may be as small as the Kolmogorov scale (with high frequency), which is sub-millimetric. This variation of length scale signifies that finely-resolved numerical simulations will be expensive to determine in terms of the required computational resources [71]. Correspondingly, the equations are oftentimes time-averaged (or otherwise manipulated) to remove the small scales, leading to a modified set of equations that are computationally less taxing to solve. As a result of such averaging, however, additional unknowns emerge in the modified equations and turbulence closure schemes are needed to determine these variables in terms of other known quantities. In the context of ventilation modelling, the two most widely applied two equation closure schemes are the standard $k-\epsilon$ model [70] and the RNG $k-\epsilon$ models [72].

Choosing the appropriate closure equations typically necessitates a systematic parametric study to be completed. Of course, various efforts have been

made in this direction such as buoyancy-modified RANS models, Algebraic Reynolds Stress Model (ASM), ASM and $k-\epsilon$ hybrids, and the $k-\epsilon$ turbulence model (see Chung and Devaud [77]). Others have also attempted to apply Large Eddy Simulations (LES) to model turbulence [74, 46]. Zhai et al. [76] reviewed popular turbulence models that could be used for indoor environment modeling.

However, an overarching conclusion to be drawn from Chung and Devaud's discussion is that different techniques yield different degrees of physical realism and so special care needs to be applied in the choice of both closure scheme and associated parametric values. Commercial or home-made codes may also become unstable and the solutions are not unlikely to converge or they produce unreliable output for flows that are very strongly stratified (Versteeg and Malalasekera [78]). This is mainly because the impact of buoyancy on the dissipation rate, ϵ, is not fully understood yet (see ANSYS FLUENT Theory Guide, Release 14.0, November 2011, P. 59). In addition, three-dimensional numerical simulations, even those which model the turbulent time and length scales instead of resolving sub-grid eddies and so employ a coarse numerical grid require significant computational resources and therefore remain prohibitively time-consuming in many cases. The computational cost is of course more problematic when a time-critical simulation or a fast on-demand prediction is desired [79, 57].

1.3 Thesis Outline and Scope

In Chapter 2, the hydraulics of a Boussinesq two-layer exchange flow between two finite regions is considered both theoretically and experimentally. The key highlights follow.

- The exchange flow between building zones of different temperature is modeled.
- We study the transient, coupled evolution of the zonal density profiles.
- The density jump across the first front decreases abruptly after a certain point.
- Similitude laboratory experiments are conducted for validating model predictions.

- Good agreement with experiments is noted for a wide range of geometrical parameters.

In Chapter 3, this previous analysis is extended to cover a significantly broader range of geometric parameters, focusing especially on the common doorway height, h, and relative length of one zone to the other. The key highlights follow.

- We study stratification due to exchange flow between zones of different temperature.
- Different exchange flow regimes are reported depending upon the architectural parameters.
- The merits and demerits of models of well-mixed and filling-box type are explored.
- Similitude laboratory experiments are again conducted for validating the model predictions.
- The application to attached solaria design is discussed.

The analysis of Chapter 4 represents a further extension of Chapter 3 in which case the doorway is replaced with a series of top and bottom vents. The key highlights follow.

- An analytical model is derived to analyze the ventilation process in the absence and in the presence of a source of buoyancy
- Different exchange flow regimes are observed depending on the source strength.
- The spatio-temporal evolution of the stratification and buoyancy is reported.
- Similitude laboratory experiments are again conducted for validating the model predictions.

In Chapter 5 the key conclusions arising from the present study are summarized and ideas for future research are outlined. Moreover, key analytical and experimental details are presented in the appendices. In particular, Appendix

A gives the relationship between the heat flux and the buoyancy flux. Appendix B briefly presents the derivation of the one-sided line plume filling-box equations, which are used extensively in Chapters 2-4. A discussion of the associated numerical algorithm is also given. Uncertainty analysis, the raw experimental data for Chapters 2 and 3 and the raw experimental data for Chapter 4 are presented respectively in Appendices C, D and E. Finally, Appendix F shows the technical drawings of the nozzle designed as a part of the experimental setup described in Chapter 4.

Chapters 2 and 3 of the thesis have already appeared in Building and Environment [81, 82], an international journal that publishes original research papers and review articles related to building science[1]. Meanwhile the material of Chapter 4 will soon likewise be submitted for publication. Further contributions and outcomes stemming from this thesis are given in Table 1-1.

Table 1-1. Scientific contribution arising from the present thesis.

Chapter	Journal/ Conference Proceeding	Status	Co-author
2	*Building Environ.*	Published (35 pages)	M. R. Flynn
	65th APS-DFD meeting	Presented	M. R. Flynn
3	*Building Environ.*	Published (37 pages)	M. R. Flynn
	Joint 11th *REHVA* and 8th International Conference on *IAQVEC*	Published (Extended abstract- 10 pages)	M. R. Flynn
4	-	To be submitted (40 pages)	M.R. Flynn

Moreover, I had the opportunity to present my work at the Annual General Meetings associated with the NSERC Smart Net-zero Energy Buildings Research Network (SNEBRN), held in May 2012 in Halifax, Nova Scotia and in May 2013 in Ottawa, Ontario. As an active member of SNEBRN I share the organization's vision "to perform the research that will facilitate widespread adoption in key

[1] http://www.journals.elsevier.com/building-and-environment/

regions of Canada, by 2030, of optimized NZEB [net-zero energy building] energy design and operation concepts suited to Canadian climatic conditions".

References

[1] http://www.statcan.gc.ca/pub/16-002-x/2008004/article/10749-eng.htm

[2] Santamouris M. Energy in the urban built environment: The role of natural ventilation. Earthscan, 2005.

[3] CMHC, 2004. Analysis of ventilation system performance in new Ontario houses. Technical Series 04-117, Canada Mortgage and Housing Corporation.

[4] Spengler JD, Sexton K. Indoor air pollution: A public health perspective. Science, 1983;221:9–17.

[5] Heiselberg P, Svidt K, Nielsen PV. Characteristics of airflow from open windows. Build Environ 2001;36(7): 859-869.

[6] Torcellini P, Pless S, Deru M, Crawley D. Zero Energy Buildings: A Critical Look at the Definition. ACEEE Summer Stud, Pacific Grove, California, USA (2006).

[7] Parker DS. Very low energy homes in the United States: Perspectives on performance from measured data. Energ Build, 2009;41:512–520.

[8] Chen Y, Athienitis AK, Galal K. Modeling, design and thermal performance of a BIPV/T system thermally coupled with a ventilated concrete slab in a low energy solar house: Part 1, BIPV/T system and house energy concept. Solar Energy 2011;84:1892-1907.

[9] Linden P. The fluid mechanics of natural ventilation. Annu Rev Fluid Mech, 1999;31:201–238.

[10] Liu PC, Lin HT, Chou JH. Evaluation of buoyancy-driven ventilation in atrium buildings using computational fluid dynamics and reduced-scale air model. J Fluid Mech, 2009;44:1970-1979.

[11] Linden PF, Lane-serff GF, Smeed DA. Emptying filling boxes: the fluid mechanics of natural ventilation. J Fluid Mech 1990;212:309-335.

[12] Fang L, Clausen G, Fanger PO, Impact of temperature and humidity on the perception of indoor air quality, Indoor Air 1998;8:80–90.

[13] Fang L, Clausen G, Fanger PO, Impact of temperature and humidity on chemical and sensory emissions from buildings materials, Indoor Air 1999;9:193–201.

[14] Melikov AK, Cermak R, Majer M, Maele K. Personalized ventilation: evaluation of different air terminal devices. Energ and Build 2002;34:829–836.

[15] Caulfield CP, Woods W. The mixing in a room by localized finite-mass-flux source of buoyancy. J Fluid Mech 2002;471:33-50.

[16] Merci B, Maele K. Numerical simulations of full-scale enclosure fires in a small compartment with natural roof ventilation. Fire Safety J 2008;43:495-511.

[17] Baines WD, Turner JS. Turbulent buoyant convection from a source in a confined region. J Fluid Mech 1969;37:51-80.

[18] Roony GG, Linden PF. Similarity considerations for non-Boussinesq plumes in un-stratified environment. J Fluid Mech, 1996;318:237–50.

[19] Morton BR, Taylor GI, Turner JS. Turbulent gravitational convection from maintained and instantaneous sources. J Fluid Mech 1956;234:1-23.

[20] Worster MG, Huppert HE. Time-dependent density profiles in a filling box. J Fluid Mech, 1983;132:457–466.

[21] Germeles AE. Forced plumes and mixing of liquids in tanks. J Fluid Mech 1975;71:601-623.

[22] Kuesters AS, Woods W. The formation and evolution of stratification during transient mixing ventilation. J Fluid Mech 2010;670:66-84.

[23] Lin YJP, Linden PF. Buoyancy-driven ventilation between two chambers. J Fluid Mech, 2002;463:293–312.

[24] Benjamin TB. Gravity currents and related phenomena. J Fluid Mech 1968;31:209-248.

[25] Klemp JB, Rotunno R, Skamarock WC. On the propagation of internal bores. J Fluid Mech 1997;331:81-106.

[26] Chen Q. Ventilation performance prediction for buildings: A method overview and recent applications. Build Environ 2009;44:848-858.

[27] Sandberg H, Lindstrom S. A model for ventilation by displacement. Proc. Roomvent'87, Stockholm, Sweden.

[28] Sandberg H, Lindstrom S. Stratified flow in ventilated rooms—a model study. Proc. Roomvent'90, Oslo, Norway.

[29] Linden PF, Cooper P. Multiple sources of buoyancy in a naturally ventilated enclosure. J Fluid Mech, 1996;311:177–92

[30] Caulfield CP. Stratification and buoyancy in geophysical flows. PhD thesis. Cambridge Univ., UK, 1991.

[31] Kaye NB, Hunt GR. Time-dependent flows in an emptying filling box. J Fluid Mech, 2004;520:135-156.

[32] Gorton RL, Sassi MM. Determination of temperature profiles in a thermally stratified air-conditioned system: Part 2. Program description and comparison of computed and measured results. Trans. ASHRAE, 1982;88(2), paper 2701.

[33] Jacobsen J. Thermal climate and air exchange rate in a glass covered atrium without mechanical ventilation related to simulations. 13th Natl. Solar Conf. MIT, Cambridge, MA, 1988,4:61–71.

[34] Cooper P, Mak N. Thermal stratification and ventilation in atria. Proc. ANZSES Conf., Adelaide, Australia, 1991:pp. 385–91.

[35] Shrinivas AB, Hunt GR. Transient ventilation dynamics induced by heat sources of unequal strength. J Fluid Mech, 2014;738:34-64.

[36] Brown WG, Solvason KR. Natural convection heat transfer through rectangular openings in partitions-I. Int J Heat Mass Transf 1962a;5:859–68.

[37] Brown WG, Solvason KR. Natural convection heat transfer through rectangular openings in partitions-II. Int J Heat Mass Transf 1962b;5:869–78.

[38] Shaw BH, Whyte W. Air movement through doorways—the influence of temperature and its control by forced airflow. J Inst Heat Vent Eng 1974;42:210–18.

[39] Linden PF, Simpson JE. Buoyancy driven flows through an open door. Air Infiltration Rev. 1985;6:4–5.

[40] Dalziel SB, Lane-serff G. The hydraulics of doorway exchange. Build Environ 1991;26:2:121-35.

[41] Chenvidyakarna T, Woods A. Multiple steady states in stack ventilation. Build Environ 2005;40:399–410.

[42] Fitzgerald SD, Woods A. On the transition from displacement to mixing ventilation with a localised heat source. Build Environ 2007;42:2210–2217.

[43] Coffey CJ, Hunt GR. Ventilation effectiveness measures based on heat removal: part 2. Application to natural ventilation flows. Build Environ 2007;42(6):2249–62.

[44] Hunt GR, Coffey CJ. Emptying boxes – classifying transient natural ventilation flows. J Fluid Mech 2010; 646:137–168.

[45] Holford JM, Woods AW. On the thermal buffering of naturally ventilated buildings through internal thermal mass. J Fluid Mech, 2007;580:3–29.

[46] Bassiouny R, Koura NSA. An analytical and numerical study of solar chimney use for room natural ventilation. Energ Buildings, 2008;40(5):865–73.

[47] Bolster DT, Linden PF. Particle transport in low-energy ventilation systems. Part 1: theory of steady states. Indoor Air 2009; 19: 122–129.

[48] Bolster DT, Linden PF. Particle transport in low-energy ventilation systems. Part 2: Transients and experiments. Indoor Air 2009; 19: 130–144.

[49] Shearer D, Porteous CDA. Winter performance of 2-storey solar buffer spaces in Glasgow demonstration houses. EuroSun 2012.

[50] Mottard JM, Fissore A. Thermal simulation of an attached sunspace and its experimental validation. Sol Energ 2007; 81: 305-315.

[51] Oliveti G, Arcuri N, De Simone M, Bruno R. Solar heat gains and operative temperature in attached sunspaces. Renew. Energy 2012, 39, 241–249.

[52] Stathopoulou OI, Assimakopoulos VD, Flocas HA, Helmis CG. An experimental study of air quality inside large athletic halls. Build Environ 2008;43:834–48.

[53] Baker N, Linden PF. Physical modelling of airflows—a newdesign tool. Atrium Build Archit Eng a991;13–22, Ed. F. Mills. CICC Publications, Welwyn, England

[54] Lane-Serff GF. Heat flow and air movement in buildings. PhD thesis, University of Cambridge, UK 1989.

[55] Kaye NB, Flynn MR, Cook MJ, Ji Y. The role of diffusion on the interface thickness in a ventilated filling box. J Fluid Mech 2010;652:195-205.

[56] Howell SA, Potts I. On the natural displacement flow through a full-scale enclosure and the importance of the radiative participation of the water vapour content of the ambient air. Build Environ 2002;37: 817–823.
[57] Zhang Z, Chen X, Mazumdar S, Zhang T, Chen Q. Experimental and numerical investigation of airflow and contaminant transport in an airliner cabin mockup. Build Environ 2009;44(1):85–94.
[58] Melikov AK, Popiolek Z, Silva MCG, Care I, Sefker T. Accuracy limitations for low-velocity measurements and draft assessment in rooms. HVAC&R Research 2007;13(6):971–86.
[59] Batchelor GK, Heat convection and buoyancy effects in fluids. Quart J Roy Met Soc, 1956;80:339-358.
[60] Rottman JW, Linden PF. Gravity Currents. In: Grimshaw R, editor. Environmental stratified flows. Dordrecht: Kluwer Academic Publishers; 2003, p. 89-118.
[61] Chenvidyakarn T, Woods A. Stratification and oscillations produced by precooling during transient natural ventilation. Build Environ 2007;42(1):99–112.
[62] Livermore SR, Woods AW. Natural ventilation of a building with heating at multiple levels. Build Environ 2007;42(3):1417–30.
[63] Morsing S, Strøm JS, Zhang G, Kai P. Scale model experiments to determine the effects of internal airflow and floor design on gaseous emissions from animal houses. Biosyst Eng 2008;99(1):99–104.
[64] Phillips JC, Woods AW. On ventilation of a heated room through a single doorway. Build Environ 2004;39:241-253.
[65] Mott RW, Woods AW. Quasi-steady states in natural displacement ventilation driven by periodic gusting of wind. J Fluid Mech 2012;707:1-23.
[66] Fitzgerald SD, Woods AW. Transient natural ventilation of a room with a distributed heat source. J Fluid Mech 2007;591:21–42.
[67] Norton T, Sun DW. Computational fluid dynamics (CFD) – an effective and efficient design and analysis tool for the food industry: a review. Trends Food Sci Tech 2006;17:600–20.

[68] http://www.ansys.com/Products/Simulation+Technology/Fluid+Dynamics/Fluid+ Dynamics+Products/ANSYS+Fluent

[69] http://www.ansys.com/Products/Simulation+Technology/Fluid+Dynamics/Fluid+ Dynamics+Products/ANSYS+CFX

[70] Abantoa J, Barreroa D, Reggioa M, Ozella B. Air flow modelling in a computer room. Build Environ 2004;39:1393–1402.

[71] Pope SB. Turbulent flows. Cambridge University Press; 2000.

[72] Launder BE, Spalding DB. The numerical computation of turbulent flows. Comput Method Appl Mech Eng1974;3:269–89.

[73] Yakhot V, Orszag SA. Renormalization group analysis of turbulence. J Sci Comp 1986;1(1):3–51.

[74] Maele K, Merci B. Application of RANS and LES field simulations to predict the critical ventilation velocity in longitudinally ventilated horizontal tunnels. Fire Safety J 2008;43(8):598-609.

[75] Hu CH, Ohba M, Yoshie R. CFD modelling of unsteady cross ventilation flows using LES. J Wind Eng Indust Aero 2008;96 (10-11):1692-1706.

[76] Zhai Z, Zhang Z, ZhangW, Chen Q. Evaluation of various turbulence models in predicting airflow and turbulence in enclosed environments by CFD: part 1 – summary of prevalent turbulence models. HVAC&R Research 2007;13(6):853–70.

[77] Chung W, Devaud CB. Buoyancy-corrected k–ε models and large eddy simulation applied to a large axisymmetric helium plume. Int J Numer Meth Fluids 2008; 58:57–89.

[78] Versteeg HK, Malalasekera W. An Introduction to Computational Fluid Dynamics: The Finite Volume Method. McGraw-Hill, 1st edition, 1995.

[79] Amsallem D, Cortial J, Farhat C. Toward Real-Time Computational-Fluid-Dynamics-Based Aeroelastic Computations Using a Database of Reduced-Order Information. AIAA JOURNAL 2010; 48(9):2029–2037.

[80] Malkawi AM, Srinivasan RS. A new paradigm for Human-Building Interaction: the use of CFD and Augmented Reality. Automat Constr 2005; 14:71–84.

[81] Nabi S, Flynn MR. The hydraulics of exchange flow between adjacent confined building zones. Build Environ 2013;59:76-90.

[82] Nabi S, Flynn MR. Influence of geometric parameters on the eventual buoyancy stratification that develops due to architectural exchange flow. Build Environ 2014;71:33-46.

Chapter 2

The hydraulics of exchange flow between adjacent confined building zones

2.1 Introduction

The exchange of a buoyant fluid of finite volume through one or more openings with an adjacent volume of ambient fluid is a common problem in fluid mechanics with numerous examples in natural, industrial, and architectural settings [1]. Important examples in the latter circumstance include the exchange of hot and cold air between the inside and outside of a building and between different zones within the same building. The temperature difference between such zones produces buoyancy forces that drive the flow. Knowledge of the

mixing process associated with such an exchange flow is important for the design of HVAC (heating, ventilation, and air conditioning) systems or for increasing the efficiency of natural ventilation [2-6].

Consider two zones with different temperatures in a one-storey building. The temperature difference can be a consequence of a difference of zone orientation relative to the sun or because in one zone high load (i.e. heat generating) electrical devices are used. If the temperature difference is small, the Boussinesq assumption implies that

$$\beta(T_0 - T_c) = -\frac{(\rho_0 - \rho_c)}{\rho_{00}} \tag{2-1}$$

where β is the coefficient of volumetric expansion (for ideal gases $\beta \sim 1/T$), T_0 and T_c are the temperatures in the dense and light zones respectively, with the densities ρ_0 and ρ_c similarly defined, and ρ_{00} is a reference density, e.g. the density of the dense zone. In the simple model suggested by Figure 2-1, the cold zone dimensions are $H \times \ell \times W$ with H as height, ℓ as length and W as width. The total length of both hot and cold zones is L.

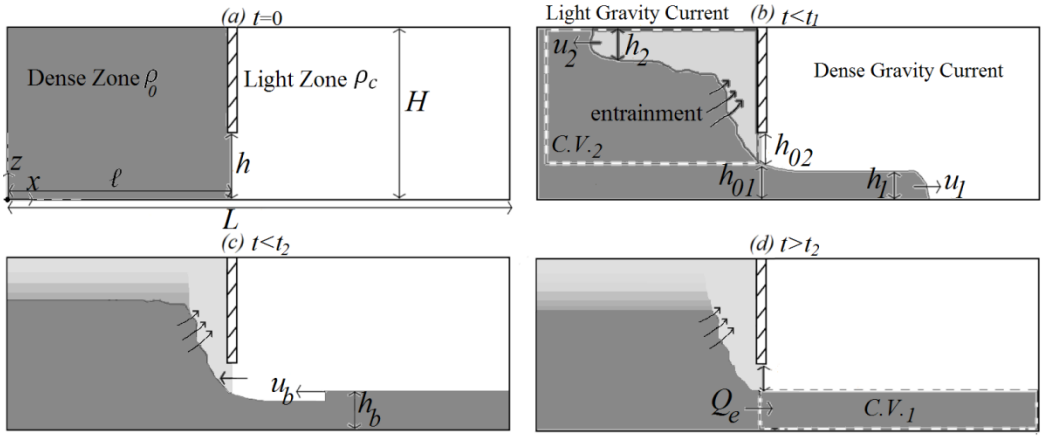

Figure 2-1. Schematic of the exchange flow at (a) $t = 0$, the instant when buoyancy-driven motion begins, (b) $t < t_1$, before the dense gravity current reaches the right end wall, (c) $t_1 < t < t_2$, after reflection of the dense gravity current as an internal bore, and, (d) $t \geq t_2$, after the bore has reached the horizontal position of the opening, $x = \ell$.

Loosely mimicking the sudden opening of a doorway between the building zones[2], let us suppose that the vertical barrier at $x = \ell$ is partially removed at time $t = 0$. As indicated schematically in Figure 2-1, for $t > 0$ the barrier spans a distance $H - h$ measured from the ceiling. For $h < H$, two qualitatively different kinds of flow are observed: a gravity current of dense fluid traveling at constant speed from left to right at the base of the hot zone and a buoyant plume rising through the cold zone. In the latter case, ambient (dense) fluid is entrained into the plume, which forms a (light) gravity current of its own when it reaches the ceiling. Over time and as the buoyant convection and entrainment continues there will develop a stable stratification of density in the ambient in a manner described by the "filling-box" theory of Baines and Turner [7]. Accordingly dense fluid of density ρ_0 is separated from fluid originating from the plume by a horizontal "first front" of elevation z_{ff} that descends over time. Meanwhile to the other side of the vertical barrier, and after some elapsed time, say, $t = t_1$, the (dense) gravity current will reflect from the right end wall whereupon a right-to-left traveling internal bore will be generated. The bore has a total height, h_b, travels at constant speed, u_b, and reaches the opening at $x = \ell$, at $t = t_2$, say. For $t \geq t_2$, the source conditions of the buoyant plume will be different from those for $t < t_2$ and slowly varying in time in a manner to be described below. Phillips and Woods [8] analyzed the exchange flow between an interior space and the external ambient through a single doorway. They carried out similitude experiments that characterized the room filling time as a function of doorway and room geometry. They also examined the impact of the source buoyancy on the interface height. In their analysis, however, Phillips and Woods [8] considered an exchange flow that remained critical (i.e. fully controlled) for all time. Moreover, Phillips and Woods [8] did not consider the details of the (evolving) interior stratification in the context of a filling box analysis. This latter simplification was relaxed in the follow-up investigation by Caulfield and Woods [9], who investigated the

[2] To reiterate, and for simplicity, we herein restrict attention to cases where the opening spans the width, W, of the building zones. Based on the analysis of Dalziel and Lane-Serff [16], we expect qualitatively similar flow behavior when $w/W < 1$ in which w is the opening width.

transient evolution of an interior space forced by a thermal source of fixed, but non-zero, volume flux. The interior and exterior spaces were able to exchange mass and buoyancy through a single low-level vent located at the same elevation as the source, i.e. at $z = 0$ in the coordinate system of Figure 2-1. This analysis was extended by Keusters and Woods [10] who added a second vent connecting interior to exterior. In both cases, and because of the finite source volume flux, the first front reached the source elevation $z = 0$ in finite time. Moreover, the exchange flows of interest occurred between the interior and (infinite) exterior spaces. Here, we take a different approach and examine the exchange flows that arise between two interior zones of finite size where the dynamics to one side of the vertical barrier influence the time evolution of buoyancy stratification to the other side. In the zone that initially contains dense fluid, flow dynamics are modeled by adopting the filling-box model of Baines and Turner [7] and Germeles [11]. In the zone that initially contains light fluid, concepts from gravity current and bore theory are employed [12-14]. The hydraulic exchange flow at $x = \ell$, connects the two halves of the problem and determines the source conditions for the plume and dense gravity current.

Therefore, our principal objective is to construct a composite model that combines various elemental (though nontrivial) pieces studied by others e.g. [7, 11-14]. Doing so gives us new insights into the flow physics associated with, say, a sudden change in the source conditions in the context of the filling-box flow shown schematically in Figure 2-1. As we shall demonstrate, the dynamics of the two zones illustrated in Figure 2-1 are highly coupled. Therefore, in the absence of a composite approach of the type described above, it is unlikely that the predictions of the associated (lower-order) model(s) would accurately describe the transfer of buoyancy from one zone to the other.

Throughout ℓ is considered to be similar in magnitude to $L - \ell$ so that the gravity current and bore speeds remain constant in time. Cases where $\ell \ll L - \ell$ or $\ell \gg L - \ell$ are of less architectural relevance and will be explored in a follow-up investigation. Moreover, we restrict our attention to instances where the first front illustrated in Figure 2-1c does not reach the top of the opening, which occurs

when h/H and ℓ/L are respectively large and small (see Figure 2-6b below). If the first front were to reach to the top of the opening at $z = h$, there would be a further abrupt change to the source buoyancy flux of the plume; we defer this scenario to a follow-up investigation.

In Section 2.2 aspects of the theory are discussed. Whenever necessary, we derive the equations applicable to our study. In Section 2.3 the experimental procedure is outlined. The experimental data is compared with theory in Section 2.4. The significance and application of this investigation is considered in Section 2.5, which also includes a summary of our most important results.

2.2 Theory

The flows described above are, for purposes of analytical efficacy, divided into three components: (i) a two-layer exchange flow at the opening, (ii) a buoyant plume that rises through the dense fluid and yields, through filling box dynamics to be explained below, a non-trivial ambient density stratification, and, (iii) the gravity current and resulting internal bore of dense fluid which ultimately affects the exchange flow and plume behavior.

The large value of Reynolds number allows us to assume that the flow is fully turbulent. The associated critical value of Re is discussed in the following section. Because of the relatively low speeds associated with architectural flows, we assume the flow to be incompressible. Even in exceptional circumstances where this approximation is questionable, Baines and Turner [7] argue that the quantitative details of the analysis can be preserved by replacing density with the potential density. Moreover, because we mimic flows in which the temperature difference is relatively small, the Boussinesq approximation can be applied by which (i) density variations are neglected except where they multiply gravitational acceleration, g, and (ii) temperature variations are assumed to be linearly proportional to density variations (equation 2-1). Consequently, the conservation of internal energy equation can be straightforwardly reduced to an equation for the conservation of buoyancy.

In the following subsections, we describe the governing equations for each flow in turn.

2.2.1 Exchange flow at doorway

The density difference between the two zones results in a two-layer exchange flow at $x = \ell$ in which dense fluid flows from left to right and occupies the lower portion of the opening to a depth of h_{01} (Figure 2-1). Light fluid flows with equal volume flux in the opposite direction and occupies the upper portion of the opening to a depth of $h_{02} = h - h_{01}$. By ignoring the effects of mixing between the two-layers, the exchange volume flux per unit width is given as

$$Q_e = u_{01}h_{01} = u_{02}h_{02} \tag{2-2}$$

with $u_{01}$and u_{02} as the vertically averaged fluid velocities in the lower and upper layers at $x = \ell$, respectively.

Many theoretical and experimental studies of exchange flow through a rectangular opening in a vertical wall have been carried out, e.g. [15-18]. Of these, the most relevant to our case is Dalziel [15] who showed that for a steady, Boussinesq, inviscid, and incompressible two-layer exchange flow through a doorway, the flow regime is critical such that the composite Froude number, defined as $Fr_c^2 = \frac{u_{01}^2}{g'h_{01}} + \frac{u_{02}^2}{g'h_{02}}$, is equal to unity with $g' = g\left(\frac{\rho_0 - \rho_c}{\rho_{00}}\right)$ the reduced gravity (ρ_0 and ρ_c are dense and light zone density, respectively). Using Dalziel and Lane-Serff's [16] approach, which is itself an extension of Dalziel's study, the flow is assumed to be fully-controlled for $t < t_2$, with t_2 is the time at which the internal bore reaches the doorway, and therefore a maximal exchange flow is realized. One can then show that the interface between the upper and lower layers is not located at the midpoint of the opening at $x = \ell$. Rather for a channel of constant width, h_{01} satisfies the asymptotic equation

$$\frac{h_{01}}{h} = \begin{cases} \frac{1}{2} + \frac{1}{4}\left(\frac{H}{h} - 1\right)^{1/3} - \frac{1}{8}\left(\frac{H}{h} - 1\right)^{2/3} & \frac{H}{h} < 2 \\ \frac{5}{8} & \frac{H}{h} \geq 2 \end{cases}, \qquad t < t_2 \tag{2-3}$$

Dalziel and Lane-Serf [16] argued that for small values of h/H ($\frac{H}{h} \geq 2$) the interface at the doorway does not vary significantly and always stand above the mid-point.

The associated exchange flow rate reads

$$Q_e = k(h)h\sqrt{g'h}, \quad t < t_2 \tag{2-4}$$

where $k(h)$ is defined as [15]

$$k(h) = \sqrt{\frac{\left(1-\frac{h_{01}}{h}\right)^3\left(\frac{h_{01}}{h}\right)^3}{\left(1-\frac{h_{01}}{h}\right)^3+\left(\frac{h_{01}}{h}\right)^3}} \tag{2-5}$$

Equation (2-4) is used to describe the maximal exchange flow for $t < t_2$; after the bore reaches the opening, the exchange flow rate becomes sub-maximal and monotonically decreasing in time. In this case, we instead apply a modified weir equation [17] of the form

$$Q_e = \left(\frac{1}{3}\right) C_d(h-h_{01})\sqrt{g'(h-h_{01})}\,, \qquad t \geq t_2 \tag{2-6}$$

where C_d is a discharge coefficient. In deriving (2-6), using Bernoulli's equation, the dissipationless velocity profile of $\sqrt{(2g'z)}$ is achieved with z as the distance above or below the midpoint. This gives a flux of $\sim 1/3 g'^{1/2}(h-h_{01})^{3/2}$ through the doorway. Holford and Hunt [18] show that buoyancy forces can result in a non-trivial reduction of the discharge coefficient from the canonical value of 0.6. For such cases, C_d is a function of the discharge parameter Γ_d defined as [19]

$$\Gamma_d = \frac{1}{2\sqrt{2}\alpha}\frac{(h-h_{01})^3 g'}{Q_e^2} \tag{2-7}$$

with α a plume entrainment coefficient to be discussed in more detail in Section 2.3. Holford and Hunt [18] chose the smaller Γ_d of the line and axisymmetric plume as a means of interpolating between the two limits. For vertical rectangular openings buoyancy effects are important for all $\Gamma_d > 0$, and C_d varies as [18]

$$C_d = 0.56 \times \Gamma_d^{-0.101} \tag{2-8}$$

When $t < t_2$ the interface height at $x = \ell$ is fixed at $z = h_{01}$, however, for $t \geq t_2$, the interface height must increase with time, t. Equation (2-6) is therefore solved by combining it with an evolution equation for h_{01} of the form

$$\frac{dh_{01}}{dt} = \frac{Q_e}{L-\ell}, \qquad t \geq t_2 \tag{2-9}$$

It should be emphasized that for all times, including $t = t_2$, the mass conservation is satisfied.

We integrate (2-9) using the fact that at t_2 the depth of the lower layer is equal to the depth, h_b, of the internal bore (Figure 2-1c). After some straightforward algebra, it can be shown that

$$\frac{h_{01}}{h} = 1 - \frac{4}{h\left(\frac{\left(\frac{1}{3}\right)C_d\sqrt{g'}}{L-\ell}(t-t_2) + \frac{2}{\sqrt{h-h_b}}\right)^2}, \qquad t \geq t_2 \tag{2-10}$$

Clearly $h_{01} \to h$ as $t \to \infty$. Combining (2-6) and (2-10) gives the exchange flow rate for $t \geq t_2$. In summary, and for arbitrary t, Q_e is given by

$$Q_e(t) = \begin{cases} k(h)h\sqrt{g'h}, & t < t_2 \\ \dfrac{8C_d\sqrt{g'}}{\left(\frac{\left(\frac{1}{3}\right)C_d\sqrt{g'}}{L-\ell}(t-t_2) + \frac{2}{\sqrt{h-h_b}}\right)^3}, & t \geq t_2 \end{cases} \tag{2-11}$$

In order to solve (2-11), we require estimates for the bore height, h_b, and t_2 where

$$t_2 = \frac{L-\ell}{u_1} + \frac{L-\ell}{u_b} = (L-\ell)\frac{u_1+u_b}{u_1 u_b} \tag{2-12}$$

in which u_1 and u_b are, respectively, the (time-independent) speed of the dense gravity current and internal bore. Hence, first we must derive the appropriate equations for the dense gravity current and internal bore, and afterwards we will be able to employ (2-11) as the transient boundary condition for the plume equations, which are discussed in Section 2.3.

2.2.2 Light zone: Gravity current and internal bore

By vertically withdrawing the barrier at $x = \ell$ by a distance h, a horizontal gravity current flows from left to right into the light zone i.e. the zone that initially contained light fluid of density ρ_c. At the leading edge of the gravity current a relatively sharp dividing curve is maintained between the current and the ambient. The gravity current, being after a brief time long and thin, has a hydrostatic pressure gradient in the vertical, or z, direction. Vertical accelerations are ignored away from the gravity current front. As discussed by Shin et al. [13], it is reasonable to ignore the effects of viscosity and assume an inviscid flow when $Re > 10^3$, where the Reynolds number is defined as $Re = \frac{\sqrt{g'h}h}{2\nu}$, with ν a reference kinematic viscosity. For nominally inviscid gravity currents, the pressure gradient in the horizontal direction is balanced by inertial forces. The gravity current head is followed by shear instabilities which cause the gravity current to mix with the (light) ambient. Nonetheless, consistent with many previous studies, we assume that this mixing is of limited dynamical importance at least insofar as influencing the bulk motion i.e. the front speed.

Benjamin [12] obtained the following equation for the front speed, u_1, in terms of the front height, h_1:

$$Fr_1^2 = \frac{{u_1}^2}{g'H} = \frac{h_1(H - h_1)(2H - h_1)}{H^2(H + h_1)} \tag{2-13}$$

Here Fr_1 is the Froude number of the dense gravity current. For the non-dissipative case, it can be shown that $h_1/H = 1/2$ and $Fr_1 = 1/2$. Benjamin [12] argued that currents occupying less than half the channel depth are dissipative and that external energy is required for gravity currents with $h_1/H \geq 1/2$.

Benjamin's equation (2-13) is one equation with two unknowns u_1 and h_1. To close the problem, we argue that the volume flux associated with the gravity current is given by

$$Q_e = u_1 h_1 \tag{2-14}$$

where we consider entrainment and detrainment effects due to shear flow instabilities to be of second order importance.

When the gravity current encounters the right end wall of Figure 2-1, an internal bore is reflected [20]. We need to relate the bore amplitude, h_b, to the bore velocity, u_b. The latter quantity is required when estimating t_2, the time at which the bore reaches the opening, and the former needed when evaluating Q_e from (2-11). As we demonstrate in Appendix 2-A, the relevant equation is

$$Fr_b^2 = \frac{{u_b}^2}{g'H} = \frac{h_1^2(H-h_1)(2H-h_b-h_1)}{H^2(Hh_1+Hh_b+{h_1}^2-3h_1h_b)} \tag{2-15}$$

which establishes the connection between the bore speed, u_b, and the bore height, h_b. If we assume the mass flux carried by the bore is equal to the gravity current front mass flux, we can write

$$Q_e = u_b(h_b - h_1) \tag{2-16}$$

Now by using (2-4), (2-15) and (2-16), the velocity and depth of the internal bore can be determined.

Once we solve for the dense gravity current and internal bore velocities and depths, t_2 can be found from (2-12). As the next step, the transient exchange flow rate can be estimated from (2-11). Before presenting theoretical results for Fr_1, Fr_b, t_2, and Q_e, we examine the flow dynamics to the left of the vertical barrier, i.e. those associated with the rising plume.

2.2.3 Dense zone: Plume and ambient interaction

A schematic of a plume ascending into a confined region, whose density profile is initially uniform and denser than the plume fluid, is given in Figure 2-1. When the plume fluid reaches the top of the channel, i.e. $z = H$, it spreads out horizontally and produces a layer with a density discontinuity separating it from the more dense ambient below. The ambient, previously homogenous, now consists of a deep layer of dense fluid and a thin layer of lighter fluid with density between ρ_0 and ρ_c. At the next time instant, the plume entrains fluid from both layers and therefore arrives at the top of the space slightly less dense than before.

Consequently, the first front is pushed downwards with a layer of lighter fluid appearing above. This process continues for still longer time leading to non-trivial density stratification in the ambient as described by Baines and Turner [7].

The plume of Figure 2-1 has a finite volume and momentum flux. Below, the governing equations for a one-sided line plume are provided assuming a Gaussian model for velocity and density, i.e.

$$w_p = \overline{w} e^{-\left(\frac{x}{b_p}\right)^2} \tag{2-17a}$$

$$g\frac{(\rho_a - \rho_p)}{\rho_{00}} = \Delta e^{-\left(\frac{x}{\lambda b_p}\right)^2} \tag{2-17b}$$

where w_p and ρ_p are the velocity and density of the plume, respectively. (2-17) assumes that the presence of the wall reduces the entrainment by a factor of 2 as compared to a free plume. However, consistent with Linden et al. [6], the left hand side of the profile of the velocity remains unchanged. Also $\overline{w}$ is the vertical velocity of the plume evaluated on the plume axis, b_p, the effective half-width of the plume is the radius at which $w_p = \overline{w}/e$ and λ is an empirical factor. We use λ =1.16 as suggested by Germeles [11]. Δ is the characteristic relative density within plume.

Following the classical work by Morton et al. [23] the time-averaged volume flux, Q, specific momentum flux, M, and specific buoyancy flux, F, within plume are defined as:

$$Q = \frac{\sqrt{\pi} b_p \overline{w}}{2} \tag{2-18a}$$

$$M = \frac{\sqrt{\pi} b_p \overline{w}^2}{2} \tag{2-18b}$$

$$F = \frac{\sqrt{\pi} b_p \overline{w} \Delta}{2} \tag{2-18c}$$

By using equations of mass, momentum and buoyancy conservation, these averaged fluxes must satisfy:

$$\frac{dQ}{dz} = \sqrt{2}\alpha\frac{M}{Q} \tag{2-19a}$$

$$\frac{dM}{dz} = \sqrt{\frac{1+\lambda^2}{2}}\frac{FQ}{M} \tag{2-19b}$$

$$\frac{dF}{dz} = Q\frac{\partial \Delta_a}{\partial z} \tag{2-19c}$$

with $\Delta_a = g\frac{(\rho_a - \rho_0)}{\rho_{00}}$. In (2-19) Taylor hypothesis for entrainment is applied, which states that the entrainment velocity at each elevation is proportional to the centerline velocity within the plume. The associated proportionality constant is called the entrainment coefficient. In determining the appropriate value of α to apply in solving (2-19a-c), we compared all available experimental data with the predictions of our model equations, generated using a range of reasonable values for the entrainment coefficient. A particular optimum value of α was selected by minimizing the aggregate total distance between theoretical and experimental curves in figures such as Figure 2-13 below. Therefore, we select the plume entrainment coefficient α =0.14. This result is broadly consistent with other measurements for line plumes (e.g. [24-25]). Whereas the choice of α has a mild impact on the particulars of the density stratification in the zone that initially contained dense fluid, its numerical value is immaterial insofar as the total buoyancy exchanged between the two zones, which is a function only of Q_e.

Following Baines and Turner [7], Δ_a evolves according to the advection equation

$$\frac{\partial \Delta_a}{\partial t} = \frac{Q}{\ell}\frac{\partial \Delta_a}{\partial z} \tag{2-19d}$$

in the region above the first front. Below the first front, the ambient density is equal to ρ_0 and Δ_a =0. Baines and Turner [7] proposed (2-19) in the limit $b_p \ll \ell$, so that the ambient fluid evolves on a much longer time scale than does the plume fluid. This is consistent with present study in particular our assumption that ℓ is not too much smaller than L.

The motion of the descending first front is directly proportional to the plume volume flux and inversely proportional to the breadth of the dense zone, i.e.

$$\frac{dz_{ff}}{dt} = \frac{Q}{\ell} \tag{2-20}$$

where z_{ff} corresponds to the elevation of the first front. The boundary conditions read

$$Q = Q_e \tag{2-21a}$$

$$M = \frac{{Q_e}^2}{h - h_{01}} \tag{2-21b}$$

$$F = g'Q_e \tag{2-21c}$$

The governing equations are thereby subjected to transient boundary conditions that asymptotically tend to zero. To our knowledge, this is the first time that such an approach has been considered. Note that the vanishing boundary conditions make it impossible to non-dimensionalize the governing equations in the manner of Germeles [11].

For simplicity the source is assumed to be at the top of the opening, i.e. we apply the boundary conditions (2-21) at $z = h$. We considered other elevations as the position of the plume source, but determined that these gave an inferior comparison between theory and experiment insofar as the front speed of the light gravity current and also the terminal stratification in the dense zone. In the present investigation, and as noted above, we restrict attention to cases where the first front does not reach the source so that at and below the source the ambient density is always described by $\Delta_a = 0$.

As noted by Killworth and Turner [26] and Bolster and Caulfield [27], for time-varying boundary conditions it is possible that the buoyancy flux, F, becomes negative at some particular elevation. We limit the integration of (2-19) to the domain below that particular elevation; above that elevation we assume that there is no plume i.e. the fluxes are undefined. Equivalently, we neglect the rate of penetrative entrainment.

When the rising plume first reaches the top of the dense zone, its density is less than ρ_0, the ambient density. Plume fluid therefore spreads as a gravity current travelling from right to left in Figure 2-1. The dynamical details of such a gravity current are ignored in Baines and Turner's [7] investigation. Instead Baines and Turner [7] assume (for $t = 0$ and $t > 0$) that the discharged plume fluid spreads to the side walls instantaneously. However, by solving the plume equations and thereby considering entrainment into the plume, one can study more carefully the gravity current that materializes along the top of the channel at early times. By mass balance

$$Q(z = H) = u_2 h_2 \tag{2-22}$$

where u_2 and h_2 are defined in Figure 2-1b.

We also have a relationship between the velocity and the depth of the light gravity current from Benjamin's equation (2-13). Here, of course, the density difference is not $\rho_0 - \rho_c$, as in the case of dense gravity current, but is equal to $\rho_0 - \rho_a|_{z=H,t=0}$. Hence, instead of $g' = g\frac{\rho_0 - \rho_c}{\rho_0}$, we now write $-\Delta_a|_{z=H,t=0} = g\frac{\rho_0 - \rho_a|_{z=H,t=0}}{\rho_0}$. Therefore, the Benjamin [12] equation for the light gravity current is written as

$$\frac{u_2^2}{-\Delta_a|_{z=H,t=0} h_2} = \frac{(2H - h_2)(H - h_2)}{H(H + h_2)} \tag{2-23}$$

Solving (2-22) and (2-23) together yields estimates for u_2 and h_2. Here we assumed the fluid at the top has uniform density.

2.2.4 Theoretical predictions

In this subsection, we combine the previous equations and present model predictions for both building zones of Figure 2-1.

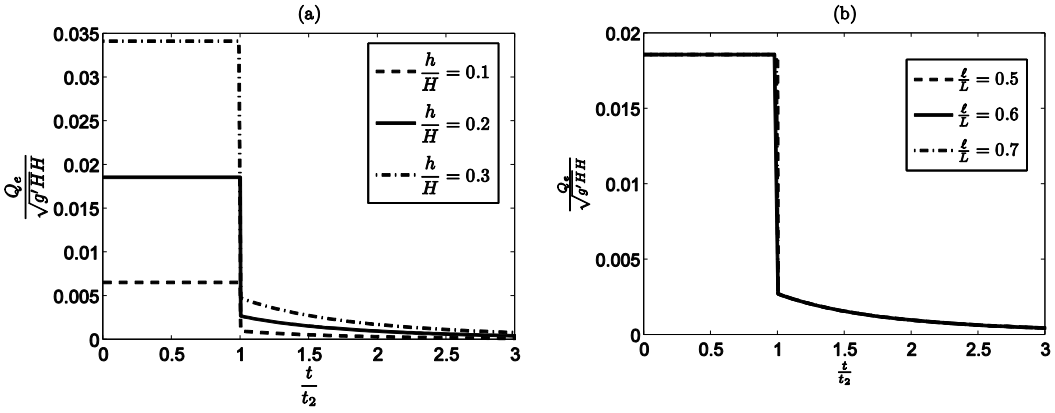

Figure 2-2. Dimensionless exchange flow rate with respect to dimensionless time (a) $\frac{\ell}{L}$ =0.5 and various $\frac{h}{H}$ (b) $\frac{h}{H}$ =0.2 and various ℓ/L.

The dimensionless exchange flow rate with respect to dimensionless time is given in Figure 2-2. By increasing h/H, the rate of exchange flow increases. It can be seen from panel b that changing ℓ/L has essentially no impact on the exchange flow rate. This is expected: (2-11a) makes no reference to ℓ/L and, from (2-11b), Q_e is only a weak function of ℓ/L for $t \geq t_2$. On the other hand, Q_e is strongly dependent on h/H whether $t < t_2$ or $t \geq t_2$ (Figure 2-2a).

Figure 2-3a shows Fr_1, $Fr_2 = u_2/\sqrt{g'H}$ and Fr_b with respect to h/H. Fr_1 increases with h/H, reaching a maximum of 0.53 when h/H =0.87. Similar to the dense gravity current, Fr_2 also exhibits a maximum for $h/H < 1$, i.e. of 0.51 when h/H =0.95. The observed global maxima for both Fr_1 and Fr_2 is a result that mimics the solutions determined by Benjamin [12] who plotted the non-dimensional front speed as a function of h_1/H. To be clear, important differences exist between our analysis and his e.g. he did not make reference to boundary conditions and therefore omits reference to "doorways" and suchlike. Nonetheless, as the derivation of Section 2.2 makes clear, we can, and do, still make use of Benjamin's front condition and thereby inherit certain features of his solution including the global maximum of Fr. The maxima for Fr_1 and Fr_2 occur for different h/H reflecting the influence of the ambient fluid entrained into the rising plume which renders $-\Delta_a|_{z=H,t=0}$ less or much less than g'.

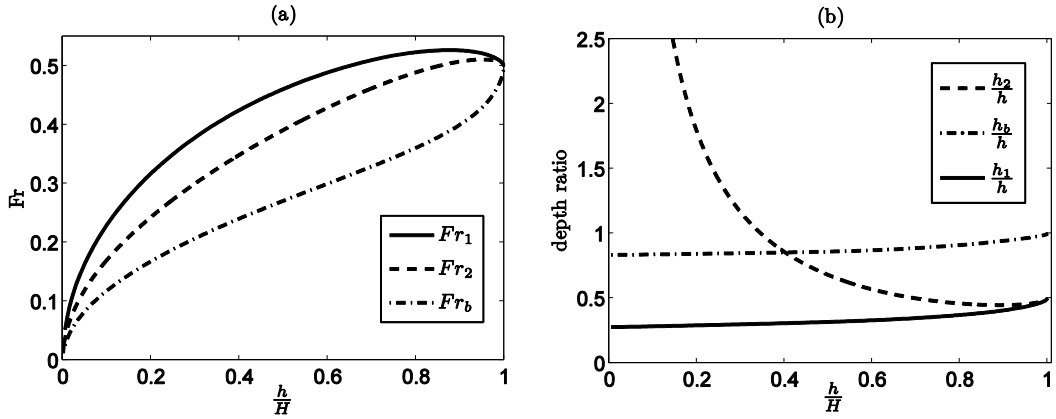

Figure 2-3. (a) Froude number and (b) dimensionless depth for the dense gravity current ($Fr_1$and $\frac{h_1}{h}$), light gravity current (Fr_2 and $\frac{h_2}{h}$) , and reflected bore (Fr_b and $\frac{h_b}{h}$).

As shown in Figure 2-3a, in limit of h/H =1, (2-15) yields Fr_b =1/2, the familiar gravity current result, which is consistent with Figure 2b of Klemp et al. [14]. Moreover, Fr_b (and h_b/h) both monotonically increase with h/H. A similar trend is observed in Figure 3 of Klemp et al. [14], although they plot $u_b/\sqrt{g'h_1}$ versus h_b/h_1. As in Benjamin's study, Klemp et al. [14] do not examine the influence of a doorway i.e. their solution does not make reference to lateral boundary conditions.

Shown in Figure 2-3b are the dimensionless depths with respect to h/H. h_1/h, which increases by about a factor 2 from $h/H = 0$ to h/H =1, has a mean value of 0.33 suggesting that the dense gravity current height is set by h rather than the height, H, of the building zone. However, the depth of the light gravity current decreases for h/H <0.89 with a minimum value of 0.45; this depth is set by H rather than h. It should be recalled that the velocity and depth of light gravity current are coupled to the dynamics of the ascending plume and cannot be trivially determined from the initial conditions.

Figure 2-4 shows the variation of dimensionless t_2 with h/H. By increasing h/H, the velocities of the dense gravity current and reflected bore increase and therefore t_2 decreases. In addition, by increasing ℓ/L the distance travelled by the gravity current and internal bore decreases, which likewise decreases t_2.

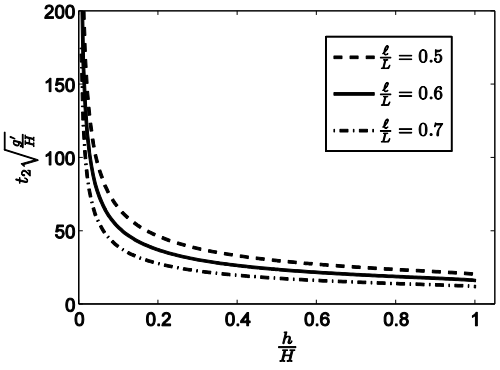

Figure 2-4. $t_2\sqrt{\frac{g'}{H}}$ as a function of $\frac{h}{H}$ for different $\frac{\ell}{L}$.

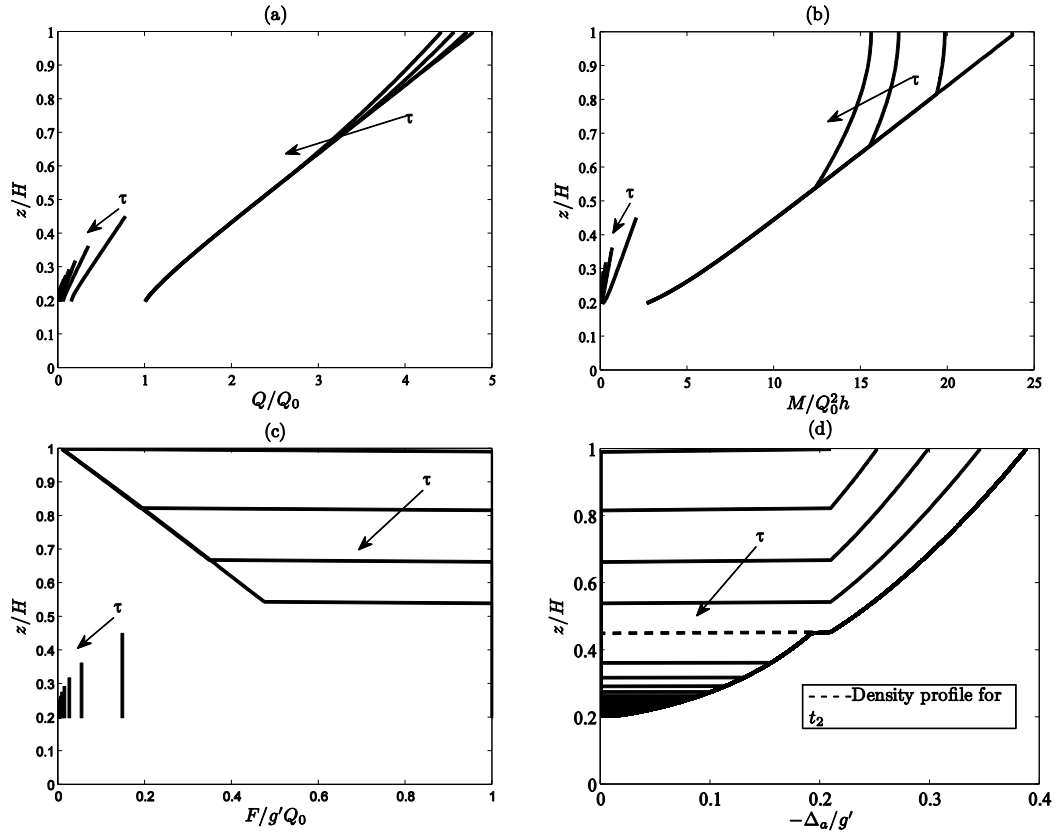

Figure 2-5. Dimensionless fluxes of volume, momentum, and buoyancy and the stratification profiles at different dimensionless times $\tau = \frac{t}{t_2}$ for $\Delta\tau$ =0.25 when $t < t_2$ and $\Delta\tau$ =1 when $t \geq t_2$. Here $\frac{h}{H}$ =0.2, and $\frac{\ell}{L}$ =0.5.

In Figure 2-5a and 5b, the non-dimensional plume volume flux, $Q(z,t)/Q_0$, and momentum flux, $M(z,t)/(Q_0^2.h)$, are shown versus z/H for various non-

dimensional times. Q_o is defined as the initial exchange flow rate i.e. for $t < t_2$ from (2-4). Here h/H =0.2 and so the fluxes are defined over a range of 0.2≤ z/H ≤1.0. Figure 2-5a and 5b have similar features to Figures 2-12 and 2-11, respectively, of Germeles [11]. Due to the entrainment of ambient fluid, Q is an increasing function of height. The momentum flux, M, likewise increases with z due to the impact of buoyancy forces. However, in contrast to Germeles's results, we consider transient source conditions and thus observe a dramatic decrease in Q and M when $t = t_2$.

In Figures 2-5c and 2-5d, respectively, we present the non-dimensional buoyancy flux, $F(z,t)/(g'Q_0)$, and the ambient density, $-\frac{\Delta_a(z,t)}{g'} = \frac{\rho_0-\rho_a}{\rho_0-\rho_c}$. After t_2, whose density profile is highlighted by the dashed curve in Figure 2-5d, the velocity and density jump across the first front decrease substantially. This is in contrast to Figure 13 of Germeles [11] or Figure 7 of Kuesters and Woods [10] in which the density jump across the first front is constant at all times. In fact, for $t > t_2$ we find that F becomes negative at the first front i.e. we predict that the plume does not reach the top of the control volume. Of course below the first front, F remains equal to its source value (which is notably less than the source buoyancy flux for $t < t_2$). If the velocity of the first front becomes vanishingly small before reaching the source, the front halts at distance R (defined in Figure 2-6a) above the source, i.e.

$$R = \left(\frac{z_{ff}}{H} - \frac{h}{H}\right); t \to \infty \tag{2-24}$$

R is shown as a function of ℓ/L and h/H in the phase plane diagram of Figure 2-6b. We can rationalize these results with reference to equation (2-20): for smaller ℓ/L and larger h/H, the descending velocity of the first front is relatively large and the front is therefore able to reach the source in finite time.

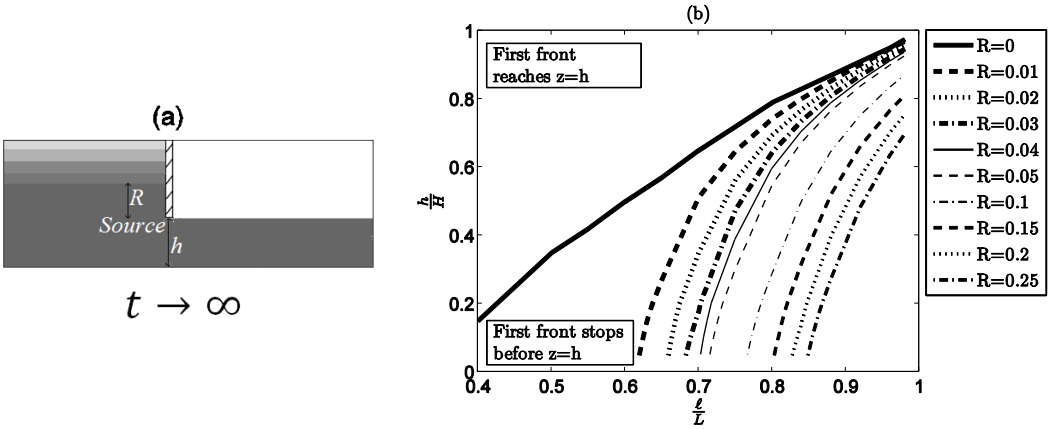

Figure 2-6. (a) Schematic showing R, the asymptotic position of the vanishing front. (b) Phase plane of parameters showing for what range of h/H and ℓ/L the first front reaches the source.

Regarding the dense zone stratification, we are especially interested in the effects of the height of the opening, h, and the lock length, ℓ. Figure 2-7a shows the terminal dimensionless density profiles, $-\Delta_a(z,t)/g'$ for various of h/H. It can be seen that by increasing h, $-\frac{\Delta_a}{g'}|_{z=H}$ increases: for larger h/H, the plume is comparatively short and therefore there is less entrainment which leads to a larger density contrast between the fluids above and below the first front. Figure 2-7b shows the analogous dimensionless density profiles for various ℓ/L. By decreasing ℓ/L, the first front, whose velocity is given by Q/ℓ, descends more rapidly.

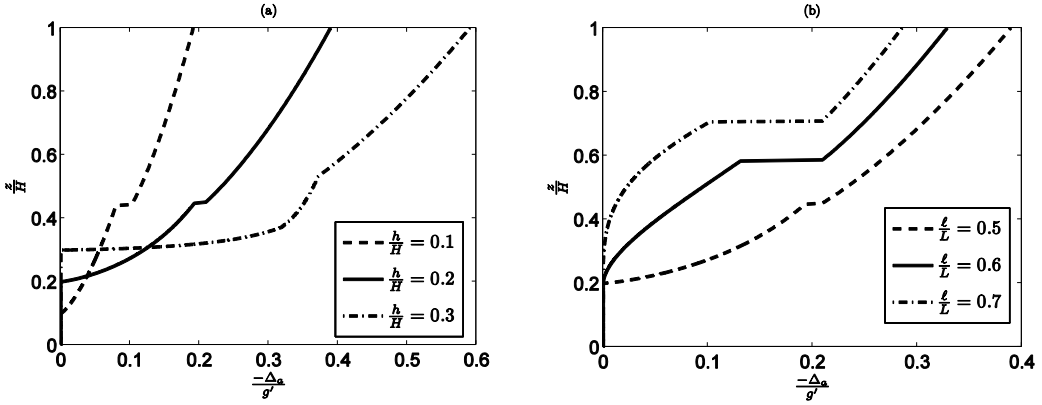

Figure 2-7. Comparison of ambient stratification; (a) $\frac{\ell}{L}$= 0.5 and various $\frac{h}{H}$, (b) $\frac{h}{H}$ = 0.2 and various ℓ/L.

The non-dimensional buoyancy b of the dense zone of Figure 2-1 is defined as

$$b(t) = -\frac{1}{g'HL}\int_0^{\ell}\int_0^{H}\Delta_a(z,t)\,dzdx \tag{2-25}$$

In Figure 2-8, the total buoyancy is shown as a function of t/t_2 for various geometries. This figure is comparable to Figure 2 of Caulfield and Woods [9] or Figure 4b of Kuesters and Woods [10] where buoyancy is depicted as a function of dimensionless time. In the former study, for example, the buoyancy increases linearly before the first front reaches the source. The same trend can be perceived in Figure 2-8, at least up until $t = t_2$ whereupon Q_e and the associated source buoyancy flux drop abruptly. Thus in contrast to both Caulfield and Woods [9] and Kuesters and Woods [10], the mean density of the zone that initially contained the dense fluid does not asymptotically tend to that of the source, reflecting the finite size of each zone.

The buoyancy is an increasing function of h/H: by increasing h/H the depth of the gravity current and the mass carried by its head increases and therefore more dense fluid flows from left to right in Figure 2-1. By mass continuity, this dense fluid is of course replaced by light fluid from the zone to the right of the internal partition. Moreover, the buoyancy is a decreasing function of ℓ/L.

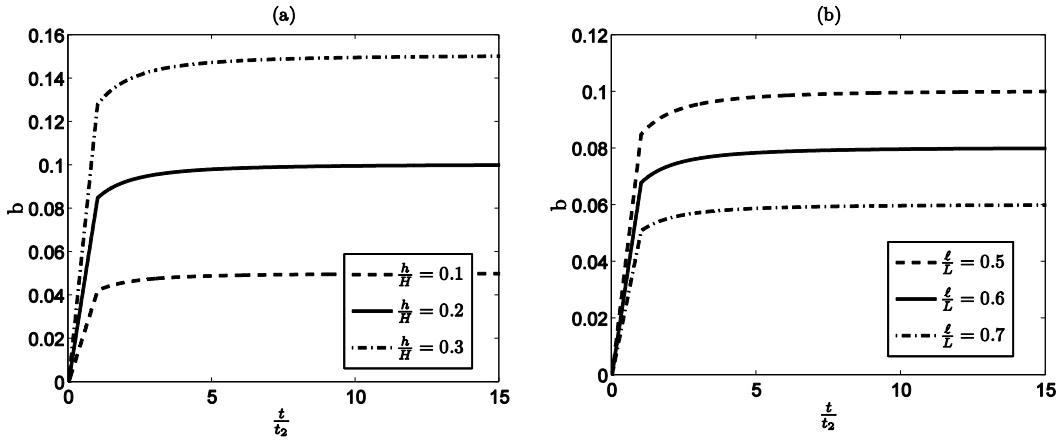

Figure 2-8. Total buoyancy variation with time for (a) $\frac{\ell}{L}$ = 0.5 and various $\frac{h}{H}$, (b) $\frac{h}{H}$ = 0.2 and various ℓ/L.

2.3 Experimental apparatus and procedure

To verify the analytical results, a series of similitude laboratory experiments was performed. Experimental measurements were carried out for the purpose of (i) measuring the speed of the dense and light gravity currents and the reflected bore, and, (ii) measuring the ambient stratification profiles resulting from the ascending plume and its subsequent lateral spreading at $z = H$. Following a long line of earlier studies (as summarized in e.g. Linden [28]), we used water as the working fluid in our similitude experiments, which makes it possible to achieve much larger Reynolds numbers than would be possible using air.

If the Reynolds numbers of the model and the room match then the results, in terms of turbulent phenomena, are expected to be the same at both scales. In practice, Reynolds number matching can be quite challenging between the model and the real building zone, particularly for smaller scale ratios. The characteristic velocity scales as $\sqrt{g'H}$ and, therefore, the Reynolds number of the model is

$$Re_{model} = \frac{\sqrt{\left(g\frac{\Delta\rho}{\rho}\right)H_{model}^3}}{2\nu_{water}} \tag{2-26-a}$$

and for the room it can be defined as

$$Re_{room} = \frac{\sqrt{\left(g\frac{\Delta T}{T}\right)H_{room}^3}}{2\nu_{air}} \tag{2-26-b}$$

For our experimental model the density differences are such that $\frac{\Delta\rho}{\rho} = 0.04$ and therefore $10^4 < Re_{model} < 3\times10^4$. Conversely, a typical maximum temperature difference between adjacent building zones is approximately 5 K [3]. Therefore, for our 10-15:1 scale model (the exact ratio depends on the height of the room) the Reynolds number of the model is between 30-60% that of the room. However, Thatcher et al. [29] showed that if Re is large enough so that turbulent structures appear in the similitude experiments then the laboratory results can generally be scaled-up with confidence. In our experiments, such large scale structures (i.e. turbulent eddies) were plainly visible. Thatcher et al. [29] provide

more quantitative guidance when they make the following assertion: if $\mathrm{Re}_{\mathrm{room}}$ is about 20% of $\mathrm{Re}_{\mathrm{room}}$, but still large enough to have an inertial subrange of eddy sizes, the relative difference expected vis-a-vis turbulent kinetic energy and turbulent mass diffusivity is only 5%. Based on Thatcher et al.'s calculations, we estimate that our similitude experiments admit flows that are quantitatively similar to those that would be observed in a real building.

Experiments were run in a plexiglas tank of length $L = 227.5$ cm, width $W = 25.0$ cm, and height of 35.0cm with an acrylic barrier mounted on vertical sliders at $x = \ell$ for subdividing the tank into two zones. The position of this barrier and the height of opening were adjustable. Experiments are carried out for various ℓ/L and h/H i.e. $0.125 \leq h/H \leq 1$ and $0.25 \leq \ell/L \leq 0.75$.

The tank was filled with tap water of density $\rho_c = 0.9984$ g/cm^3 up to a depth of $H = 20.0 \pm 0.1$ cm. Then we added salt and a small quantity of dye (food coloring) to the lock region. The typical density of saline water was $\rho_c = 1.04$ g/cm^3. In select experiments, dye was added to the opposite side of the tank. In order to measure fluid densities, an Antor Paar densitometer DMA 4500 with an accuracy of ± 0.0001 g/cm^3 was used. Experiments began by vertically extracting the gate to a height h. Given the need to avoid very large accelerations or decelerations, the speed of removal depends on h/H. Thus when h/H is large, the speed of removal was also relatively large. More quantitatively, in the limit as h/H approaches 1, the removal speed was approximately 15 cm/s whereas when h/H was only 0.125, speeds as low as approximately 3 cm/s were measured. The average removal speed of approximately 8 cm/s obviously falls between these two extremes. Among other considerations, standardizing the removal speed could only be achieved at the expense of having a less tight seal between the two zones prior to removing the gate and so was not deemed to be worthwhile.

For purposes of flow visualization, either one or two externally-triggered 1280×1064, 12 bit cameras (LaVision GmbH, Imager 3) were employed with frame rates of between 8Hz and 17 Hz. The captured images were post-processed using MATLAB. Images were cropped then thresholded, the latter step being applied so that the intensity contrast between the gravity current head and ambient

fluid was sharp. By measuring the location of a sudden change of pixel intensity, it was therefore straightforward to estimate the front position and, by extension, the front speed. Similar comments applied when determining the speed, u_b, of the bore.

After a large time, say $20t_2$, no flow was evident i.e. the system was quiescent. At this moment, we used a conductivity probe (Precision and Measurement Engineering, MSCTI) which was mounted on a vertical traverse (Velmex, X-Slide) to measure the terminal ambient stratification in the dense zone. For calibration of the probe, we gathered five samples from the ambient medium and used these to find the linear relationship between the voltage measured by the probe and the fluid density.

2.4 Results and discussion

Representative experimental snapshots of the light zone are provided in Figure 2-9, which shows time series images of a gravity current (LHS) and bore (RHS). Figure 2-9 also shows the corresponding front position of the dense gravity current and the internal bore as functions of time.

Representative experimental snapshots of the dense zone are provided in Figure 2-10 where, in contrast to the experimental image of Figure 2-9, dye has now been added to the fluid of density ρ_c. At t/t_2=0.25 the front of the light gravity current is clearly distinguishable. It is apparent that the first front travels towards the source with increasing time. At larger times (i.e. t/t_2=5.2) it can be seen from the gradient of color intensity in the upper layer that the ambient is non-trivially stratified above the source. Note that a bore is evident in panels c and d of Figure 2-10. However, we do not examine the dynamics of such bore in the analytical model. Rather, we follow filling-box approach of Baines and Turner [7] by which such horizontal flows are ignored.

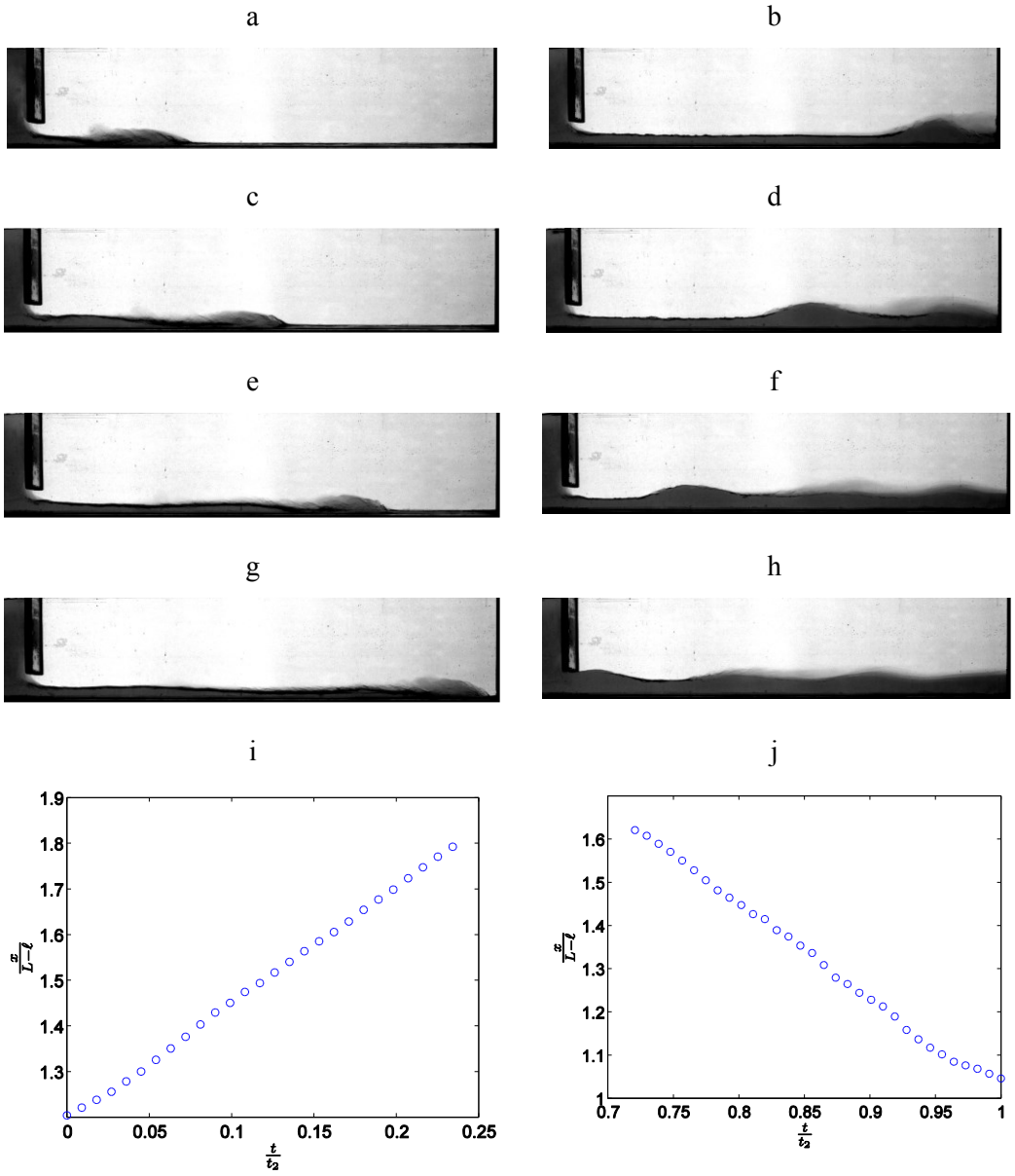

Figure 2-9. Time evolution and front position of the dense gravity current (LHS) and associated reflected bore (RHS) with $\frac{h}{H}$ =0.25, Re= 4520, $\frac{\ell}{L}$= 0.50, and $\frac{t}{t_2}$ = 0.1, 0.17, 0.23, and 0.33 for LHS and $\frac{t}{t_2}$ = 0.67, 0.79, 0.91, and 1.00 for RHS. The field of view measures 20 cm tall by 68 cm long.

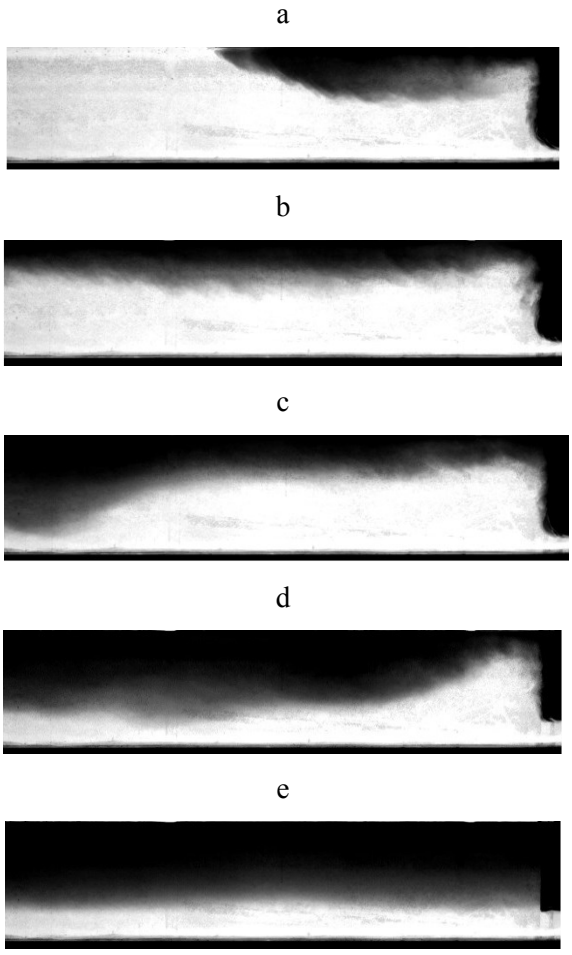

Figure 2-10. Time evolution of a stratification with $\frac{h}{H}$ =0.25, Re= 1600, $\frac{\ell}{L}$= 0.50 and $\frac{t}{t_2}$ = 0.25, 0.50, 0.75, 1.00, and 5.20. The field of view measures 20 cm tall by 68 cm long.

Model results showing $Fr_1 = u_1/\sqrt{g'H}$ vs. h/H are given in Figure 2-11a where we now also include experimental data for various ℓ/L. Error bars are based on the results of repeated experiments conducted for selected h/H. More specifically, measurement uncertainties are based on the standard deviation of an ensemble of measurements with a confidence limit of 68% [30]. Benjamin's front condition neglects internal flows i.e. the current is treated as if it were a cavity with no raised head. However, Lowe et al. [31] showed by laboratory experiments that there is a larger flux of gravity current fluid at the back of the gravity current as compared to near the front with the difference being due to detrainment. Note also that Benjamin's front condition has been found moderately to over-predict

experimental measurements in related laboratory investigations e.g. that of Huppert and Simpson [32]. Although we have neglected such effects, the agreement is reasonable.

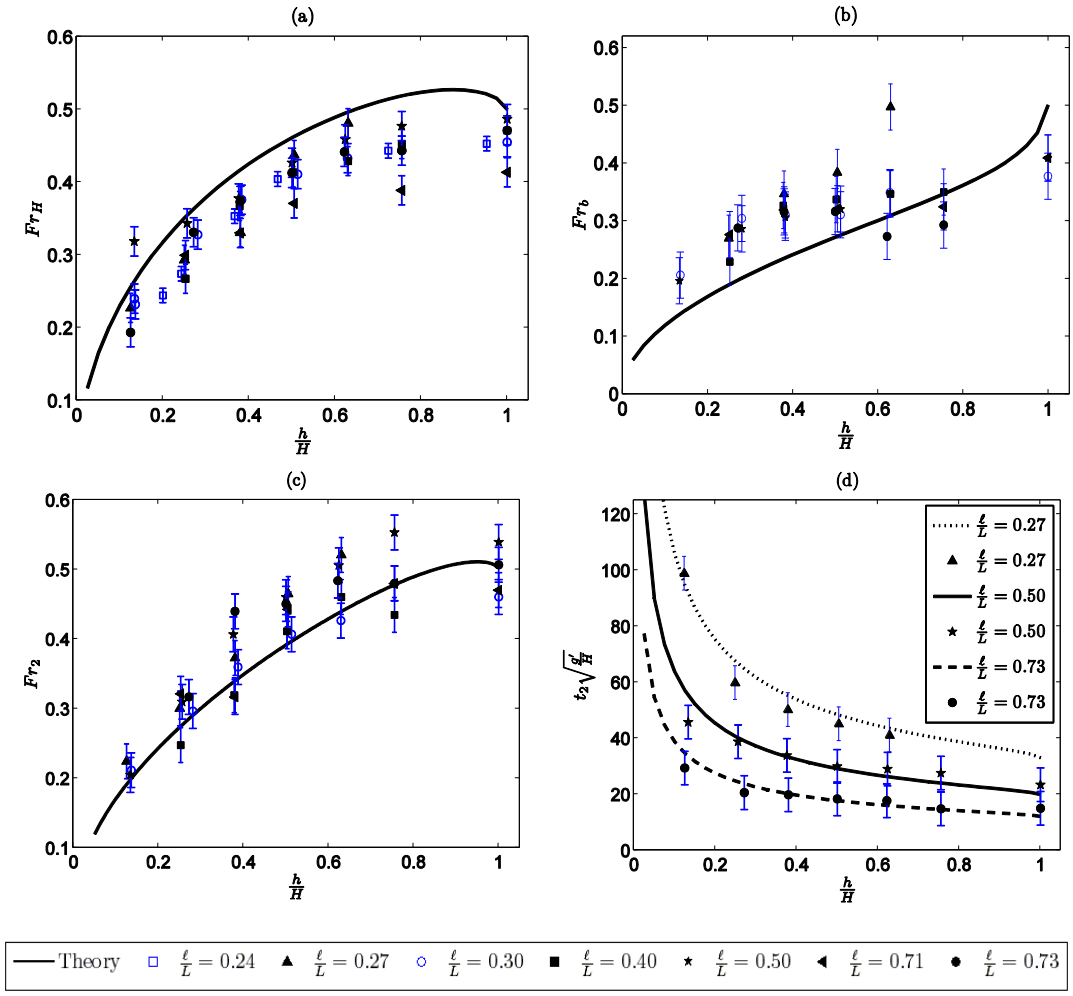

Figure 2-11. Comparison between theory and experiment: (a) dense gravity current, (b) internal bore, (c) light gravity current, (the theory curves for Figure 2-11a, b, c are the same as the curves of Figure 2-3a), (d) t_2.

Figure 2-11b shows $Fr_b = u_b/\sqrt{g'H}$ as a function of h/H where again experimental data are included. Compared to Figure 2-11a, the error bars for the experimental data points are larger reflecting greater difficulty of measuring the front position of the internal bore. Because the bore dynamics are highly dependent on those of the gravity current, any errors associated with the assumptions applied in calculating Fr_1 are manifest also in Fr_b. Moreover, we

applied Bernoulli's equation in the lower layer in deriving estimates for Fr_b. Consistent with the discussion of Rottman and Linden [33], this approximation becomes less accurate for larger h_1/H because it is then"indeterminate in which layer the required dissipation occurs".

Figure 2-11c shows the variation of $Fr_2 = u_2/\sqrt{g'H}$ with h/H. Here the agreement is moderately better for smaller h/H for which the flow of light fluid through the dense zone most closely resembles the vertically ascending plume envisioned by Baines and Turner [7] whose theory is reflected in (2-25) and, by extension, (2-22). On the other hand, although the validity of the Baines and Turner's equations becomes suspect for larger h/H, we continue to see good agreement with measured data in this regime. The theoretical model, comparing to the overprediction of Figure 2-11a, underpredicts the experimental data. This has important implications in Figure 2-11d, which shows t_2 as a function of h/H. Due to the over- and under- prediction, there is a fortuitous cancellation of errors that renders quite positive agreement in Figure 2-11d. In particular, all of the associated data sets predict a monotone decreasing variation of t_2 with h/H: by increasing the opening height, the dense gravity current and bore velocities likewise increase.

Summarizing the results of Figure 2-11, the average relative error is 15.6%, 20.2%, 7.8%, and 9.5% for Fr_1, Fr_b, Fr_2, and t_2 respectively.

Figures 2-12 and 2-13 show for two different ℓ/L and various h/H, the terminal stratification that develops as a result of the filling box dynamics described in Section 2.2.3. Because the buoyancy flux at the source is decreasing for $t > t_2$, the density jump across the first front vanishes as the source is approached. Such a phenomenon is seen in the experimental data too, whereas it is not observed when the plume is supplied from a time invariant source. A point-by-point comparison reveals better agreement for smaller h/H and larger ℓ/L. In practice the motion of the plume follows an inclined trajectory whereas our model assumes that the plume motion is purely vertical, which becomes less reasonable as h/H increases. For the extreme case of h/H =1, there is no plume, only a light gravity current. In addition, there is better agreement for larger ℓ/L. The reason is

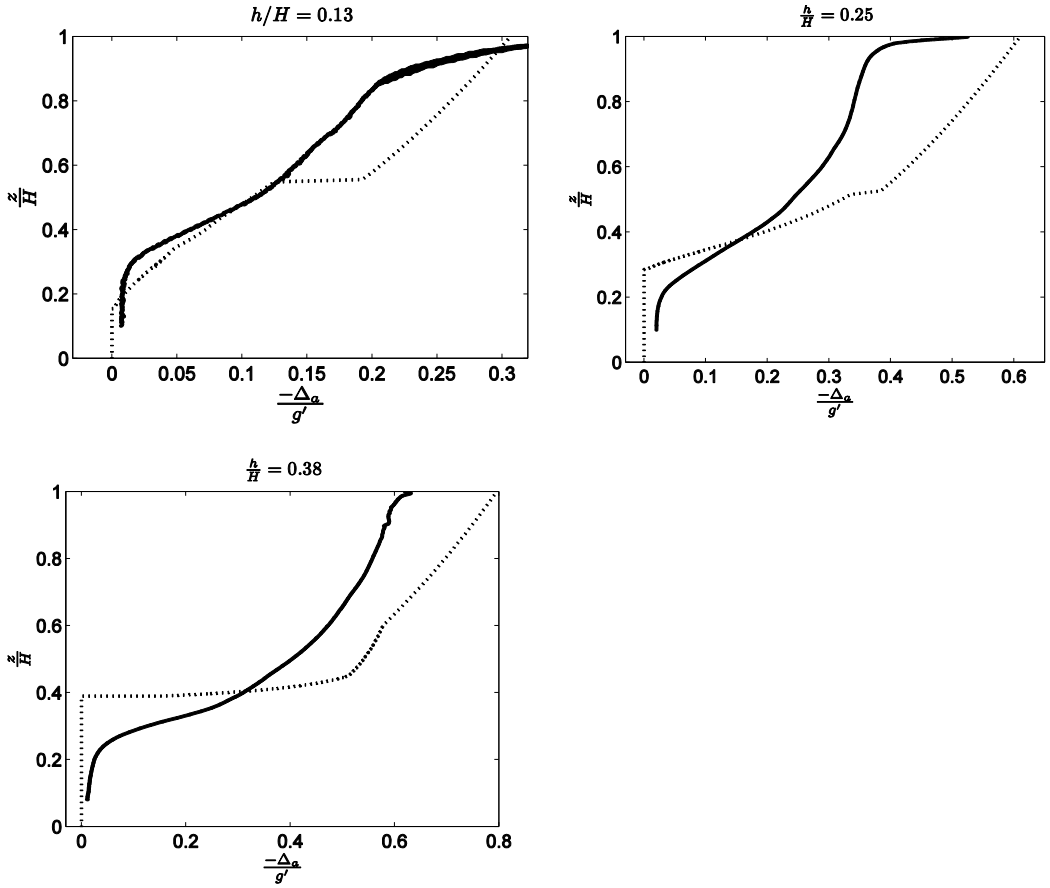

Figure 2-12. Comparison between theory (dotted line) and experiment (solid line) for $\frac{\ell}{L}$ =0.50. The terminal stratification of the dense zone is considered.

that for larger lock lengths the assumption of $\ell \gg b$, which is the basis of Baines and Turner's theory, is better justified. Also, for larger lock lengths, the first front descends more slowly suggesting a reduced sensitivity to transient flow features such as the irregular first front exhibited in Figure 2-10 (t/t_2=0.75), which is due to inertial effects.

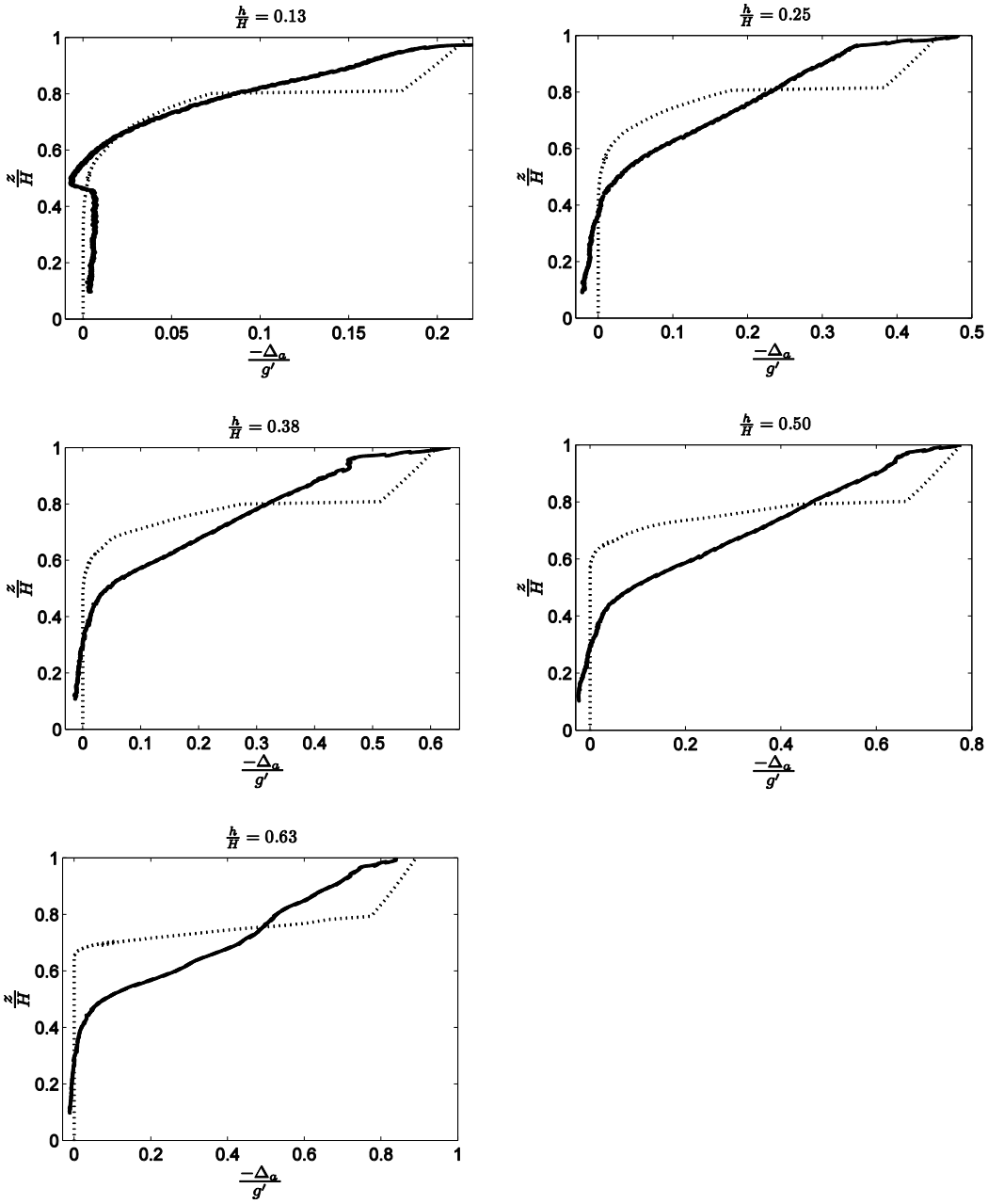

Figure 2-13. As in Figure 2-12 but with $\frac{\ell}{L}$ =0.73.

By integrating the area to the left of the curves in Figures 12 and 13, for both theoretical and experimental data, the terminal buoyancy, $b_\infty = \lim_{t\to\infty} b(t)$, can be calculated from (2-25). Results are presented in Figure 2-14. The promising result is that, despite the fact that point-by-point agreement is less

robust for higher h/H and smaller ℓ/L, the predicted b_∞ shows good agreement with measurements over a broad region of parameter space.

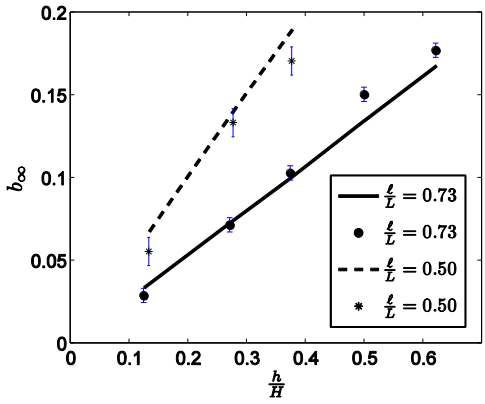

Figure 2-14. Experimental (points) and theoretical (lines) terminal buoyancy for $\frac{\ell}{L}$ =0.50 and $\frac{\ell}{L}$ =0.73 for various h/H. We only present the data for $R > 0$ where R is defined by (2-24). For $\frac{\ell}{L}$ =0.5 at $\frac{h}{H}$ =0.38 and for $\frac{\ell}{L}$ =0.73 at $\frac{h}{H}$ =0.63, the first front reaches to the source and the model is not applied.

2.5 Conclusions

In this Chapter the hydraulics of Boussinesq two-layer exchange flow between two finite regions is considered both theoretically and experimentally. A major application is in the architectural context. By opening the doorway separating a building zone containing cold air from an adjacent zone containing hot air, a vertically ascending plume and a dense gravity current are respectively observed in either zone. The exchange flow model proposed by Dalziel [15], and extended by Dalziel and Lane-Serff [16] to problems of architectural fluid mechanics, connects two halves of the problem. Because each of the connected regions is confined (i.e. has finite volume) the dynamics of each zone is highly coupled to the other. Thus the gravity current is reflected from the end wall and propagates back towards the opening in the form of an internal bore. When the bore reaches the opening, the details of the (previously time-independent) exchange flow are significantly altered; this in turn changes the source volume,

momentum and buoyancy flux of the plume that ascends through the dense zone. A model describing these dynamics is assembled by judiciously combining the previous analyses of Benjamin [12], Klemp et al. [14], Baines and Turner [7], Germeles [11], Dalziel [15] and others. An important prediction of this model is that the velocity and density jump across the first front steadily decrease once the exchange flow becomes transient. We thereby consider a qualitatively different scenario from that examined in related studies (e.g. [9, 10]) in which case the source conditions are constant for all time and likewise also the density jump across the first front.

In this preliminary study, we focus specifically on instances where the first front stops its downward descent above the level, $z = h$, of the plume source, if only by a vanishingly small amount. In the context of Figure 2-1, our analysis is therefore most applicable for large ℓ/L and small h/H. Further quantitative details are given by the phase plane diagram of Figure 2-6b. With reference to this figure, we intend to report in a follow-up study upon the flow dynamics in the region above the thick solid curve where the first front is predicted to reach, and possibly exceed, the level $z = h$.

By increasing the doorway height, h, for a certain length, ℓ, the exchange flow rate increases. Thus the dense gravity current travels faster, the reflected bore arrives more rapidly at the opening and the transition to a transient flow regime occurs sooner. Similarly, the gravity current that forms along the upper boundary of the dense zone and that is comprised of fluid discharged from the ascending plume also travels more quickly. The plume meanwhile does not rise strictly vertically as is assumed by our model equations but rather becomes inclined [34]. When h/H is relatively large, we typically see a less favorable comparison between the measured and predicted density stratification in the dense zone (see in particular Figure 2-12 where by virtue of the previous assumptions, our model equations cannot be applied for h/H larger than approximately 0.4; see also Figure 2-13). On the other hand, when considering the terminal buoyancy in the dense zone, which is obtained by integrating the aforementioned density profile, generally positive agreement is noted even for large h/H (Figure 2-14).

Likewise, we find that our predictions for the gravity current speeds match well with laboratory experiments in a broad region of the parameter space (Figure 2-11). So although accurately predicting the details of the dense side stratification remains challenging when the opening is made to be a significant fraction of the zone height, our model equations are otherwise encouragingly robust in their predictive capabilities.

Notwithstanding this generally positive agreement between theory and experiment, it should be emphasized that there are, in the context of real architectural flows, a number of simplifying assumptions that have been applied whose relaxation provides a fruitful area for further inquiry. Firstly, in contrast to our theoretical model and analogue laboratory experiments, the doorway width, w, is, in real buildings, almost always less than the width, W, of the building zone. When $w/W < 1$, the plume source conditions will be slightly different from those studied here. Also, the top and bottom gravity currents will initially propagate both along and across the width of the zone. Moreover, in real buildings, whether mechanically- or naturally-ventilated, localized mixing may occur e.g. due to fans and related HVAC components or the thermal plumes that rise from computer hardware, building occupants or a patch of sunlit floor-space.

Other extensions of the present investigation include examining circumstances where the first front reaches the source (Figure 2-6). In these cases, the fluid density in the dense zone at the level of the source will experience an abrupt decrease when the first front reaches or crosses the level $z = h$. Thus, in addition to the change of flow behavior that occurs when $t = t_2$, the plume buoyancy flux will experience another sudden change. We believe that the composite model outlined in Section 2.2 should be sufficient for elucidating the pertinent flow details; however, no such calculations have yet been attempted. In future we also plan to consider instances where ℓ is either much larger or much smaller than L, mimicking, for example, a small shop connected to a much larger atrium. In these instances of geometric asymmetry between the adjacent zones, it is likely that either the dense or light gravity current of Figure 2-1 will begin to decelerate before it reaches its associated end wall. Thus in the circumstance

where ℓ/L is small, equations such as (2-12), which predicts the magnitude of t_2 assuming constant front speeds, will have to be suitably modified.

Appendix 2-A

In Appendix 2-A we relate the bore amplitude, h_b, to the bore velocity, u_b. In this regard, the flow of interest is sketched in a stationary reference frame in Figure 2-A-1a. This schematic shows a gravity current with constant depth that is reflected from an end wall resulting in an internal bore that propagates from right-to-left with height h_b and speed u_b. If we follow Klemp et al. [14] and change the reference frame to one in which the frame moves with the bore speed, then the upstream lower and upper layer flow speeds are $u_1 + u_b$ and $u_b - u_1'$, respectively (Figure 2-A-1b).

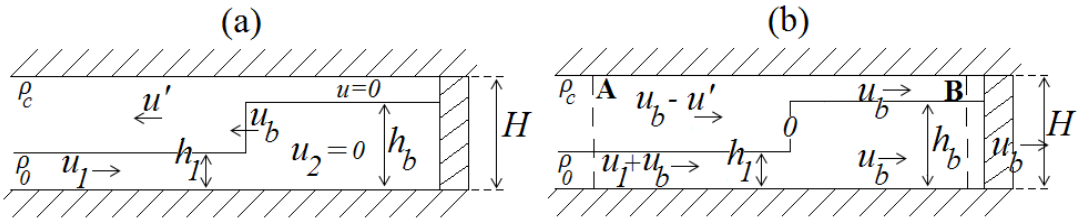

Figure 2-A-1. Schematic illustration of flow reflection from a vertical wall, showing an internal bore propagating upstream away from the wall. (a) Stationary reference frame and (b) translating reference frame.

With reference to Figure 2-A-1b, we apply mass conservation in the upper and lower layers and find that

$$u_b - u' = \frac{u_b(H - h_b)}{(H - h_1)} \tag{2-A-1}$$

and

$$u_b + u_1 = \frac{u_b h_b}{h_1} \tag{2-A-2}$$

Considering a control volume consisting of two vertical planes downstream at A and upstream at B and the top and bottom boundaries of the building zone, the integral form of the horizontal force-balance equation can be written as

$$\int_0^H (P_B - P_A)dz = \int_0^H (\rho u^2)_A - (\rho u^2)_B dz \qquad \text{(2-A-3)}$$

In the above equation the pressure difference between A and B is given by

$$P_A - P_B = \begin{cases} \Delta p_H & 0 < z < h_1 \\ \Delta p_H + (\rho_0 - \rho_c) g z h_1 < z < h_b \\ \Delta p_H h_b < z < H \end{cases} \qquad \text{(2-A-4)}$$

where Δp_H is the pressure difference between A and B along the upper boundary. By substitution of (2-A-4) into (2-A-3), the momentum equation reduces to

$$\left[-\frac{h_b}{h_1} + \frac{\rho_c}{\rho_0}\frac{H - h_b}{H - h_1}\right] u_b^2 (h_b - h_1) + \frac{1}{2} g'(h_b^2 - h_1^2) - \frac{\Delta p_H H}{\rho_0} = 0 \qquad \text{(2-A-5)}$$

Equations (2-A-1), (2-A-2) and (2-A-5) are three equations with four unknowns u', h_b, u_b, and Δp_H. In order to close the system, some description of energy dissipation is needed. In this vein, three different approaches have been suggested by Yih and Guha [21], Wood and Simpson [22] (in both of each the energy is dissipated in the bottom layer), and Klemp et al. [14] (in which the energy is dissipated at the top layer). Each of these approaches, and their respective underlying assumptions, has its merits and demerits. Here, we favor the model of Klemp et al. [14] (i) because of its consistency with Benjamin's analysis in the limit of large amplitude bores, and, (ii) because of the close connection in our study between the bore and the gravity current. Employing Klemp et al.'s approach, i.e. applying Bernoulli's equation along the bottom of the channel, yields:

$$\Delta p_H = \frac{1}{2}\rho {u_b}^2 \left[1 - \frac{{h_b}^2}{{h_1}^2}\right] + (\rho_1 - \rho_2) g (h_b - h_1) \qquad \text{(2-A-6)}$$

Substituting this result into the momentum equation (2-A-5) gives the desired result, namely (2-15).

Appendix 2-B

We have modified Germeles' numerical scheme to account for a transient exchange flow after the reflected internal bore reaches the opening. For $t \geq t_2$, it

is important, for reasons of numerical stability, to ensure that the CFL condition is satisfied. Stated differently, the Germeles [7] algorithm applies an explicit time discretization and it is necessary to verify that the local Courant number remains less than unity in order to avoid possible numerical instabilities. Given that the ambient stratification evolves in time according to (2-19d), the layers are rebuilt at every time step. We have therefore defined a layer-specific Courant number, Cr_i, as

$$Cr_i = \frac{\left(\frac{Q_i}{\ell}\right)\Delta t}{\Delta z_i} \tag{2-A-7}$$

where Δt is the time step, Q_i/ℓ is the velocity of a given layer and Δz_i its depth. If $Cr_i > 1$ anywhere on the domain, then we adaptively define a new time step as $\Delta t_{new} = \frac{0.9\,\Delta z_{i,max}}{(Q_{i,max}/h)}$. The maximum value of Cr_i is then determined and further adjustments to the numerical value of Δt_{new} are made as necessary.

References

[1] Hunt GR, Van den Bremer TS. Classical plume theory: 1937–2010 and beyond. IMA J Appl Math 2011;76:424-448.

[2] Sandbach SD, Lane-Serff GF. Transient buoyancy-driven ventilation: Part 1. Modelling advection. Build Environ 2011;46:1578-1588.

[3] Mingotti N, Chenvidyakarn T, Woods AW. The fluid mechanics of the natural ventilation of a narrow-cavity double-skin facade. Build Environ 2011;46:807-823.

[4] Kaye NB, Flynn MR, Cook MJ, Ji Y. The role of diffusion on the interface thickness in a ventilated filling box. J Fluid Mech 2010;652:195-205.

[5] Merci B, Maele K. Numerical simulations of full-scale enclosure fires in a small compartment with natural roof ventilation. Fire Safety J 2008;43:495-511.

[6] Linden PF, Lane-serff GF, Smeed DA. Emptying filling boxes: the fluid mechanics of natural ventilation. J Fluid Mech 1990;212:309-335.

[7] Baines WD, Turner JS. Turbulent buoyant convection from a source in a confined region. J Fluid Mech 1969;37:51-80.

[8] Phillips JC, Woods AW. On ventilation of a heated room through a single doorway. Build Environ 2004;39:241-253.

[9] Caulfield CP, Woods W. The mixing in a room by localized finite-mass-flux source of buoyancy. J Fluid Mech 2002;471:33-50.

[10] Kuesters AS, Woods W. The formation and evolution of stratification during transient mixing ventilation. J Fluid Mech 2010;670:66-84.

[11] Germeles AE. Forced plumes and mixing of liquids in tanks. J Fluid Mech 1975;71:601-623.

[12] Benjamin TB. Gravity currents and related phenomena. J Fluid Mech 1968;31:209-248.

[13] Shin JO, Dalziel SB, Linden PF. Gravity currents produced by lock exchange. J Fluid Mech 2004;521:1-34.

[14] Klemp JB, Rotunno R, Skamarock WC. On the propagation of internal bores. J Fluid Mech 1997;331:81-106.

[15] Dalziel SB. Two-layer hydraulics: a functional approach. J Fluid Mech 1991;223:135-163.

[16] Dalziel SB, Lane-serff G. The hydraulics of doorway exchange. Build Environ 1991;26:2:121-35.

[17] Wilson DJ, Kiel DE. Gravity driven counter flow through an open door in a sealed room. Build Environ 1990;25:379-388.

[18] Holford JM, Hunt GR. The dependence of the discharge coefficient on density contrast - experimental measurements. 14th Australian Fluid Mechanics Conference, Adelaide University, Adelaide, Australia, 2001.

[19] Hunt GR, Kaye NG. Virtual origin correction for lazy turbulent plumes. J Fluid Mech 2001;435:377-396.

[20] Simpson JE. Gravity Currents: in the environment and the laboratory.2nd ed. Cambridge University Press;1999.

[21] Yih CS, Guha CR. Hydraulic jump in a fluid system of two layers. Tellus 1955;7:358-366.

[22] Wood IR, Simpson JE. Jumps in layered miscible fluids. J Fluid Mech 1984;140:329-342.

[23] Morton BR, Taylor GI, Turner JS. Turbulent gravitational convection from maintained and instantaneous sources. J Fluid Mech 1956;234:1-23.

[24] Kotsovinos NE. A study of the entrainment and turbulence in a plane buoyant jet. Report No. KH-R-32, California Institute of Technology, Keck Laboratory, Pasadena, Calif., Aug., 1975.

[25] Rouse H, Yih C, Humphreys H. Gravitational convection from a boundary source. Tellus 1952;4:200-210.

[26] Killworth PD, Turner JS. Plumes with time-varying buoyancy in a confined region. Geophys Astro Fluid 1982;20 (3-4):265-291.

[27] Bolster D, Caulfield CP. Transients in natural ventilation-A time-periodically- varying source. Building Serv Eng Res Technol2008;29,2:119-135.

[28] Linden P. The fluid mechanics of natural ventilation. Annu Rev Fluid Mech 1999;31:201-238, 1999.

[29] Tatcher TL, Wilson DJ, Wood EE, Craig MJ, Sextro RG. Pollutant dispersion in a large indoor space: Part 1 – Scaled experiments using a water-filled model with occupants and furniture. Indoor Air 2004;14: 258–271.

[30] Taylor JR. An introduction to error analysis: The study of uncertainties in physical measurements. 2nd ed. University Science Books; 1997.

[31] Lowe RJ, Linden PF, Rottman JW. A laboratory study of the velocity structure in an intrusive gravity current. J Fluid Mech 2000;456:33-48.

[32] Huppert HE, Simpson JE. The slumping of gravity currents. J Fluid Mech 1980;99:785-799.

[33] Rottman JW, Linden PF. Gravity Currents. In: Grimshaw R, editor. Environmental stratified flows. Dordrecht: Kluwer Academic Publishers; 2003, p. 89-118.

[34] Lane-Serff, GF, Linden PF, Hillel M. Forced angled plumes. J Haz Mat 1993;33:75-99.

Chapter 3

Influence of geometric parameters on the eventual buoyancy stratification that develops due to architectural exchange flow

3.1 Introduction

Buildings' contribution to overall energy consumption in the United States is approximately 40%, 45% of which is attributed to space heating and 25% of which is attributed to space cooling [1]. Approximately 30% of the energy consumed within the built environment is used inefficiently or unnecessarily [2]. Moreover, 17% of greenhouse gas (GHG) emissions are attributed to commercial

buildings [2]. This necessitates a fundamental reconsideration in the way we operate buildings today. HVAC systems consume significant energy whereas designs that favor passive heating/cooling offer potentially lucrative savings [3-5]. It should be emphasized that using passive design is favored in certain climates and in select regions [6].

Many buildings include equator-facing windows or attached solaria. The associated solar gains create temperature differences between building zones, which results in interior exchange flows. Making efficient use of the heat collected by solaria requires a detailed understanding of the fluid dynamics due to such flows [5-8].

In this spirit, Nabi and Flynn [9] and others [11-19], analyzed the doorway exchange flow between two confined zones. They showed that this exchange flow is characterized by a buoyant plume that ascends in the zone initially containing the cold dense air (i.e. the dense zone). The process by which the plume interacts with the dense zone ambient fluid through entrainment and boundary discharge, i.e. the lateral flow of discharged plume fluid along the ceiling, is referred to as the filling-box model [20]. Accordingly discharged plume fluid is, over time, advected downwards towards the plume source. An appreciable fraction of this discharged plume fluids is re-entrained into the ascending plume, rendering the fluid that is discharged at a subsequent time step less dense than that from before. In this way, a nontrivial stratification is realized. The horizontal boundary between the buoyant upper layer and the layer of dense fluid below is called the first front, whose time-dependent elevation is denoted by z_{ff}.

Nabi and Flynn's study [9] was not restricted to the dense zone. They also considered the adjacent zone, initially containing the warm light air (i.e. the light zone) wherein a dense gravity current propagated away from the opening, was reflected from an end wall then reflected as an internal bore back towards the doorway opening. When the internal bore reached the doorway, say at $t = t_2$ where t denotes time, a marked drop in the exchange flow rate was predicted. In Figure 3-1, panels b, c, f, and g show the horizontal gravity current and reflected internal bore flow and also the vertically ascending plume. Figure 3-1 also shows

the geometric parameters used in this study e.g. h, H, ℓ, L. ρ_0 and ρ_c are the initial densities of the dense and light zones, respectively.

Panels d and h in Figure 3-1 indicate the long-time stratification in the adjacent zones. R represents, the non-dimensional distance between the first front and the top of the doorway, i.e.

$$R = \lim_{t\to\infty}\left(\frac{z_{ff}-h}{H}\right) \qquad (3\text{-}1)$$

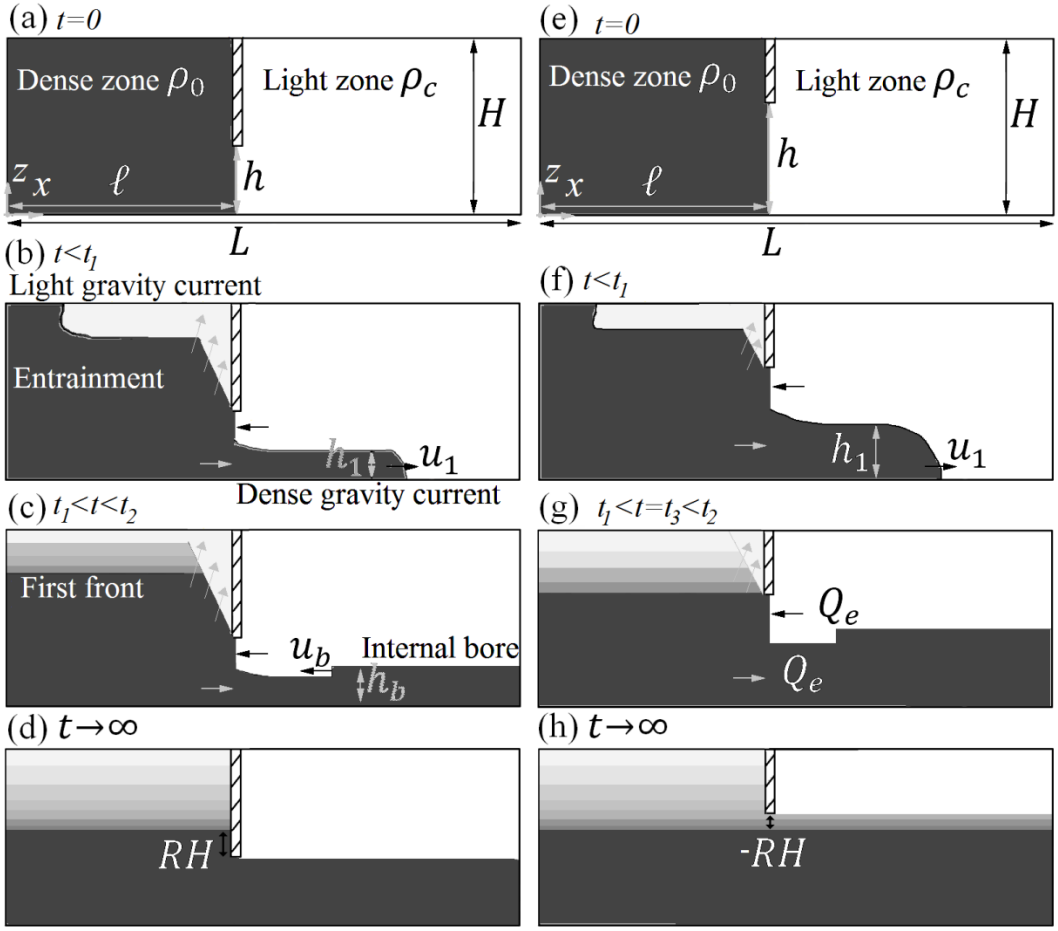

Figure 3-1. The evolution of stratification in adjacent building zones for two different doorway heights. The dimensions h, H, ℓ, L are as defined. Panels a-d and e-h show cases in which $R > 0$ and $R < 0$, respectively. In Figure 3-1g $t_3 < t_2$; however, depending on geometric parameters it is possible that $t_3 > t_2$. Here, t_2 is defined by (3-6) and t_3 is the time required for the first front to reach the top of the doorway.

Two regimes can be identified. For large ℓ/L and for small h/H, the first front descends slowly and its terminal elevation is likely to lie above the plume source

at $z = h$; thus $R > 0$. Conversely for small ℓ/L and for large h/H, the first front is likely to reach and surpass the top of the doorway in a finite time t_3 so that $R < 0$.

Although Nabi and Flynn's investigation (Chapter 2) confirmed the highly interrelated evolution of the density stratification within the adjacent zones, this previous study was limited to $R > 0$ regime. Therefore, the terminal density stratification in the light zone consisted of a uniform layer of dense fluid underlying a uniform layer of light fluid as shown in Figure 3-1d. Having devoted chapter to the former scenario, we now concern ourselves with the $R < 0$ regime and its associated complications. For instance, as we outline more carefully in Section 3.2, when the first front descends below the top of the doorway at a finite time, t_3, some fraction of this stratified dense zone ambient fluid will flow as an intrusive gravity current into the adjacent zone. Moreover, for $t > t_3$ there is a noticeable drop in the buoyancy flux associated with the plume. Hence, the nature of the exchange flow is nontrivially different for $t < t_3$ versus $t > t_3$.

The rest of the Chapter is organized as follows: We develop our analytical model in Section 3.2. The similitude experimental setup is explained in Section 3.3 along with preliminary observations. In Section 3.4, the comparison between the present model and measurements is given. The application of our results to attached solaria design is also discussed. Conclusions and ideas for future work are presented in Section 3.5.

3.2 Analytical model

In this section a model that describes the exchange flow between two confined zones is developed. After articulating the underlying assumptions, the governing equations and predictions are then presented.

3.2.1 Preliminaries

Consistent with our previous study [9], the model is predicated on the following assumptions.

1. The flow is Boussinesq, i.e. $\Delta\rho/\rho \lesssim 0.1$.

2. The fabric of the building is assumed to be perfectly insulating, so that there are no fabric heat losses or gains through ceiling or floor. Such heat transfer is significant only when the aforementioned assumptions do not apply and is modeled elsewhere [10].
3. The plume is everywhere fully turbulent. In the stably stratified dense zone ambient fluid, whose stratification details evolve in time, mixing by anything other than plume entrainment is ignored.
4. The entrainment velocity is proportional to the local centerline vertical velocity of the plume [21]. For a one-sided line plume, Nabi and Flynn [9] reported as the numerical value of the entrainment parameter α =0.14. The plume density and vertical velocity are assumed to satisfy Gaussian distributions.
5. The plume origin is located at the top of the doorway with a non-zero volume flux and the plume rises vertically from this source. This assumption in particular is rather delicate; its validity will be discussed later in Section 3.4.
6. Both zones of Figure 3-1 are rectangular. The governing equations can be extended to other geometries in a straightforward manner [20]. However, so that the flow conforms to a filling-box type rather than a convective overturning type flow, we limit our model to cases where the length of the dense zone is at least as large as its depth. Also, we restrict attention to cases where the doorway spans the width of the building zones. Based on the analysis of Dalziel and Lane-Serff [22], we expect qualitatively similar flow behavior for cases where the doorway width is smaller than that of the building zone.

The bottom propagating gravity current of Figure 3-1 is taken to travel with constant speed from left to right. The analysis of Benjamin [23] relates the gravity current speed, u_1, to its depth, h_1, i.e.

$$\frac{{u_1}^2}{g_0' H} = \frac{h_1(H-h_1)(2H-h_1)}{H^2(H+h_1)} \tag{3-2}$$

Here $g_0' = g\left(\frac{\rho_0 - \rho_c}{\rho_{00}}\right)$ is the initial reduced gravity where g and ρ_{00} are respectively gravitational acceleration and a reference density. In writing (3-2), we scaled the velocity with H instead of h_1 as originally presented by Benjamin. Having applied mass and momentum continuity, Benjamin did not close the problem definitively; indeed, he claimed that a solution supplemented by conservation of energy "would be difficult, if not impossible, to produce experimentally" [23]. Here, we use Benjamin's equation but supplement it with an expression that relates the gravity current volume flux and the exchange flow rate. This assumes a balance between entrainment and detrainment, which we believe to be reasonable in the present circumstances.

The volume flux carried by the gravity current is thus given by

$$u_1 h_1 = Q_e \tag{3-3}$$

where Q_e is the volumetric exchange flow rate and is specified in Section 3.2.2. Equation (3-3) provides a second relationship between u_1 and h_1 in terms of Q_e.

The internal bore dynamics are resolved by applying conservation of mass and momentum plus Bernoulli's equation in the expanding layer [24]. Thus, the following equation relating the internal bore speed, u_b, and depth, h_b, can be derived:

$$\frac{{u_b}^2}{g_0' H} = \frac{h_1^2 (H - h_1)(2H - h_b - h_1)}{H^2 (H h_1 + H h_b + {h_1}^2 - 3 h_1 h_b)} \tag{3-4}$$

Ignoring, as before, any entrainment and detrainment of light zone fluid, the flux associated with the internal bore volume is equal to the exchange volume flux i.e.

$$u_b (h_b - h_1) = Q_e \tag{3-5}$$

The time required for the internal bore to reach the horizontal position of the opening is

$$t_2 = (L - \ell)\frac{u_1 + u_b}{u_1 u_b} \tag{3-6}$$

In deriving (3-6) it is assumed that the velocity of propagation for both upper and lower gravity currents is constant and likewise with the reflected internal bore. For ℓ/L not too large or too small this assumption is reasonable [25]. Once the front has travelled approximately ten lock lengths, there is a

transition that takes place whereby the front speed drops abruptly. Therefore, throughout we restrict our attention to the architecturally realistic scenario whereby $0.10<\ell/L<0.90$

3.2.2 Model equations

The equations describing the evolution of the flux of volume, Q, momentum M, and buoyancy F within the ascending plume read [21]

$$\frac{dQ}{dz} = \sqrt{2}\alpha\frac{M}{Q} \tag{3-7-a}$$

$$\frac{dM}{dz} = \sqrt{\frac{1+\lambda^2}{2}}\frac{FQ}{M} \tag{3-7-b}$$

$$\frac{dF}{dz} = Q\frac{\partial \Delta_{a,0}}{\partial z} \tag{3-7-c}$$

where λ, as turbulent Schmidt number, is an empirical constant equal to 1.16 [26]. Conversely, dense zone ambient stratification evolves according to an advection equation that reads [20]

$$\frac{\partial \Delta_{a,0}}{\partial t} = U\frac{\partial \Delta_{a,0}}{\partial z} \tag{3-8}$$

in which U is the velocity at which individual layers within the upper stratified layer are advected downwards. Here, by individual layers, we have in mind plume fluid discharged over a particular time interval; note that the density of a particular layer does not change with time though its thickness steadily decreases due to entrainment.

These layers have a density (or reduced gravity) that is characterized by

$$\Delta_{a,0} = g\left(\frac{\rho_{a,0}-\rho_0}{\rho_{00}}\right) \leq 0 \tag{3-9}$$

$\rho_{a,0}$ is the dense zone ambient density. We assume that $\Delta_{a,0} = 0$ as the initial condition, which means that $\rho_{a,0} = \rho_0$ for all z at $t = 0$. Likewise, in light zone $\rho_{a,c} = \rho_c$, where $\rho_{a,c}$ is the density of the light zone.

Figure 3-2 indicates that $R < 0$ admits two further possibilities. For large h/H (and also small ℓ/L), the first front descends below the top of the doorway before the internal bore reaches the doorway, i.e. $t_3/t_2 < 1$ (where t_3 is the time

required for the first front to reach the top of the doorway). Conversely for moderate h/H (and moderate ℓ/L), $t_3/t_2 > 1$. In the following paragraphs, we will develop model equations for both scenarios. Differences between the two cases are largely (though not exclusively) confined to stratification; (3-2) and (3-4) are not directly influenced by the relationship between t_2 and t_3.

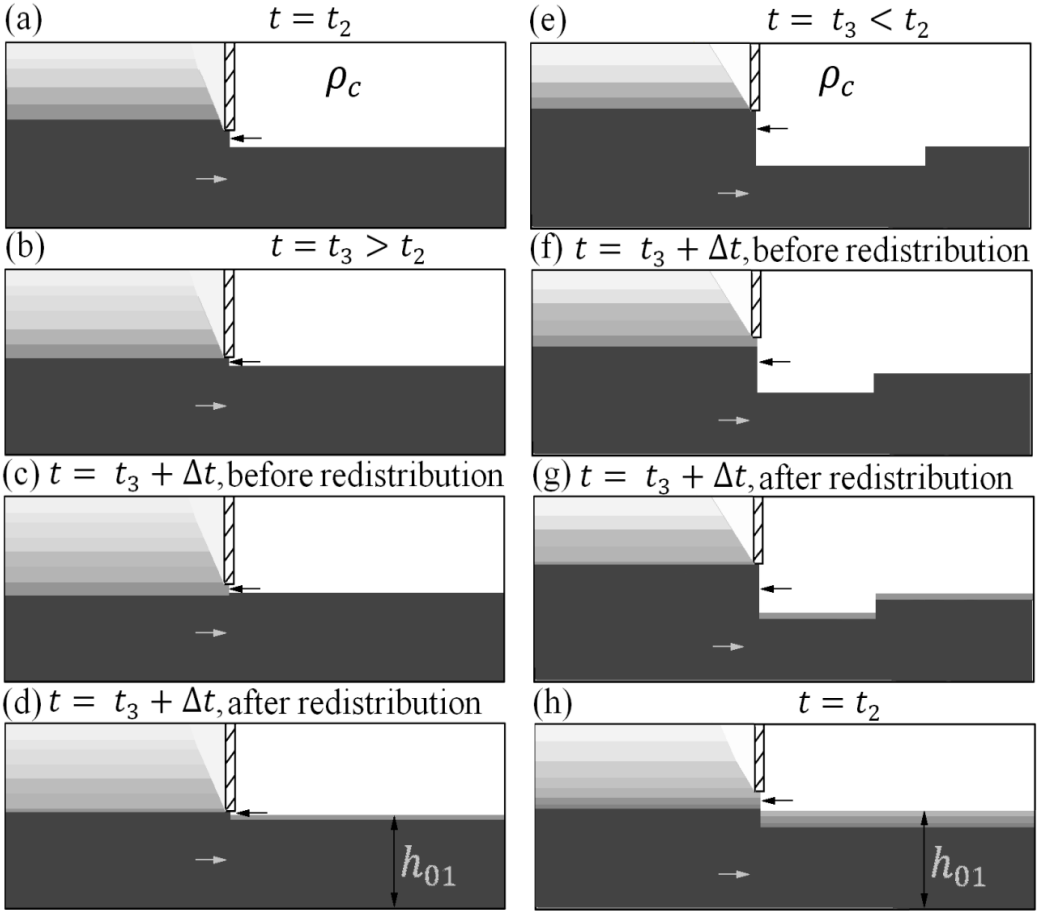

Figure 3-2. Two possible scenarios whereby the first front reaches the top of the doorway after (a-d) and before (e-h) the internal bore reaches the doorway. Panels (b) and (e) illustrate the density stratification for $t = t_3$. At the next time instant, $t_3 + \Delta t$, a new layer of stratified fluid is advected below the top of the doorway as in (c) and (f) which is thereafter redistributed as in (d) and (g).

When z_{ff} falls below h the stratified dense zone ambient fluid continues to evolve in time. However, there is no plume (and no entrainment) below the top of the doorway and therefore layers in the stratified dense zone ambient fluid are advected at a speed Q_e/ℓ. Consequently, the advection speed, U, is defined as

$$U = \begin{cases} \dfrac{Q}{\ell} & h < z \leq H \\ \dfrac{Q_e}{\ell} & z_{ff} \leq z \leq h \end{cases} \tag{3-10}$$

where Q is given by the solution (3-7).

As these layers are advected below the top of the doorway, some fraction of the fluid therein flows into the adjacent zone (Figure 3-2c-d, f-g). In the absence of a universal theory for intrusive gravity currents, the newly-arrived layer at $z < h$ is assumed to spread instantaneously along the interface between the dense lower layer and buoyant upper layer in the light zone. This picture is consistent with Baines and Turner [20] who likewise assume that discharged plume fluid spreads instantaneously after the plume reaches the ceiling. (Note that a similar assumption is applied by Germeles [30], who by introducing discrete layers provided a numerical procedure by which the equations derived by Baines and Turner [20] could be solved efficiently.) Clearly, the redistribution must respect mass conservation i.e. we assume that each aforementioned newly arrived layer is partitioned between the dense and light zones according to the ratio of $\ell/(L-\ell)$. A schematic description of the redistribution process is shown in Figure 3-2.

Linking the two halves of the exchange flow, (3-7) and (3-8) are solved subject to boundary conditions

$$Q = Q_e \tag{3-11-a}$$

$$M = \frac{{Q_e}^2}{h - h_{01}} \tag{3-11-b}$$

$$F = F_e \tag{3-11-c}$$

at $z = h$. Here F_e and h_{01} are, respectively, the source buoyancy flux and the depth of the lower layer (consisting of the dense lower layer and the intermediate stratified layer above it at the doorway. Boundary conditions are all related as we demonstrate below. The buoyancy flux is governed by the difference between ρ_c and $\rho_{a,0}|_{z=h}$ i.e.

$$F_e = \frac{g}{\rho_{00}}\left(\rho_{a,0}|_{z=h} - \rho_c\right)Q_e \tag{3-12}$$

Insofar as the exchange flow, Q_e, is concerned, it is inappropriate, as with (3-12), to compare the fluid densities at $z = h$ because the exchange flow occurs across the entire doorway. Rather, we suppose that Q_e is dictated by the density difference given below:

$$g' = g\left(\frac{\bar{\rho}_{a,0} - \rho_c}{\rho_{00}}\right) \tag{3-13}$$

Here $\bar{\rho}_{a,0}$ is the spatially-averaged density in the dense zone ambient fluid over the vertical expanse of the doorway, i.e. over $0 < z < h$. Due to the evolution of the stratification profile, g' is constant and equal to g'_0 up till t_3, but time variable (and less than g'_0) thereafter as explained in Chapter 2. The exchange flow is respectively critical and subcritical for $t < t_2$ and $t > t_2$ so that [9, 22]

$$Q_e = k(h)h\sqrt{g'h} \qquad t < t_2 \tag{3-14-a}$$

$$Q_e = \frac{8C_d\sqrt{g'}}{\left(\frac{\left(\frac{1}{3}\right)C_d\sqrt{g'}}{L-\ell}(t-t_2) + \frac{2}{\sqrt{h-h_b}}\right)^3} \qquad t \geq t_2 \tag{3-14-b}$$

where the discharge coefficient is taken to be that associated with a sharp-edged orifice or weir and is expressed as [28, 29]

$$C_d = \frac{1}{\left(\frac{311.31}{2\sqrt{2\alpha}}\frac{(h-h_{01})^3 g'}{Q_e^2}\right)^{0.101}} \tag{3-15}$$

and the formula for $k(h)$ reads [22]

$$k(h) = \sqrt{\frac{\left(1-\frac{h_{01}}{h}\right)^3\left(\frac{h_{01}}{h}\right)^3}{\left(1-\frac{h_{01}}{h}\right)^3 + \left(\frac{h_{01}}{h}\right)^3}} \tag{3-16}$$

Finally, h_{01}, is given by [9]

$$\frac{h_{01}}{h} = \begin{cases} \frac{1}{2} + \frac{1}{4}\left(\frac{H}{h}-1\right)^{1/3} - \frac{1}{8}\left(\frac{H}{h}-1\right)^{2/3} & \frac{H}{h} < 2 \\ \frac{5}{8} & \frac{H}{h} \geq 2 \end{cases}, \quad t < t_2 \tag{3-17-a}$$

$$\frac{h_{01}}{h} = 1 - \frac{4}{h\left(\frac{\left(\frac{1}{3}\right) C_d \sqrt{g'}}{L-\ell}(t-t_2) + \frac{2}{\sqrt{h-h_b}}\right)^2}, t \geq t_2 \qquad \text{(3-17-b)}$$

For $t < t_2$, h_{01} is a function only of h/H. The lower dense layer is compromised solely of fluid of density ρ_0 for $t < t_3$ whereas for $t > t_3$ it also consists of the intermediate layers. For further details on equations (3-14) to (3-17) the reader may refer to Chapter 2.

3.2.3 Numerical scheme

The algorithm used for the numerical solution of (3-7) and (3-8) is based on a scheme originally devised by Germeles who developed the layered modeling approach [30]. Germeles's algorithm employs Runge-Kutta and Euler schemes, respectively, for the spatial and temporal discretization. The boundary conditions are updated once the first front falls below the top of the doorway or the internal bore reaches the doorway. In either event, they become transient and it is possible that the plume buoyancy flux becomes vanishingly small, $F \to 0$, before the plume reaches the ceiling (for simplicity, we did not consider this possibility in Figure 3-2). We then limit the spatial domain of integration to $h < z < z_{bal}$ where z_{bal} is the height where $F \to 0$. No plume is defined for $z > z_{bal}$. The evolution of the stratification continues, as before, with the difference that now the upper-most layer appears at z_{bal}.

3.2.4 Model predictions

Figure 3-3 shows a regime diagram obtained by solving (3-7) and (3-8). For R <0 (i.e. to the left of the solid curve of Figure 3-3) t_3 was computed; the dashed curve shows the locus of points for which $t_3 = t_2$.

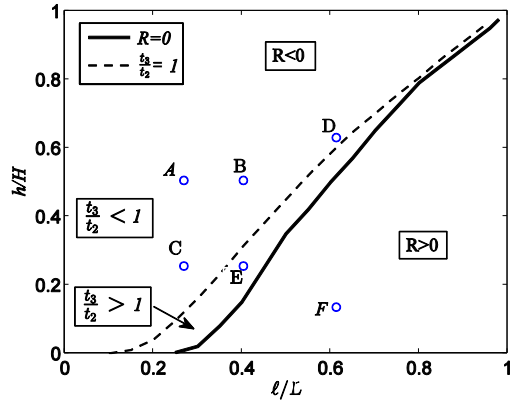

Figure 3-3. Regime diagram of admissible solutions of (3-7) and (3-8). The solid and dashed lines denote $R = 0$ and $t_3 = t_2$, respectively. Points A-F correspond to particular experimental combinations of h/H and ℓ/L (see Section 3.4).

Figure 3-4 shows t_3/t_2 as a function of h/H for various ℓ/L. By increasing ℓ/L, t_3/t_2 likewise increases. The reason is twofold: the horizontal distance traveled by the gravity current and internal bore increases whereas the first front descends more rapidly.

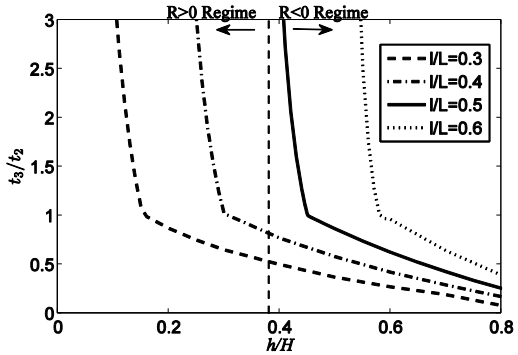

Figure 3-4. Variation of t_3/t_2 with respect to h/H for various ℓ/L. The dashed vertical line shows the transition from $R > 0$ (right) to $R < 0$ (left) regime for ℓ/L=0.5.

When ℓ/L=0.50 and h/H <0.38, the first front never reaches the source and therefore $R > 0$. By increasing h/H, the speed of the bottom gravity current and internal bore both increase and t_2 decreases. However, the first front also descends more rapidly and, of course, the vertical distance between the ceiling and the top of the doorway is diminished. On balance therefore, increasing h/H results in a decrease in t_3/t_2. For fixed ℓ/L, there is a unique value of h/H for which $t_3 = t_2$ i.e. the first front reaches the top of the doorway at the exact instant

that the internal bore reaches the doorway. For ℓ/L=0.50, Figure 3-4 shows that this value is 0.45, which is consistent with Figure 3-3 and indicates a transition from the $t_3/t_2 > 1$ regime to the $t_3/t_2 < 1$ regime. Similar comments can be made for other values of ℓ/L. Therefore, in the following figures we consider only the ℓ/L =0.50 case because this scenario is representative: for 0.10<ℓ/L<0.90, qualitatively similar results are obtained. Both small and large h/H are considered so that t_3/t_2 >1 and t_3/t_2 <1, respectively.

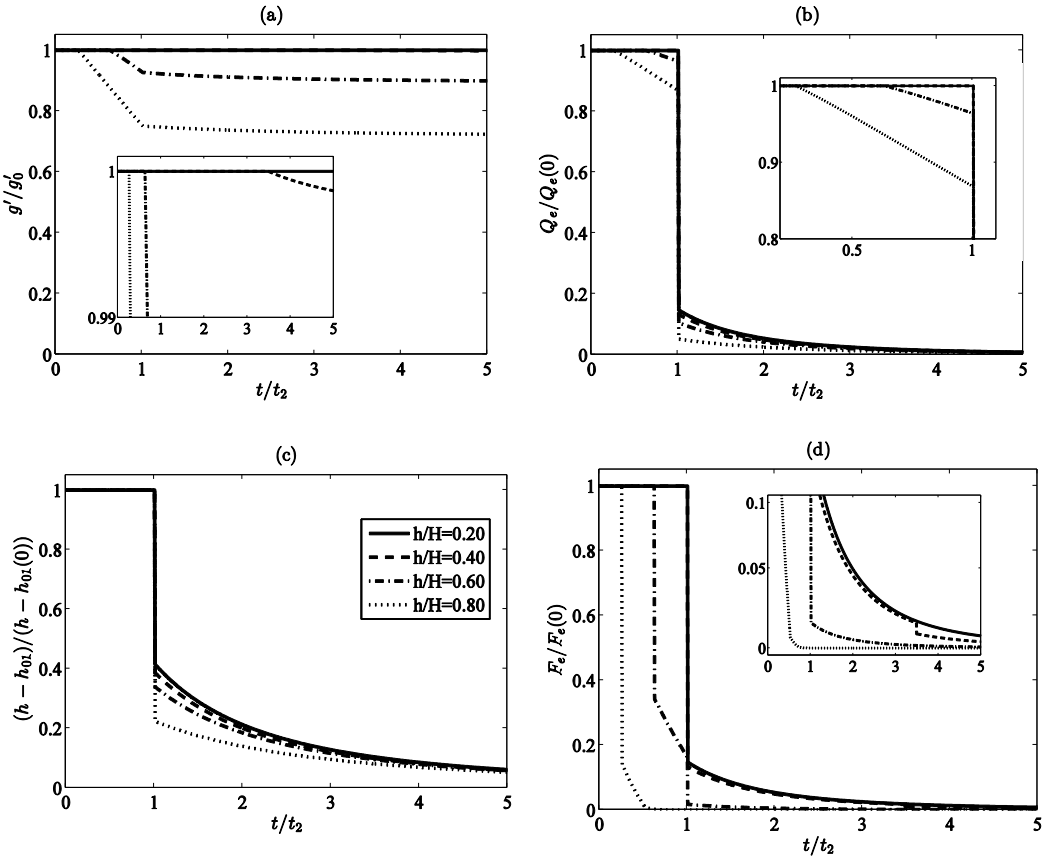

Figure 3-5. Non-dimensional (a) reduced gravity, (b) volume flux, (c) exchange area per unit depth, and (d) buoyancy flux at the doorway with respect to t/t_2 for various h/H. The axes labels for the inset figures are the same as those of the larger figures. For h/H =0.4 t_3/t_2 >1 and for h/H =0.6 and 0.8 t_3/t_2<1. For h/H =0.2, R >0 and t_3 is not defined.

Figure 3-5 shows various exchange flow parameters versus t/t_2 for different h/H. When h/H =0.20, the first front never reaches the top of the doorway. By contrast, when h/H =0.40, 0.60, and 0.80, R <0 and t_3/t_2 =3.48,

0.62, and 0.25, respectively. For all cases, as indicated by Figure 3-5b, the volumetric exchange flow, $Q_e/Q_e(0)$, drops abruptly when $t = t_2$ after which the formerly critical exchange flow becomes transient and sub-maximal decaying to zero in the long time limit. Similar comments apply for Figure 3-5c-d which show, respectively, $\left(h - h_{01}(t)\right)/\left(h - h_{01}(0)\right)$ as a surrogate for the area of the exchange flow, and $F_e/F_e(0)$.

For $t < t_2$ and consistent with the analysis of Dalziel [27], the composite Froude number at the doorway, i.e. $Fr_c^2 = {u_{01}}^2/g_0' h_{01} + {u_{02}}^2/g_0' h_{02}$ equals 1, where u_{01} (u_{02}) and h_{01} (h_{02}) are the velocity and depth of the lower (upper) layer at the doorway. For such a critical flow, h_{01}/h is given by (3-14b) - see Nabi and Flynn [9]. Figure 3-5c clearly shows that $h - h_{01} = h - h_{01}(0)$ for $t < t_2$ which signifies that the exchange flow is critical while for $t > t_2$, $h - h_{01}$ drops abruptly implying a subcritical flow.

For h/H=0.40 ($t_3/t_2 > 1$), as shown by the dashed curve in the inset to Figures 3-5a and d, g' and F_e respectively experience a gradual and sudden, albeit small, decrease at $t = t_3$. Clearly, the change following t_3 is so much less pronounced than that after t_2 that there is little difference between the h/H=0.20 (R >0) and h/H=0.40 (R <0) cases, at least insofar as the variables considered here.

For h/H=0.60 and h/H=0.80 ($t_3/t_2 < 1$), however, the difference is much more striking. Figure 3-5a shows that as soon as the first front falls below the top of the doorway (i.e. $t = t_3$) g' steadily decreases from its initial value of g_0'. Therefore, as shown in Figure 3-5b, the exchange flow rate, Q_e, though critical, becomes transient for $t_3 < t < t_2$. A still more dramatic change is observed in Figure 3-5d, which exhibits a sharp decrease in F_e when $t = t_3$. The reason is that both $\rho_{a,0}|_{z=h}$ and Q_e decrease at t_3, as is evident by (3-12). Both Q_e and F_e decrease again when $t = t_2$ and the flow becomes subcritical.

Figure 3-6 shows, as a function of height and time, the evolution of the dense zone ambient stratification in the dense zone. After t_2 the fluxes decrease abruptly, and the plume is therefore unable to reach the ceiling. As illustrated by

Figure 3-6a and predicted by the model, the advection velocity becomes so small that the first front does not descend significantly below the top of the doorway.

In Figure 3-6b, we consider h/H =0.60 ($t_3/t_2 < 1$). In contrast to Figure 3-6a, we see a much more pronounced stratification in the region below the top of the doorway. The reason is that for $t_3/t_2 < 1$ at $t = t_3$ there is a small decrease in Q_e compared to the more substantial change at $t = t_2$ (Figure 3-5b). Therefore, the vertical advection speed remains relatively large until t_2 and the stratified upper layer in the dense zone is able to penetrate further below the top of the doorway as compared to the $t_3/t_2 > 1$ case.

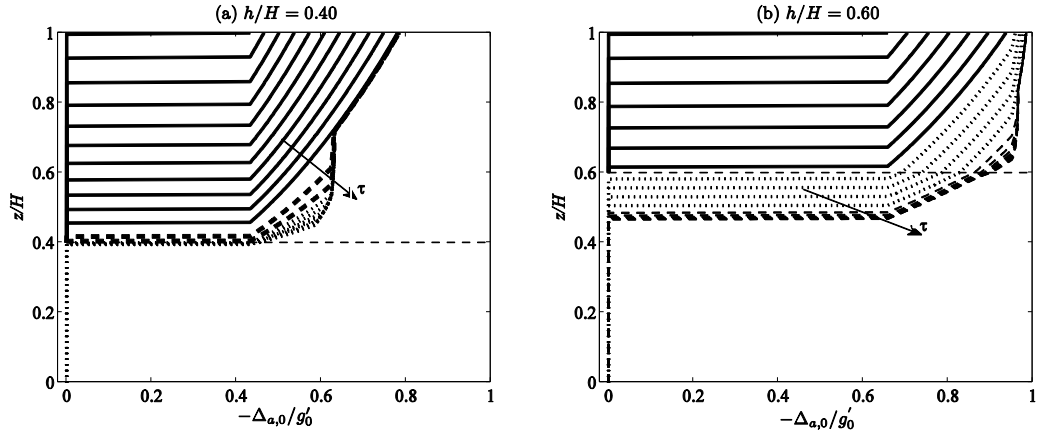

Figure 3-6. Dimensionless stratification profiles at different dimensionless times, where the arrow indicates the direction of increasing $\tau = t/t_2$ wherefor $\Delta\tau$ =0.25 when $t < t_2$ and $\Delta\tau$ =1 when $t \geq t_2$. (a) h/H =0.40, t_3/t_2 =3.48 and (b) h/H =0.60, t_3/t_2=0.62. The dashed curves correspond to $t > t_2$ and the dotted curves correspond to $t > t_3$. The dashed horizontal line indicates to the position of the plume source, i.e. the top of the doorway.

We denote the terminal reduced gravity profiles in the dense and light zones as $\Delta_{a,0}^{\infty}$ and $\Delta_{a,c}^{\infty}$, respectively. Here $\Delta_{a,c}$ is defined as

$$\Delta_{a,c} = g\left(\frac{\rho_{a,c} - \rho_0}{\rho_{00}}\right) \leq 0 \tag{3-18}$$

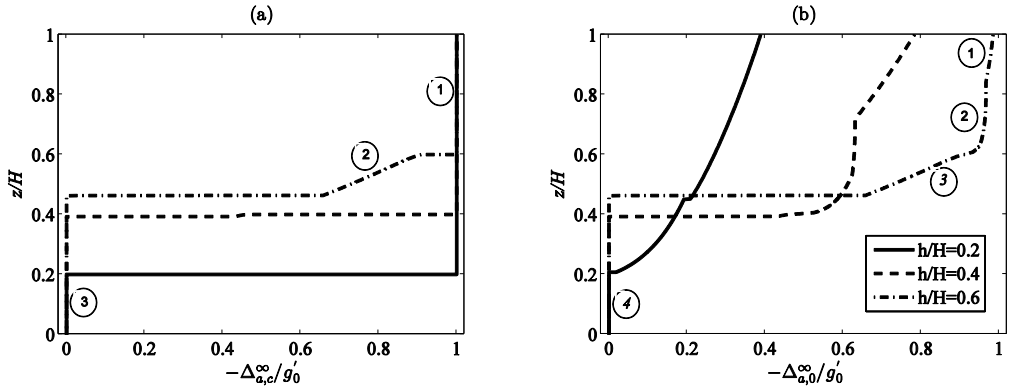

Figure 3-7 (a) Light-zone terminal stratification, $\Delta^{\infty}_{a,c}$, and (b) dense-zone terminal stratification, $\Delta^{\infty}_{a,0}$, versus z/H for ℓ/L = 0.50 and various h/H. Each number corresponds to a layer whose definition is given on page 79.

Figure 3-7 shows $\Delta^{\infty}_{a,0}$ and $\Delta^{\infty}_{a,c}$ non-dimensionalized by $-g'_0$ versus z/H. In principle, for R <0 , $\Delta^{\infty}_{a,c}$ represents a superposition of three layers; a uniform layer of light fluid above $z = h$ with $\Delta^{\infty}_{a,c} = 1$ (layer 1 in Figure 3-7a) a layer of dense fluid with $\Delta^{\infty}_{a,c} = 0$ along the bottom (layer 3) and some intermediate layer of spatially-variable $\Delta^{\infty}_{a,c}$ in between these two layers (layer 2). Note that the intermediate layer thickness is small (appreciable) when t_3/t_2 >1 ($t_3/t_2 < 1$). Similarly, $\Delta^{\infty}_{a,0}$ for the $R < 0$ regime encompasses four layers; Layer 1 corresponds to $z_{bal}/H < z/H < 1$ where for h/H=0.60, z_{bal}/H =0.86. For $t \geq t_2$ the stratification remains frozen in this layer because the plume is unable to ascend beyond z_{bal}. The second layer spans $h/H < z/H < z_{bal}/H$. Here the interaction between the plume and the dense zone ambient fluid continues for $t \geq t_2$. The third layer, which we call the intermediate layer, spans $h/H - |R| < z/H < h/H$ and describes the stratification beneath the plume source. In the $t_3/t_2 < 1$ regime the thickness of this intermediate layer is larger. Referring to Figure 3-7, R =-0.0020 and -0.0778 for h/H =0.40 and 0.60, respectively. The important feature of the terminal stratification profiles is that $\Delta^{\infty}_{a,0}$=$\Delta^{\infty}_{a,c}$ just below the top of the doorway (i.e. layer 2 of Figure 3-7a matches layer 3 of Figure 3-7b). Therefore, for the $t_3/t_2 < 1$ regime, there is a relatively broad range of z, over which $\Delta^{\infty}_{a,0}$ is the same as $\Delta^{\infty}_{a,c}$.

An impetus for examining the details of the vertical stratification is that this allows us to find the heat content or buoyancy in one or the other zone. Thus we define

$$b_0 = \frac{1}{g_0' HL}\int_0^{\ell}\int_0^{H}\left(-\Delta_{a,0}\right)\,dzdx \tag{3-19-a}$$

$$b_c = \frac{1}{g_0' HL}\int_{\ell}^{L}\int_0^{H}\left(-\Delta_{a,c}\right)\,dzdx \tag{3-19-b}$$

The total buoyancy, $b_{tot} = b_0 + b_c$, is time-independent for a closed system. For the initial conditions of $\Delta_{a,0} = 0$ and $\Delta_{a,c} = 1$, $b_0 = 0$ and $b_c = 1 - \ell/L$, hence at any instant $b_{tot} = 1 - \ell/L$. Figure 3-8 shows b_0/b_{tot} versus time for h/H =0.20, 0.40 and 0.60. It can be shown that light zone buoyancy b_c is the mirror image of b_0. There is an abrupt change of slope that is realized when $t = t_2$ and the flow becomes subcritical. Furthermore when h/H is relatively large b_0 is about half of the b_{tot} which implies that $b_0 \to b_c$ in the long time limit whereas these parameters remain distinct when h/H is small.

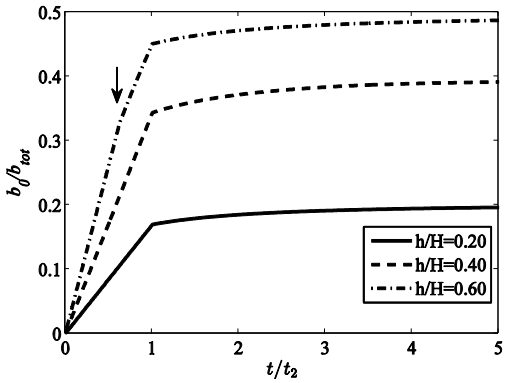

Figure 3-8. Dense zone buoyancy, b_0, versus t/t_2 for ℓ/L = 0.50 and various h/H. For h/H =0.60, the vertical arrows indicate $t = t_3$ whereupon small changes of slope are seen.

3.2.5 Well-mixed model

If one sought to omit the complicating dynamical influence of the interior flows, he or she might instead employ a well-mixed model in which each zone exhibits a spatially-uniform, time-varying density. In this case, the exchange flow is again driven by the difference of density between the two zones, i.e.

$$Q_e = k(h)h\sqrt{\frac{g}{\rho_{00}}(\rho_{a,0}-\rho_{a,c})h} = kh\sqrt{(\Delta_{a,0}-\Delta_{a,c})h} \tag{3-20}$$

where $\Delta_{a,0} \leq 0$ and $\Delta_{a,c} \leq 0$ are now independent of z and solve

$$H\ell\frac{d}{dt}\Delta_{a,0} - Q_e\Delta_{a,c} + Q_e\Delta_{a,0} = 0 \text{ [dense zone]} \tag{3-21-a}$$

$$H(L-\ell)\frac{d}{dt}\Delta_{a,c} - Q_e\Delta_{a,0} + Q_e\Delta_{a,c} = 0 \text{ [light zone]} \tag{3-21-b}$$

respectively.

Starting from the aforementioned initial conditions yields $\Delta_{a,0}(0) = \Delta_{a,c}(0) = -g_0'$. Thus $\Delta_{a,0}$ and $\Delta_{a,c}$ solve the following respective equations

$$\frac{\Delta_{a,0}}{g'} = \left[\left(1+\frac{t}{\tau_{wm}}\right)^{-2} - 1\right]\left(1-\frac{\ell}{L}\right) \tag{3-22-a}$$

$$\frac{\Delta_{a,c}}{g'} = \left[\left(1+\frac{t}{\tau_{wm}}\right)^{-2} + \frac{L-\ell}{\ell}\right]\left(-\frac{\ell}{L}\right) \tag{3-22-b}$$

where τ_{wm} is a characteristic draining time defined by

$$\tau_{wm} = \frac{2H\ell}{kh\sqrt{g_0'h}}\frac{L-\ell}{L} \tag{3-23}$$

Thus, an algebraic equation for Q_e can be derived. Moreover, it can be shown that

$$b_{wm,0} = -\left[\left(1+\frac{t}{\tau_{wm}}\right)^{-2} - 1\right]\left(1-\frac{\ell}{L}\right)\left(\frac{\ell}{L}\right) \tag{3-24-a}$$

$$b_{wm,c} = \left[\left(1+\frac{t}{\tau_{wm}}\right)^{-2} + \frac{L-\ell}{\ell}\right]\left(\frac{\ell}{L}\right)\left(1-\frac{\ell}{L}\right) \tag{3-24-b}$$

$b_{wm,0}$ and $b_{wm,c}$are the buoyancy in dense and light zone given by the well-mixed model, respectively. Consistent with the previous discussion $b_{tot} = 1 - \ell/L$. An explicit comparison between the buoyancy of the well-mixed model given by (3-24) with the buoyancy of stratified model given by (3-19) is deferred to Section 3-4, where the experimental data is also included.

3.3 Experimental setup and observations

3.3.1 Apparatus and procedure

Similitude laboratory experiments were conducted in a glass tank measuring 25.0×34.5×227.5 cm. A vertical barrier served as the lock gate. The fluid depth, H, was 20.0±0.2 cm. The barrier location and the height, h, of removal were adjustable so that various ℓ/L and h/H, i.e. $0.12 \leq h/H \leq 1.00$ and $0.25 \leq \ell/L \leq 0.75$, could be achieved. By employing an electric vinyl light-sheet, the majority of the tank was uniformly backlit. The experimental images were recorded using a LaVision Imager E-lite camera with 35 mm Nikon AF Nikkor lens.

Density differences were produced by addition of sodium chloride and were measured using an Antor Paar DMA 4500 densitometer with a precision of ±0.0001 g/cm^3. Saline ($\rho_0 \simeq 1.0400$ g/cm^3) and fresh water ($\rho_c \simeq 0.9984$ g/cm^3), respectively, served as the dense and light fluid. In a typical experiment, $g_0' = 0.40 \pm 0.02$ m/s^2. The Reynolds number

$$\mathrm{Re} = \frac{\sqrt{g_0' H^3}}{2\nu} \tag{3-25}$$

was large enough, i.e. $1\times10^4 < \mathrm{Re} < 3\times10^4$, so that our experiments admitted flows that were quantitatively similar, insofar as turbulent transport, to those observed in real buildings [9, 31].

We first filled the tank with fresh tap water to a depth of 20.0 ± 0.2 cm. Thereafter, the lock gate was lowered into the tank and salt was added to the lock region. Dye (food coloring) was also added to one or the other side of the gate to aid flow visualization. The gate was then partially removed to a depth h. Detailed gravity current and internal bore speed measurements appear in Nabi and Flynn [9], where the experimental data was (favorably) compared with theory. Herein, we focus our attention on density measurements and stratification details. Thus we used a conductivity probe (Precision and Measurement Engineering, MSCTI) mounted on a vertical traverse (Velmex, X-Slide), whose translational speed was 5 mm/s. The relationship between voltage and density was approximately linear and was calibrated using five samples of known density, which were collected at

the conclusion of a particular experiment by selectively withdrawing fluid at a series of prescribed elevations using a 32.0 cm needle and syringe.

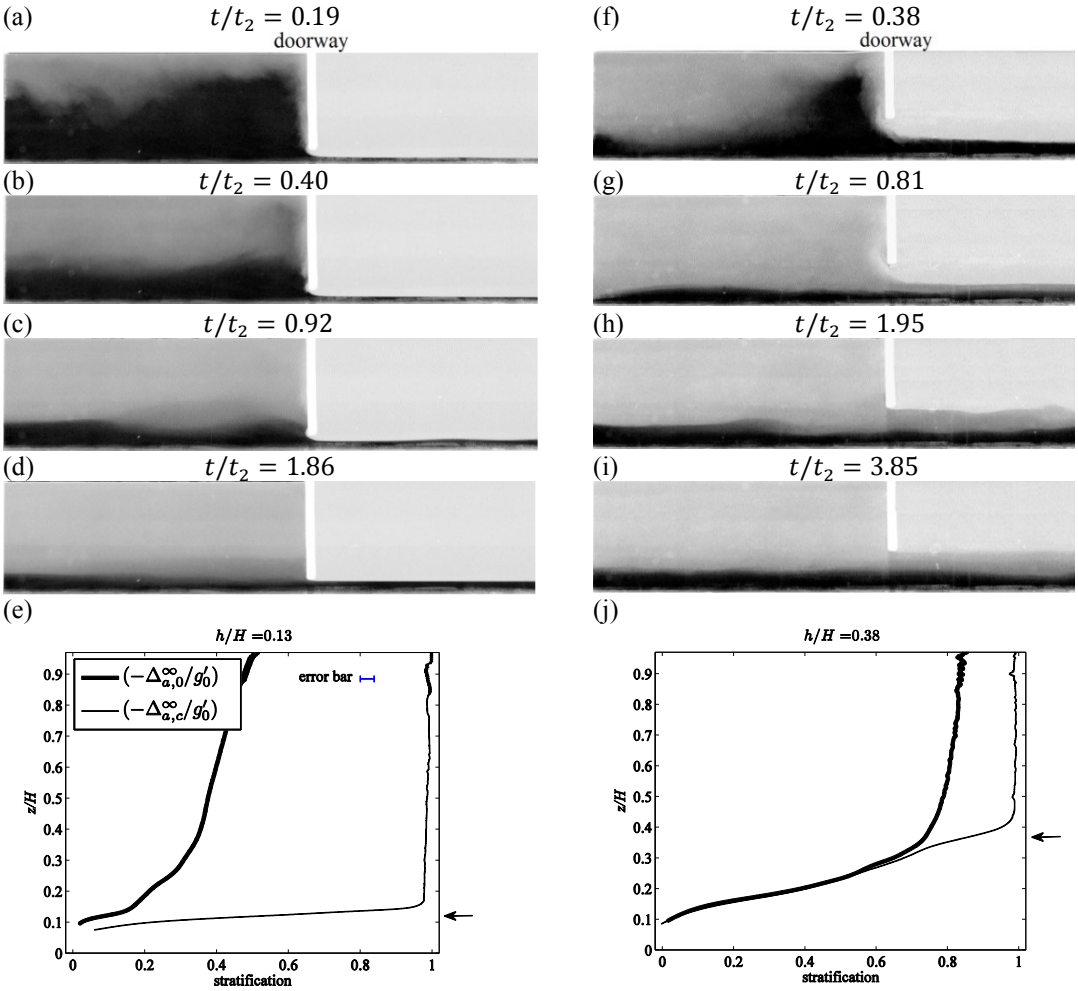

Figure 3-9. Time evolution of the density stratification where, in contrast to Figures 1 and 2, the clear and dark fluid have respective densities ρ_0 and ρ_c. (a-e) h/H =0.13 and (f-j) h/H =0.38. In either case, ℓ/L =0.27. Only part of the field of view (measuring 20 cm tall by 98 cm long) is shown. Although the consecutive figures correspond to different t/t_2, they show the same dimensional times i.e. t =13.5, 28.6, 65.9, and 133.5 s.

Density measurements were made a long time after partially removing the gate. We found that the measured stratifications ceased to vary with time when $t \gtrsim 10t_2$.

3.3.2 Preliminary observations

Figure 3-9 shows the time evolution of the density stratification in both zones. The left- and right-hand side panels correspond, respectively, to the $t_3/t_2 > 1$ and $t_3/t_2 < 1$ regime, where in both cases $R < 0$. Figures 3-9e and j indicate the associated terminal stratification profiles. As shown in Figure 3-9d, for the $t_3/t_2 > 1$ case the terminal elevation of the first front approximately coincides with $z = h$. Two distinct layers are evident in the light zone and a sharp gradient is observed close to the top of the doorway, whose position is indicated by the horizontal arrow in Figure 3-9e. Conversely, when $t_3/t_2 < 1$, the first front falls an appreciable distance below the top of the doorway, and thus a nontrivial stratification develops in both zones. Figure 3-9j demonstrates that $\Delta_{a,0}^{\infty}$ and $\Delta_{a,c}^{\infty}$ are approximately equal below $z = h$. Here and elsewhere, slight deviations between $\Delta_{a,0}^{\infty}$ and $\Delta_{a,c}^{\infty}$ may be due to the fact that there is oftentimes a sharp gradient of density in the vicinity of the doorway rendering the collection of calibration samples there difficult.

Error bars, shown in Figures 3-9e and j, are based on the results of repeat experiments, conducted for select h/H. Uncertainty analyses are based on the standard deviation of an ensemble of measurements with a confidence limit of 68% [32].

3.4 Results and discussions

3.4.1 Comparison between theory and experiment

Regarding $\Delta_{a,0}^{\infty}$ and $\Delta_{a,c}^{\infty}$, there exists an extensive volume of experimental data, therefore only select experiments are analyzed in detail whereas in other cases the interrogation of the data is less intensive.

In Figure 3-3, a series of points labeled A-F are highlighted. The coordinates of each point are listed in Table 3-1, which also provides predictions for t_3/t_2 and R based on the model equations. Working down the table, the speed of the first front decreases. Therefore both R and t_3/t_2 increase. For point F,

$R > 0$; t_3 is undefined. Table 3-1 shows that t_3/t_2 increases with decreasing h/H for fixed ℓ/L and increasing ℓ/L for fixed h/H (see Figure 3-4).

Table 3-1. Coordinate details for the points labeled A-F in Figure 3-3. Note that h/H and ℓ/L values are considered accurate to within 0.01.

point	h/H	ℓ/L	$t_3/t_2\|_{model}$	$R\|_{model}$
A	0.50	0.27	0.32	-0.158
B	0.51	0.40	0.38	-0.110
C	0.25	0.27	0.65	-0.088
D	0.63	0.61	0.89	-0.045
E	0.26	0.40	3.24	-0.007
F	0.14	0.61	N/A	0.034

In Figure 3-10 experimental and model values for $\Delta_{a,0}^{\infty}$ and $\Delta_{a,c}^{\infty}$, which respectively correspond to the terminal stratification in the dense and light zone, are compared for each point of Table 3-1; panel (a) corresponds to point A and so forth. Thus the influence of both h/H and ℓ/L is examined. Also, Figure 3-11 shows the same parameters as Figure 3-10 but with a more specific emphasis on the variation of h/H. Here ℓ/L is fixed at 0.27 and t_3/t_2 is predicted to be 0.95, 0.46, 0.26, 0.16, and 0.10 in panels a-e, respectively.

As shown in Figures 3-10 and 3-11, the model of Section 3.2.2 describes the terminal stratification in the light zone with generally satisfactory accuracy. Thus $(\Delta_{a,c}^{\infty})_{exp}$ and $(\Delta_{a,0}^{\infty})_{exp}$ typically coincide below $z = h$ whose position is indicated by the horizontal arrow; a notable exception is Figure 3-10f for which we believe that the previous discussion of the conductivity probe accuracy in the vicinity of a sharp density interface is relevant (see Section 3.3). By decreasing t_3/t_2, the thickness of the intermediate layer below $z = h$ increases as expected. Consequently, $(\Delta_{a,c}^{\infty})_{exp}$ and $(\Delta_{a,0}^{\infty})_{exp}$ overlap to a much greater extent in, say, panel 10a than 10f.

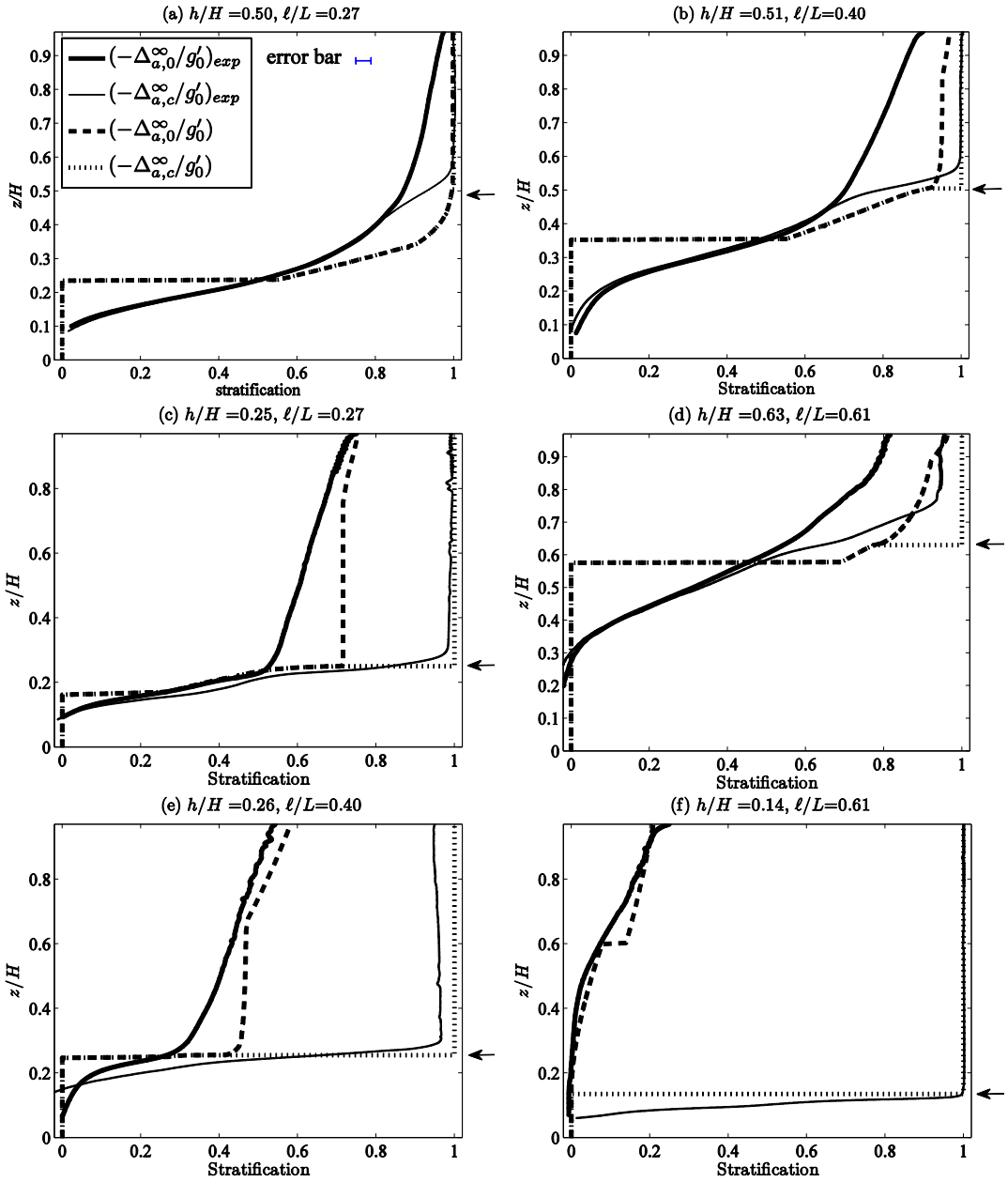

Figure 3-10. Experimental and theoretical stratification profiles for the points A-F of Figure 3-3 and Table 3-1. Representative error bars are as shown in panel a.

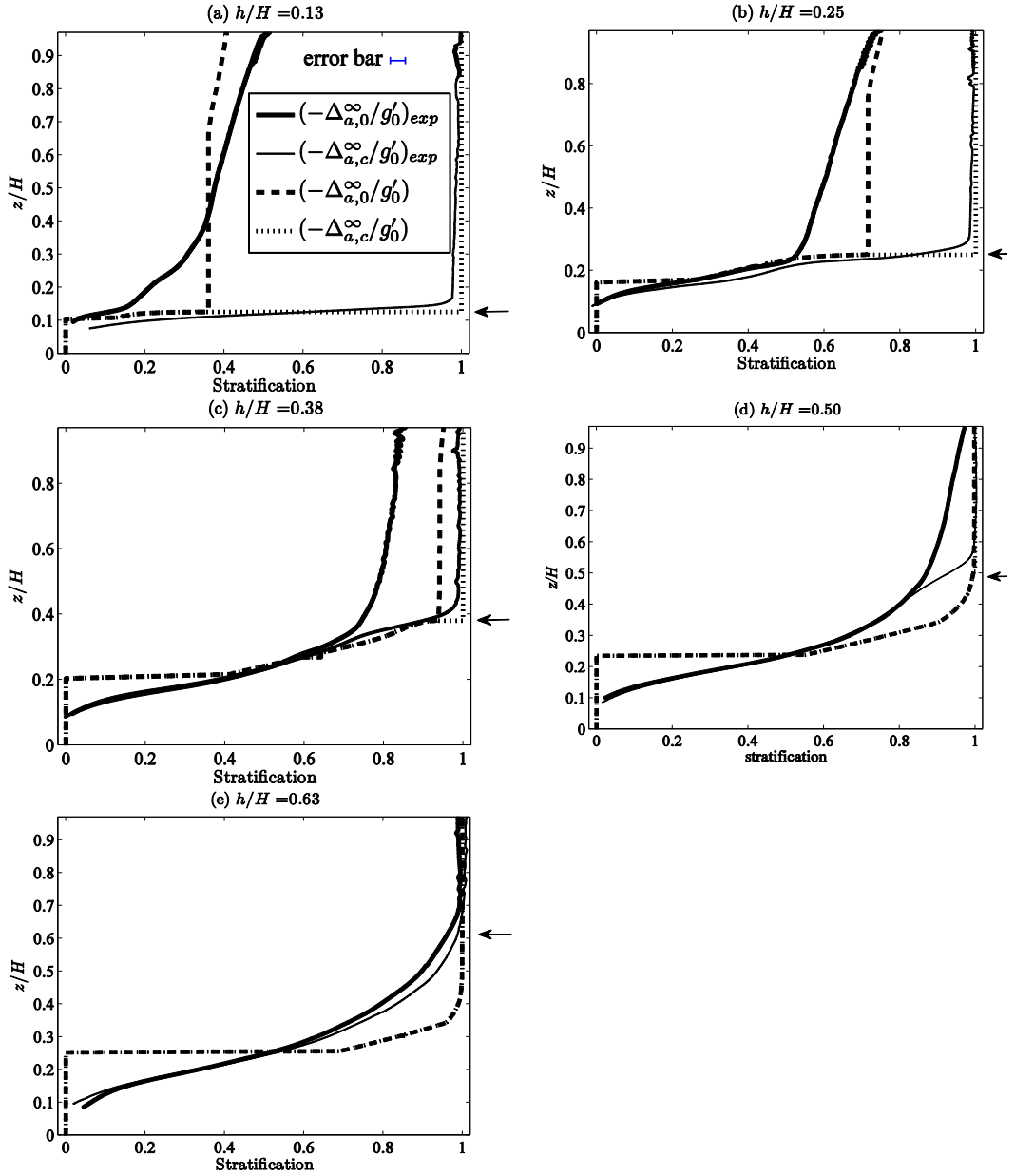

Figure 3-11. As in Figure 3-10 but with ℓ/L =0.27.

Figures 3-10 and 3-11 also highlight another difference between the R >0 and R <0 regimes. In the former (Figure 3-10f), the density below $z = h$ is, in dense zone, essentially constant. By contrast, when R <0, the stratification evolves further below the top of the doorway in the dense zone. Such behavior is more pronounced for larger values of $|R|$ and is evident in both the analytical solutions and their experimental counterparts.

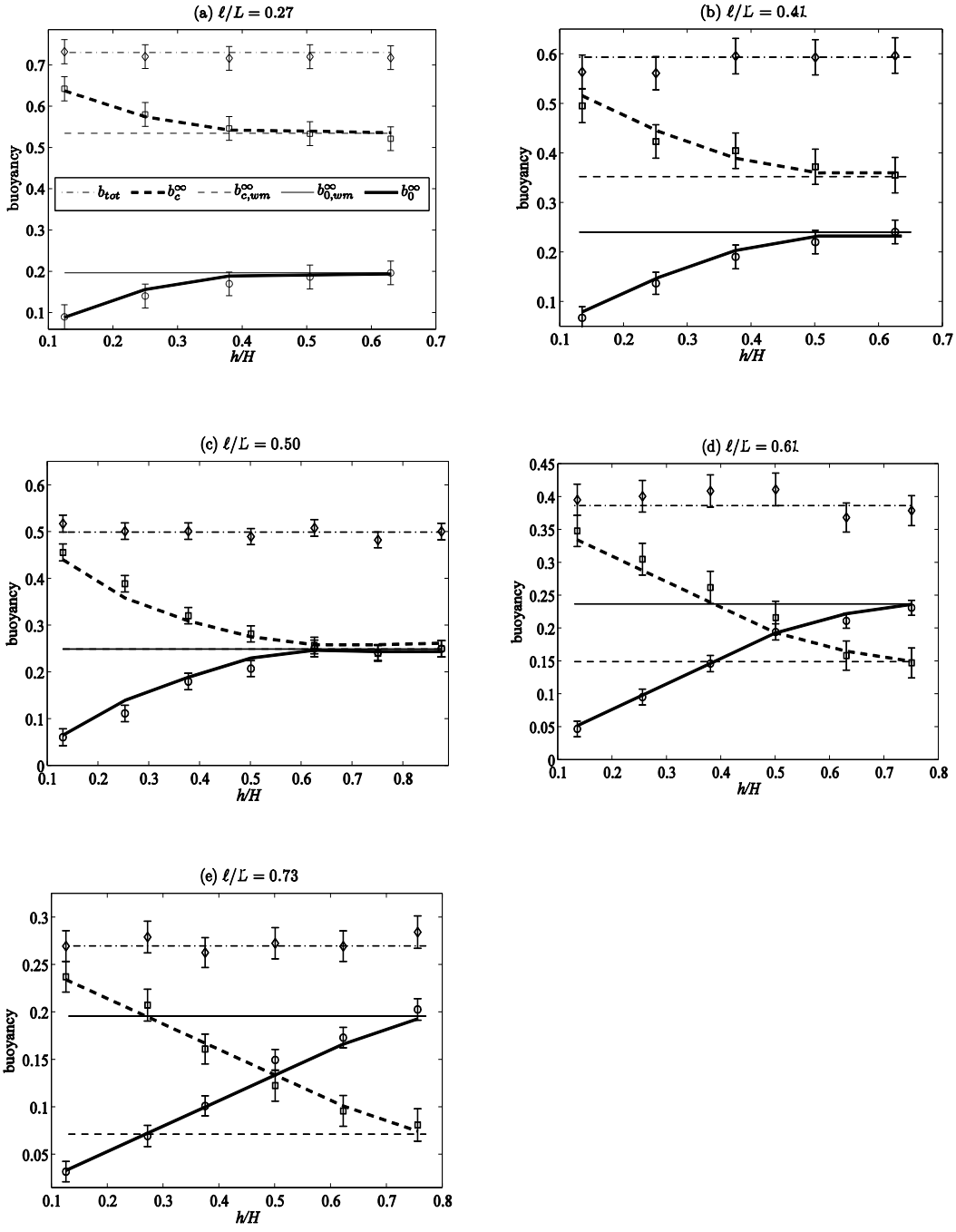

Figure 3-12. Comparison of the terminal buoyancy profiles between experiment (circles, squares, and diamonds for, respectively, $b_{0,exp}^{\infty}$, $b_{c,exp}^{\infty}$, and $b_{tot,exp}^{\infty}$), the stratified model of Section 3.2.2 (of thick lines) and the well-mixed model of Section 3.2.5 (of thin lines).

Clearly, however, superlative agreement between theory and measurement is not observed everywhere: considering the assumptions outlined in Section 3.2.1, we may expect a level of discrepancy between observation and prediction. For fixed h/H, generally better agreement is observed for larger ℓ/L (see e.g. Figures 3-10f and 3-11a). One reason is that ℓ should be much larger than the half-width of the plume, b_p. This cannot be justified when ℓ/L is too small. Moreover, for small h/H better agreement is observed than for large values of h/H. A likely explanation is that the source horizontal momentum flux is ignored in Section 3.2.2. For a doorway with a height comparable to that of the building zone, the flow is less like a vertically rising plume and more like a buoyant gravity current.

Figure 3-12 shows the experimental and theoretical terminal buoyancy as predicted by both the stratified and well-mixed models. As regards the former a promising agreement is observed for a wide range of geometric parameters. Consistent with model predictions in Section 3.2.4, experimental values of b_0^∞ and b_c^∞ increase and decrease with h/H, respectively. For all but the largest of ℓ/L, there is a saturation behavior for large h leading to a plateauing of the thick curves and the associated data points. When ℓ/L=0.50, for instance, an increase of h/H from 0.60 to 0.80, yields a buoyancy variation of less than 1%. Nonetheless, the terminal stratification profile is notably different between h/H =0.6 and 0.8. The impact on occupant comfort is discussed in Section 3.4.2.

As shown in Figure 3-12 and explained in Appendix 3-A, for small h/H, the terminal buoyancy predicted by the well-mixed model for the dense (light) zone significantly over- (under-) predicts measurement. So whereas for large h/H, a well-mixed model may serve as a reasonable approximation, its predictions are generally erroneous for small h/H, especially for large ℓ/L. When ℓ/L=0.50, for instance, the relative difference between b_0^∞ of the stratified model and that of the well-mixed model is 279% for h/H=0.13 but less than 1% for h/H=0.63. Conversely, when ℓ/L is increased to 0.73, the differences are 486% and 18%, respectively, for the same values of h/H. Moreover, in Appendix 3-A we analytically compare b_0^∞ and b_c^∞ for various ℓ/L and h/H and different regimes.

There, we demonstrate that: in the $R > 0$ regime for h/H <0.50 and h/H>0.50 we have, respectively, $b_0^\infty < b_c^\infty$ and $b_0^\infty > b_c^\infty$. Conversely, in the $R < 0$ regime and even for h/H >0.50 we always have $b_0^\infty < b_c^\infty$.

This result is supported by Figure 3-12 and demonstrates that our filling-box model can not only anticipate the values of the terminal buoyancies but also provides guidance regarding the trend of the buoyancy transferred between the adjacent zones. In Figures 3-12d, e we have $b_0^\infty > b_c^\infty$ for h/H >0.50 because $R > 0$ while in panels a, b, c we always have $b_0^\infty < b_c^\infty$, even for h/H >0.50 because $R < 0$.

As a further assessment of our model, if we had changed the position of the plume source in assumption 4 of Section 3.2.1, we would have seen a divergence of the measured and predicted results, e.g. in terms of terminal buoyancies shown in Figure 3-12, particularly for large h/H, a deviation that becomes more severe for larger ℓ/L such a deviation is more pronounced.

3.4.2 Applications to attached solarium design

A major application of this study is to the design of attached solaria. It should be noted that the heat accumulates at solarium in the course of the day. At this point we are interested in how heat is distributed to the adjacent zone. But how the heat continues to be added to solarium is not considered here. Depending on the geometric parameters, different regimes of exchange flow are expected which, dictates the terminal temperature profile in each zone and the rate of convective heat transfer. Here, we briefly examine four case studies.

As a first design consideration, we assume that h =2m. Two scenarios are considered; H =6.67m with a plan area of 18m×18m and H =2.86m with a plan area of 5m×5m. Respectively, these mimic a theater and a regular office/residential zone. We assume that ℓ/L =0.70 and 0.85 and ℓ/L =0.50 and 0.70, respectively, for the former and latter geometries. An initial temperature difference of 8ºC is assumed between the building zone and the attached solarium, the temperature of the former being 17ºC (air properties are calculated at 17ºC).

Table 3-2. Comparison of select design parameters; a. Percent relative temperature difference between the celling and floor (building zone), b. Percent relative increase of the terminal average temperature in the occupied portion (building zone).

h/H	ℓ/L	t_3/t_2	$\frac{\Delta T_{FC}}{\Delta T_0}(\%)$[a]	$h+RH$(m)	$\frac{\Delta T_{ave}}{\Delta T_0}(\%)$[b]	Heat transfer (kJ/m^3)
0.30	0.70	-	42.9	2.63	0.0	0.88
	0.85	-	36.6	4.29	0.0	0.44
0.70	0.30	0.18	100.0	0.77	59.4	2.09
	0.50	0.42	99.9	1.37	28.8	2.44

Table 3-2 summarizes the results for the cases described above. Previously it was shown that the temperature stratification in the dense zone may become appreciable. Therefore, the temperature at the floor may be significantly less than at the ceiling. Table 3-2 shows that for h/H =0.70 such temperature differences may be as large as the initial temperature difference between the adjacent zones. Conversely, when h/H =0.30 and ℓ/L =0.70 the temperature variation over H is less than half of this initial difference.

A person may feel thermally neutral as a whole but still uncomfortable if one or more parts of his or her body are too warm or too cold [33]. Designs associated with minimizing $h+RH$, with R measured from the top of the doorway, are generally favored if the goal is to achieve a temperature profile wherein building occupants do not experience an extreme variation of temperature. Table 3-2 shows that for h/H =0.70 and ℓ/L =0.30 the terminal position of the first front is 0.77m. In practice, due to mixing associated with the movement of building occupants, the stratification is likely to be gradually eroded in time, which in turn, brings the first front closer to the floor. Conversely, for h/H =0.30 and ℓ/L =0.85, no stratification is observed below 4.29m. From the point of view of thermal energy utilization, this height far larger than acceptable.

Also examined in Table 3-2, is the relative change of the average temperature of the air in the occupied portion of the building zone -- the spatial

averaging is confined to the lower 2m of the building zone. In the $R > 0$ regime, this average temperature is unaltered. On the other hand, for h/H =0.70 and ℓ/L =0.30 where $R < 0$, a 59.4% relative increase is realized, i.e. the temperature is projected to increase from 17ºC to 21.8ºC.

In addition to the vertical temperature distribution, the total amount of heat transferred between the solarium and the building zone is, of course, another important parameter. Table 3-2 shows the amount of heat transferred in the long time limit normalized by the building zone volume. Thus according to our model predictions and with reference to Figures 3-3 and 3-12, the following general rule of thumb may be applied: for $h/H \geq \ell/L$ +0.1 diminishing returns are expected.

Considering the above discussion, our model results suggest that the application of attached solaria is particularly favored for a regular office or room where the size of attached solarium can be comparatively large. However, even in case of a theatre with small h/H, the amount of heat exchange may still be significant so that the attached solarium can act as an effective heat source to reduce the energy consumption.

3.5 Conclusions

The hydraulics of the exchange flow between two adjacent building zones, first developed by Nabi and Flynn [9], is extended to cover a significantly broader range of geometric parameters, focusing especially on the common doorway height, h, and relative length of one zone to the other. In particular, it is shown that two distinct regimes may be identified depending on the terminal elevation of the first front: an $R > 0$ regime where this terminal elevation lies above h, and an $R < 0$ regime for which the first front is advected below this point. For the $R < 0$ regime, there is a competition between the speed of descent of the first front and the horizontal speed of the internal bore. Consequently, two sub-scenarios are admitted: $t_3/t_2 > 1$, for which the internal bore reaches the doorway before the first front, and t_3/t_2 <1, in which the opposite occurs. When $t_3/t_2 > 1$ the exchange flow characteristics are more like the $R > 0$ regime while significant differences arise when $t_3/t_2 < 1$. Also for the $R < 0$ regime a non-trivial

stratification evolves in the light zone, which alters the reduced gravity and nature of the exchange flow. The results are compared with similitude experimental data in Section 3.4. Many predictions, such as a stark change in the stratification below the top of the doorway, the near equality of $\Delta_{a,0}^{\infty}$ and $\Delta_{a,c}^{\infty}$ for large values of h/H, the presence of nontrivial stratification in the intermediate layer of the light zone , etc. are all reproduced experimentally.

In Figure 3-12 we explore, the effect of h/H and ℓ/L on the (terminal) depth-integrated buoyancy in both zones. A saturation behavior arises for large h/H whereas both b_0^{∞} and b_c^{∞} vary roughly linearly for small h/H especially for large ℓ/L.

Stratification profiles and the total buoyancy exchanged between the two zones are also predicted using a well-mixed model. When h is large, both well-mixed and stratified models predict comparable terminal buoyancies; for smaller h there is up to an order of magnitude difference. In the context of real buildings, where exchange flows and filling-box processes are combined with supplemental mixing e.g. due to non-stationary occupants, the observed b_0^{∞} and b_c^{∞} should lie between the predictions of our stratified and well-mixed models. For large h/H, the stratified and well-mixed model predict similar results, however, this is not the case for small h/H in which case the properties of the observed state should depend sensitively on the details of the aforementioned mixing.

Although our results are derived for rectangular geometries, they can be extended to other geometries as well [20]. More realistic cases may include doorways having a different geometry, especially one where the doorway width is less than that of the building zone. Moreover, the choice of allowing the layers to be redistributed when they coincide with the top of the doorway versus at some later time e.g. when they reach the interface has been carefully examined. Firstly, we should note that such a choice is entirely academic insofar as the terminal state is concerned. In other words, $\Delta_{a,0}^{\infty}$, $\Delta_{a,c}^{\infty}$, $b_{a,0}^{\infty}$ and $b_{a,c}^{\infty}$, which represent arguably the most important independent variables predicted by our model, are the same whether one redistributes when the layers reach (i) the top of the doorway, (ii) the interface, or, (iii) some other point below the top of the doorway. Regarding the

transient approach towards the terminal state we find that such differences arise only when $t_3 < t_2$ and then only during the time interval $t_3 < t < t_2$.

Appendix 3-A

Here, we derive analytical expressions to describe the terminal buoyancy in either building zone. That of the light zone typically consists of three layers (Figure 3-7a). If I represents the buoyancy of the intermediate layer, we may define

$$I = \lim_{t\to\infty} \frac{1}{g_0' HL} \int_{\ell}^{L} \int_{z_{ff}}^{h} (-\Delta_{a,c})\, dzdx \tag{3-A-1}$$

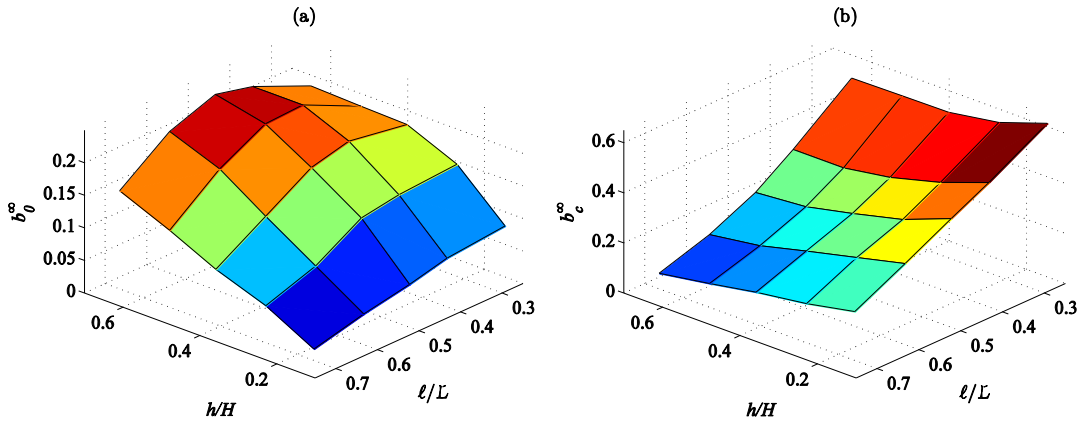

Figure 3-A-1 [Color online] (a) Dense-zone, b_0^∞, and (b) light-zone, b_c^∞, terminal buoyancy versus h/H and ℓ/L.

Therefore the terminal buoyancy of the light zone can be written as

$$b_c^\infty = \left(1 - \frac{\ell}{L}\right)\left(1 - \frac{h}{H}\right) + I \tag{3-A-2}$$

The total buoyancy being conserved, the terminal buoyancy of the dense zone is

$$b_0^\infty = \left(1 - \frac{\ell}{L}\right)\left(\frac{h}{H}\right) - I \tag{3-A-3}$$

The influence of ℓ/L on b_0^∞ and b_c^∞ is investigated in Figure A-1; b_c^∞ decreases with ℓ/L whereas b_0^∞ exhibits a local maximum when ℓ/L =0.50.

In quantitatively comparing b_0^∞ and b_c^∞, note that when $R > 0$, I =0, and therefore

$$\frac{b_0^\infty}{b_C^\infty} = \frac{1}{1-\frac{h}{H}} - 1 \tag{3-A-4}$$

From (3-A-4) it can be deduced that there is an equipartion of buoyancy i.e. $b_0^\infty = b_C^\infty$ when h/H =0.50. However, this result only holds true only when ℓ/L >0.59 (Figure 3-3). More generally R <0 and b_0^∞/b_c^∞ is proportional to I: for small t_3/t_2, I and b_0^∞/b_c^∞ are relatively large (Figure 3-12d,e).

The terminal buoyancy given by the well-mixed model, $b_{wm,0}^\infty$ and $b_{wm,c}^\infty$ can be found from (3-24), i.e.

$$b_{wm,0}^\infty = \left(1-\frac{\ell}{L}\right)\left(\frac{\ell}{L}\right) \tag{3-A-5-a}$$

$$b_{wm,c}^\infty = \left(1-\frac{\ell}{L}\right)^2 \tag{3-A-5-b}$$

When $R > 0$, the ratio of the terminal buoyancy predicted by the stratified model to that of the well-mixed model is

$$\frac{b_0^\infty}{b_{wm,0}^\infty} = \frac{\left(\frac{h}{H}\right)}{\left(\frac{\ell}{L}\right)} \text{ [dense zone]} \tag{3-A-6-a}$$

$$\frac{b_c^\infty}{b_{wm,c}^\infty} = \frac{\left(1-\frac{h}{H}\right)}{\left(1-\frac{\ell}{L}\right)} \text{ [light zone]} \tag{3-A-6-b}$$

When $R > 0$, $\ell/L > h/H$ (Figure 3-3). It follows that $b_{wm,0}^\infty > b_0^\infty$ and $b_c^\infty > b_{wm,c}^\infty$. The terminal buoyancy predicted by the well-mixed model is not a function of h/H, but this is inconsistent with measured data according to Figure 3-12.

When $R < 0$, (3-A-6-a) and (3-A-6-b) must be modified to include the parameter I defined by . The analysis now becomes more complicated, however it can still be shown that $b_0^\infty \to b_{wm,0}^\infty$ and $b_c^\infty \to b_{wm,c}^\infty$ for large h/H. When h/H is small or moderate, there is an imbalance between the pairs of terminal buoyancies in either zone (Figure 3-12).

References

[1] U.S. Department of Energy. http://apps1.eere.energy.gov/ buildings/ publications/ pdfs/ corporate/ bt_stateindustry.pdf.

[2] ENERGY STAR®. http://www.energystar.gov/ia/business/challenge/ learn_more/ FastFacts.pdf.

[3] Linden PF. The fluid mechanics of natural ventilation. Annu Rev Fluid Mech 1999;31:201-238, 1999.

[4] Parker DS. Very low energy homes in the United States: Perspectives on performance from measured data. Energ Buildings 2009;41:512–520.

[5] Parameshwarana R, Kalaiselvamb S, Harikrishnanb S, Elayaperumala A. Sustainable thermal energy storage technologies for buildings: A review. Renew Sust Energ Rev 2012;16: 2394–2433.

[6] Shearer D, Porteous CDA. Winter performance of 2-storey solar buffer spaces in Glasgow demonstration houses. EuroSun 2012.

[7] Heim D. Isothermal storage of solar energy in building construction. Renewable Energy 2010;35:788–96.

[8] Nabi S, Flynn MR. Architectural Exchange Flows and Their Influence on Interior Temperature Stratification and Building Ventilation, Clima 2013 : 11th REHVA World Congress and 8th International Conference on IAQVEC, Prague, Czech Republic, June 2013.

[9] Nabi S, Flynn MR. The hydraulics of exchange flow between adjacent confined building zones. Build Environ 2013;59:76-90.

[10] Sandbach SD, Lane-Serff GF. Transient buoyancy-driven ventilation: Part 2. Modelling heat transfer. Building and Environment 2011;46(8):1589e99.

[11] Chen Q. Ventilation performance prediction for buildings: A method overview and recent applications. Build Environ 2009;44:848-858.

[12] Sandbach SD, Lane-Serff GF. Transient buoyancy-driven ventilation: Part 1. Modelling advection. Build Environ 2011;46:1578-1588.

[13] Mingotti N, Chenvidyakarn T, Woods AW. The fluid mechanics of the natural ventilation of a narrow-cavity double-skin facade. Build Environ 2011;46:807-823.

[14] Kaye NB, Flynn MR, Cook MJ, Ji Y. The role of diffusion on the interface thickness in a ventilated filling box. J Fluid Mech 2010;652:195-205.

[15] Merci B, Maele K. Numerical simulations of full-scale enclosure fires in a small compartment with natural roof ventilation. Fire Safety J 2008;43:495-511.

[16] Linden PF, Lane-serff GF, Smeed DA. Emptying filling boxes: the fluid mechanics of natural ventilation. J Fluid Mech 1990;212:309-335.

[17] Caulfield CP, Woods W. The mixing in a room by localized finite-mass-flux source of buoyancy. J Fluid Mech 2002;471:33-50.

[18] Kuesters AS, Woods W. The formation and evolution of stratification during transient mixing ventilation. J Fluid Mech 2010;670:66-84.

[19] Bolster D, Caulfield CP. Transients in natural ventilation-A time-periodically- varying source. Building Serv Eng Res Technol 2008;29,2:119-135.

[20] Baines WD, Turner JS. Turbulent buoyant convection from a source in a confined region. J Fluid Mech 1969;37:51-80.

[21] Morton BR, Taylor GI, Turner JS. Turbulent gravitational convection from maintained and instantaneous sources. J Fluid Mech 1956;234:1-23.

[22] Dalziel SB, Lane-serff G. The hydraulics of doorway exchange. Build Environ 1991;26:2:121-35.

[23] Benjamin TB. Gravity currents and related phenomena. J Fluid Mech 1968;31:209-248.

[24] Klemp JB, Rotunno R, Skamarock WC. On the propagation of internal bores. J Fluid Mech 1997;331:81-106.

[25] Rottman JW, Simpson JE. Gravity currents produced by instantaneous releases of a heavy fluid in a rectangular channel. J Fluid Mech 1983;135:95-110.

[26] Rouse H, Yih C, Humphreys H. Gravitational convection from a boundary source. Tellus 1952;4:200-210.

[27] Dalziel SB. Two-layer hydraulics: a functional approach. J Fluid Mech 1991;223:135-163.

[28] Holford JM, Hunt GR. The dependence of the discharge coefficient on density contrast - experimental measurements. 14th Australian Fluid Mechanics Conference, Adelaide University, Adelaide, Australia, 2001.

[29] Wilson DJ, Kiel DE. Gravity driven counter flow through an open door in a sealed room. Build Environ 1990;25:379-388.

[30] Germeles AE. Forced plumes and mixing of liquids in tanks. J Fluid Mech 1975;71:601-623.

[31] Tatcher TL, Wilson DJ, Wood EE, Craig MJ, Sextro RG. Pollutant dispersion in a large indoor space: part 1-scaled experiments using a water-filled model with occupants and furniture. Indoor Air 2004;14:258e71.

[32] Taylor JR. An introduction to error analysis: The study of uncertainties in physical measurements. 2nd ed. University Science Books; 1997.

[33] ANSI/ASHRAE Standard 55-2010, Thermal Environmental Conditions for Human Occupancy.

Chapter 4

Buoyancy-driven exchange flow between two adjacent building zones connected with top and bottom vents

4.1 Introduction

Buoyancy-driven exchange flow is a common phenomenon in many different situations, such as environmental (e.g. river plumes), architectural (e.g. natural ventilation) and industrial (e.g. fire protection) settings [1-6]. While much attention has been given to exchange flow between (semi-)infinite or infinite regions and finite regions, less is known regarding the exchange flow between inter-connected finite regions [7-11]. This lack of knowledge limits the deployment of natural ventilation, which is a potentially viable ventilation strategy in many geographical regions. Expanding the reach of natural ventilation

is desirable because of the energy savings associated with a reduced reliance on traditional HVAC equipment. Hence, a better understanding of natural ventilation, with a potential to balance all or part of the energy consumed by mechanical devices, is an imperative task for engineers and architects.

As we mentioned in Chapters 2 and 3, buoyancy-driven exchange flows between inter-connected confined zones highly depend on the position of the interior openings. We examined the exchange flow between two zones of slightly different densities separated by a single common doorway which was located at the bottom of each zone. In order to gain a more complete understanding of architectural exchange flows, we now extend our investigation to cases where the bottom openings or vents are matched by an equal or unequal number of vents adjacent to the ceiling, which we will hereafter refer to as the top vents. The number of bottom and top vents we denote by N_b and N_t, respectively. It should be noted that $N_b/N_t = 0$ or ∞ results in the exchange flow that has been examined before in Chapters 2 and 3. There are non-trivial differences, however, between the two scenarios of non-zero N_b and N_t. Such differences will be outlined below. The volumetric exchange rate is Q_e and, in order to satisfy volume conservation, must be equal in magnitude as regards the flow through the bottom and top vents. The total chamber depth is H, the diameter of each vent is D and, consistent with our previous notation, the length of the dense zone is ℓ and the total length of both building zones is L. h, shown in Figure 4-1, is the vertical distance between the bottom of the bottom vent and the floor and is a fixed value. We assume a symmetrical building so that h is also the distance between the top of the top vent and ceiling.

In the mixing ventilation scenario, by opening the interior doorway, a two-layer exchange flow is established, which results in two qualitatively different flows: a buoyant plume that rises through the dense zone and a horizontal gravity current that propagates through the light zone. Over time, a stratified ambient develops in the dense zone, and depending on the geometrical parameters discussed in Chapters 2 and 3 the light zone will include two distinct layers with a possible intermediate stratified layer. Conversely in the displacement ventilation

flow that is the topic of the present chapter, by opening the top and bottom vents simultaneously unidirectional flow of opposite sign is observed through the bottom and the top vents. This in turn, evolves into horizontal gravity currents that run along the floor and ceiling of the space. As indicated by Figure 4-1b, the gravity currents have respective speeds $u_{1,b}$ and $u_{1,t}$. Therefore, unlike in the mixing ventilation scenario, there is no ascending plume (provided N_b and N_t are comparable), and, by extension, no filling-box process. Instead, we anticipate a two-layer stratification in each zone with a sharp density jump from one layer to the other. Upon reflection from end walls, floor and ceiling gravity currents yield internal bores with respective speeds $u_{2,b}$ and $u_{2,t}$ (Figure 4-1c). In the present study, we refer to the gravity currents and resulting internal bores as horizontal currents. The influence of these horizontal currents on Q_e, will be outlined in Section 4.2.

As with mixing ventilation, Q_e decreases once the internal bores reach the doorway. However, unlike in mixing ventilation, Q_e now tends to zero in a finite time t_E, rather than in an infinite time. For times larger than $t_{2,j}$ (with $j = b$ or t indicating the bottom or top flow, respectively) a horizontal interface develops in each zone; in the light zone a layer with depth h_b moves upward and, meanwhile, a layer with depth h_t travels downward in the dense zone (Figure 4-1d). In this study the interface refers to the density surface that divides the light zone fluid above from the dense or stratified fluid beneath. Initially, the variation of the interface positions with time is nearly uniform; though, later on the respective layers grow at a slower pace. For $t > t_E$, the interface elevations do not change as a function of time. We investigate the influence of pertinent geometrical parameters, e.g. the number of open vents, N_b and N_t, the relative size of the two zones, ℓ and L, the building height, H, and the initial density difference $\rho_0 - \rho_c$ on Q_e, t_E, h_b and h_t.

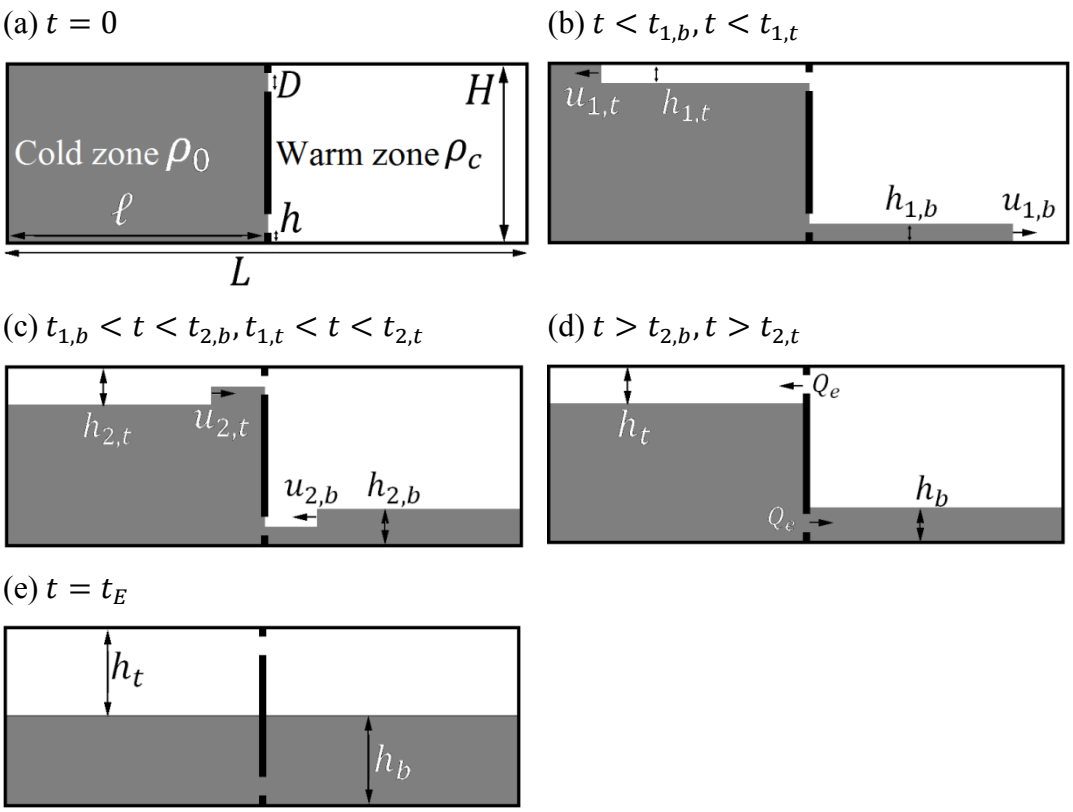

Figure 4-1. Schematic of the displacement exchange flow in the absence of source at (a) $t = 0$, the instant when buoyancy-driven motion begins, (b) $t < t_{1,b}$ and $t_{2,b}$, before the dense or light gravity currents reach the end wall, (c) $t < t_{2,b}$ and $t_{2,t}$, after reflection of the dense and light gravity currents as internal bores, (d) $t > t_{2,b}$ and $t_{2,t}$, after the dense and light bores reach the horizontal position of the vents, $x = \ell$ and (e) $t = t_E$ when the exchange flow is terminated.

Due to numerous differences between the two modes of exchange flow described above, displacement ventilation merits its own investigation, all the more so because, as we shall see, Q_e is now typically larger than for the cases examined in Chapters 2 and 3. Therefore, if the purpose is to redistribute buoyancy from an attached solarium as quickly as possible, the architectural design shown in Figure 2-1 is inferior to that of Figure 4-1. On the other hand, the scenario described by Figure 4-1 is relatively straightforward to analyze, given that it possesses a well-defined end state. Consequently it is of interest to extend

the analysis in an architecturally meaningful way. We do so by including an isolated source of buoyancy in the light zone.

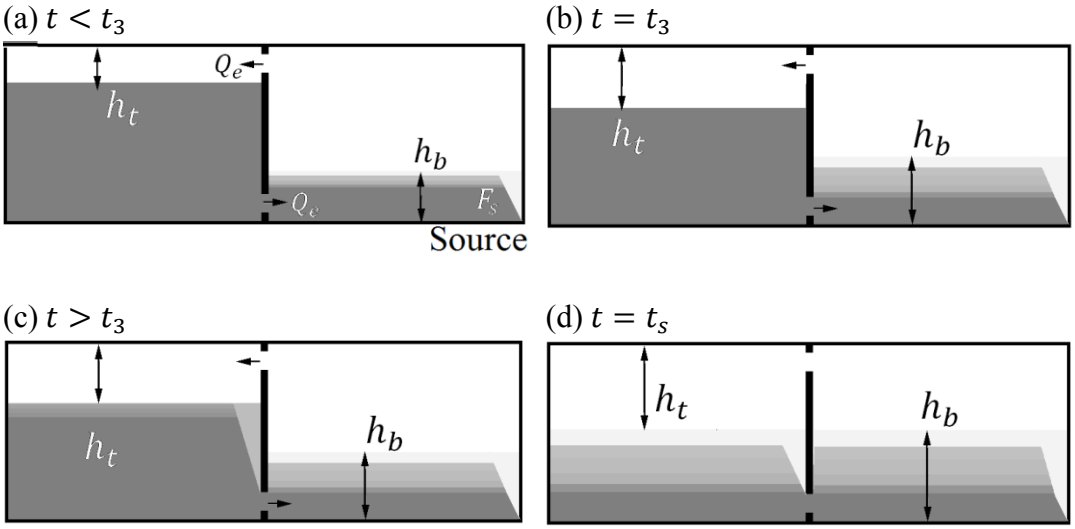

Figure 4-2. Schematic of the displacement exchange flow with a source at (a) $t < t_3$ when the stratification due to the source lies strictly above the top of the bottom vent in the light zone, (b) $t = t_3$, (c) $t_3 < t < t_s$ when a plume rises through the lower layer of the dense zone (d) $t = t_s$ when the source is turned off. Here t_3 is the time required for the first front to reach to the top of the bottom vent and t_s is the time during which the source is switched on.

The geometry of the source may fall between a point or line source of buoyancy [6] to fully distributed heat source [12]. In case of the former a stratified building zone is expected and in case of the latter the room air remains well mixed. Transition between the two cases occurs when the area of the source exceeds approximately 15% of the room area [13]. The point or line and fully distributed limits for a source with given buoyancy flux and for a given time provide helpful upper and lower bounds [13]. Here we consider a line source of buoyancy. The source origin is located at the base of the end-wall in the light zone, has a buoyancy flux F_s and provides a continuous source of buoyancy in the form of an ascending plume as indicated schematically in Figure 4-2. Over the time, t_s, that it is active or "switched on", the source thereby continually increases the thermal energy within the building envelope in addition to the energy that is transferred as a result of the exchange flow depicted in Figure 4-1. t_s scales the

time during which the building zone is subjected to solar gains and may be non-trivial over the significant fraction of the day. Thus, the source introduces additional dynamics, which are superimposed on top of those associated with a simple two-zone exchange flow. More specifically a non-trivial stratification in the light zone develops (Figure 4-2). For sufficiently large F_s and t_s, the first front, defined as the horizontal line dividing the stratified ambient above from the unmodified dense ambient below, may reach the top of the bottom vent at $t = t_3$, say. Thereafter, buoyant fluid will spill into the dense zone yielding a non-trivial vertical stratification there too (Figure 4-2c). In either case, the filling box model of Chapters 2 and 3 can be adapted to describe the zonal evolution of the stratification.

Combining the displacement and exchange flows, there are thus a number of important time scales to be considered i.e. t_2, t_3, t_s, t_E. We investigate the influence of each of these on various parameters related to thermal comfort and heat transfer, e.g., buoyancy, interface height and exchange flow rate.

The mathematical model is developed in Section 4.2. A discussion of theoretical predictions is also included in therein. In Section 4.3, the experimental setup and procedure is explained. In Section 4.4, we compare theoretical and experimental results to understand the nature of displacement flow and assess the validity of the model equations from Section 4.2. Conclusions and future considerations are drawn in Section 4.5.

4.2 Theory

In this section we develop an analytical model for the displacement ventilation between two confined zones that are connected with top and bottom vents. We seek a theoretical framework to describe the evolution of density and buoyancy in each zone with respect to time and space. Consistent with the methodology of Chapters 2 and 3, we derive a composite model through a non-trivial combination of various constituent components such as two counterpart exchange flows, gravity currents, internal bores and stratification due to the plume. As we will see later, the dynamics of each zone are highly coupled to one another.

Only vertical stratification is considered in this study. It is assumed that there are no fabric heat losses or gains through the ceiling or floor of the dense zone and that the building is well insulated. In fact, the only interaction of the building with the exterior is through the presence of the source of buoyancy in the light zone. The system is assumed to be incompressible and Boussinesq and the pressure distribution hydrostatic. The plume is assumed to be switched on at $t = t_{2,b}$, not t =0, the instant when the bottom and top vents are simultaneously opened. Such an assumption has only a minor impact on the dynamics of the displacement exchange flow because during $0 \leq t \leq t_{2,b}$, the buoyancy added to the system from the source is insignificant compared to that gained (lost) in the light (dense) zone by the exchange flow. Moreover, any entrainment or detrainment into or out of horizontal currents is ignored. Finally, the two fluids of different densities above and below the interface are miscible and the surface tension is zero. For a detailed description of assumptions related to the interaction of the plume and ambient, the reader is referred to Sections 2.2 and 2.3.

4.2.1 Ventilation flow with no source of buoyancy

Here we develop the theory for ventilation by a displacement exchange flow in the absence of a source of buoyancy, i.e. F_s=0. For purposes of analytical efficacy the problem is divided into three complementary parts: i) two counterpart exchange flows, both of which are unidirectional and which arise due a difference of hydrostatic pressure between the adjacent building zones, ii) horizontal currents comprising the bottom and top gravity currents and associated internal bores and iii) the vertical motion of the interface in each zone.

Four scenarios in terms of the values for h_b and h_t at $t = t_2$ are possible depending on the bottom and top opening effective areas and relative size of the two zones. Here we only focus on the scenario where both $\frac{h_{2,b}}{(h+D)} > 1$ and $\frac{h_{2,t}}{(h+D)} > 1$, which is the most architecturally relevant among other scenarios discussed in appendix 4-A.

4.2.1.1 Exchange flow rate Q_e and interface height

By simultaneously opening the top and bottom vents, two oppositely-directed exchange flows are established. By volume balance these two volume fluxes must be equal in magnitude. Hence, the respective conservation of volume equations for flow through the bottom and top vents read as

$$Q_e = u_b a_b = u_t a_t \tag{4-1}$$

Here u_b (u_t) is the velocity thorough the bottom (top) vent(s) whose respective total area is a_b (a_t). We assume a circular vent geometry so that a_b and a_t are given by $N_b \frac{\pi}{4} D^2$ and $N_t \frac{\pi}{4} D^2$, respectively.

To determine Q_e, some estimate of the pressure difference across the upper vents is needed for which purpose we suppose that the pressure along the ceiling of the dense and light zone is, respectively, p_A and p_B, where A and B are defined at immediate left and right of the upper vent. A straightforward application of Bernoulli's equation shows that

$$Q_e = \sqrt{2\frac{\Delta p_b}{\rho_0}}\, a_b = \sqrt{2\frac{\Delta p_t}{\rho_0}}\, a_t \tag{4-2}$$

in which the pressure difference Δp_t is given by $\Delta p_t = p_B - p_A$. Also, by hydrostatic balance,

$$\Delta p_b = (\rho_0 - \rho_c)(H - h_b - h_t)g - \Delta p_t \tag{4-3}$$

Substituting (4-2) and (4-3) into (4-1a), we can solve for the velocities u_b and u_t the former of which is given by

$$u_b = \sqrt{\frac{g'(H - h_b - h_t)}{\frac{1}{2}\left(1 + \left(\frac{a_b}{a_t}\right)^2\right)}} \tag{4-4}$$

Then by applying (4-4) into (4-1), we find that

$$Q_e = A^* \sqrt{g'(H - h_b - h_t)} \tag{4-5}$$

where A^* is the effective vent area and is defined by

$$A^* = \frac{a_b a_t}{\sqrt{\frac{1}{2}(a_b^2 + a_t^2)}} \tag{4-6}$$

This result neglects any viscous dissipation via entrance and exit effects and also ignores interfacial mixing. Whereas the latter does not influence the exchange flow rate the former does and we incorporate these losses by introducing discharge coefficient. In this way (4-6), consistent with Kaye and Hunt [14], is written as

$$A^* = \frac{a_b a_t}{\sqrt{\frac{1}{2}\left(\left(\frac{a_b}{c_b}\right)^2 + \left(\frac{a_t}{c_t}\right)^2\right)}} \tag{4-7}$$

where c_b and c_t are, respectively, the discharge coefficients associated with the bottom and top vents. Consistent with [14], we assume $c_b = c_t$ =0.6.

Equation (4-7) shows that A^* is a strong function of $\min(a_b, a_t)$, which, for the uniform vent diameter case considered here, signifies that it is the smaller of N_b and N_t that largely determines the magnitude of the displacement exchange flow. More generally, equation (4-5) is similar to (2.4) of Linden et al. [6], which specifies the exchange flow rate between an interior and exterior. A key difference is that here Q_e depends on two interface heights i.e. h_b and h_t. The time evolution of these can be connected by applying conservation of volume, according to which

$$Q_e = (L - \ell)W\frac{dh_b}{dt} = \ell W\frac{dh_t}{dt} \tag{4-8}$$

Equations (4-5) and (4-8) therefore constitute a coupled pair of ordinary differential equations, whose solution requires the specification of a pair of starting conditions i.e.

$$h_b = h_{2,b} \text{ at } t = t_{2,b} \tag{4-9a}$$

$$h_t = h_{2,t} \text{ at } t = t_{2,t} \tag{4-9b}$$

Note also that conservation of volume gives the relationship between h_b and h_t:

$$h_t = \frac{L - \ell}{\ell} h_b \tag{4-10}$$

We employ (4-9), as starting conditions, to solve (4-8). Upon applying (4-5), integrating and simplifying, it can be shown that

$$\frac{h_b}{H} = \left[1 - \left(\sqrt{\left(1 - \frac{L}{\ell}\frac{h_{2,b}}{H}\right)} - \frac{\left(t - t_{2,b}\right)}{\frac{T_E \ell}{L}}\right)^2\right]\frac{\ell}{L} \tag{4-11}$$

where T_E is given by

$$T_E = \sqrt{\frac{H}{g'}}\left(\frac{2(L-\ell)W}{A^*}\right) \tag{4-12}$$

In physical terms, T_E is similar to the draining time defined by (2.8) of Linden et al. [6]. However, there is a key difference between their approach and ours. They considered the ventilation between an interior and exterior, while we are concerned with the flow between two adjacent building zones, neither one of which exchanges mass with the outside environment. In our case, therefore, T_E does not correspond to the time required to reach steady state. The relevant time-scale is instead t_E, which is defined as

$$\frac{t_E}{T_E} = \frac{L}{\ell}\left(\sqrt{\left(1 - \frac{L}{\ell}\frac{h_{2,b}}{H}\right)} + \frac{t_{2,b}}{\frac{T_E \ell}{L}}\right) \tag{4-13}$$

Note that when $t = t_E$, Q_e, dh_b/dt and dh_t/dt are all zero.

Moreover, using (4-11) it can be shown that $h_b/H = \ell/L$ when $t = t_E$. By increasing ℓ/L or decreasing the effective area, A^*, t_E increases and, therefore, it takes more time for the interfaces to reach their terminal elevations.

4.2.1.2 Theory for horizontal flows

1**- Gravity current formulation**:

We use the Benjamin equation for the front speed, u_1, in terms of the front height, h_1

$$\frac{u_1^2}{g'H} = \frac{h_1(H-h_1)(2H-h_1)}{H^2(H+h_1)} \tag{4-14}$$

along with the equation for mass conservation, which leads to the following expression for the initial volumetric exchange rate

$$Q_e = u_1 h_1 W \tag{4-15}$$

The pair of equations (4-14) and (4-15) is identical to our previous mixing ventilation formulation for bottom gravity currents -see equations (2-12) and (2-14).

2- **Internal bore formulation**:

We use the Klemp et al-type approach

$$\frac{u_2^2}{g'H} = \frac{h_1^2(H-h_1)(2H-h_1-h_2)}{H^2(Hh_1+Hh_2+h_1^2-3h_1h_2)} \tag{4-16}$$

which establishes the connection between the bore speed, u_b, and the bore height, h_b. Equation (4-16) is coupled to a mass conservation equation, here expressed as

$$Q_e = u_2(h_2-h_1)W \tag{4-17}$$

The set of equations (4-16) and (4-17) is identical to our previous mixing ventilation formulation for internal bores -see equations (2-15) and (2-16).

Assuming constant velocity for the horizontal currents, we have

$$t_{2,b} = (L-\ell)\left(\frac{1}{u_{1,b}}+\frac{1}{u_{2,b}}\right) \tag{4-18a}$$

$$t_{2,t} = \ell\left(\frac{1}{u_{1,t}}+\frac{1}{u_{2,t}}\right) \tag{4-18b}$$

where t_2 is the time required for the internal bore to reach the horizontal position of the vent(s). Equations (4-18) show that for ℓ/L <1/2 (>1/2) we have $t_{2,b} > t_{2,t}$ ($t_{2,b} < t_{2,t}$). Obviously, when the two zones are equal in size $t_{2,b} = t_{2,t} \equiv t_2$. Using (4-14) and (4-16) implies that the propagation velocity for both gravity current and internal bore is assumed to be span-wise uniform.

4.2.1.3 Buoyancy

Consistent with the previous chapters we define the non-dimensional total buoyancy as

$$b_{c.v.} = \frac{1}{g'HL}\iint g\frac{\rho_{c.v.}-\rho_0}{\rho_0}\,dzdx \tag{4-19}$$

The control volume is either dense or light zone. As usual, g' denotes the reduced gravity, i.e.

$$g' = g\frac{\rho_0-\rho_c}{\rho_0} \tag{4-20}$$

The total initial buoyancy of the system is

$$b(0) = -\left(1 - \frac{\ell}{L}\right) \tag{4-21}$$

4.2.2 Ventilation flow with a source of buoyancy

In the previous sub-section, we developed a model describing ventilation in the absence of a source of buoyancy. We now extend our analysis to take into account the impact of an isolated source, which is turned on at $t = t_2$ for a time interval $t_s \gg t_2$. The source consists of an ideal line plume distributed uniformly along the width of the light zone with a buoyancy flux of F_s.

The process by which the plume interacts with the light zone ambient fluid through entrainment and boundary discharge, i.e. the lateral flow of discharged plume fluid along the interface, is referred to as the filling-box model [15]. (For a more detailed description of the filling-box process refer to Chapter 2 and 3). By continual discharge of fluid from the source, a nontrivial stratification develops over time as shown schematically in Figure 4-2. We assume the stratification is confined to the region below the interface, i.e. $0 < z < h_b$. Above this region the plume density is larger than the light zone fluid and the buoyancy force is downward. Although the plume momentum flux is larger than 0, which may allow the plume to ascend above the interface, consistent with [16] and also the analysis of Chapters 2 and 3, we ignore such an overshoot.

The vertical expanse of the control volume into which the plume ascends increases with time, i.e. $\frac{dh_b}{dt} > 0$. The plume/ambient interaction therefore depends on the exchange flow rate and interface height, which is in turn influenced by the filling-box process and stratification associated with plume.

Because the bottom vent(s) is/are above the source origin, the advecting first front is able to reach the top of the bottom vent(s) in finite time, say, t_3. In the present circumstance, any layer advected below $z = h + D$ will flow into the dense zone and form N_b separate axisymmetric plume(s), as we illustrate schematically in Figure 4-2. We denote the light and dense zone density below the interface as $\rho_{a,c}$ and $\rho_{a,0}$, respectively; both are functions of time and elevation.

By design, the dynamics of the horizontal currents depend on the initial condition but not the source properties. This is because the plume is not activated until $t = t_2$. As explained before, due to the small fraction of buoyancy added by the source in $0 < t < t_2$ as compared to over the much larger time interval quantified by t_s, we expect very similar results if the plume were instead activated at t =0.

4.2.2.1 Exchange flow rate Q_e and interface height

We now aim to derive a formula for Q_e for the case where $F_s > 0$. By assuming a hydrostatic pressure distribution, we have

$$\Delta p_b = \rho_c g h_t + \int_{h+\frac{D}{2}}^{H-h_t} \rho_{a,o} g dz - \rho_c g (H - h_b) - \int_{h+\frac{D}{2}}^{h_b} \rho_{a,c} g dz - \Delta p_t \tag{4-22}$$

as the pressure difference between two points immediately to the left and right of the bottom vent. $\rho_{a,o}$ and $\rho_{a,c}$ are the dense and light zone ambient density, respectively. Equation (4-4) is now expressed as

$$\frac{u_b^2}{2} = g'(H - h_b - h_t) - \frac{u_t^2}{2} + \int_{h+\frac{D}{2}}^{H-h_t} \frac{\rho_{a,o}}{\rho_0} g dz - \int_{h+\frac{D}{2}}^{h_b} \frac{\rho_{a,c}}{\rho_0} g dz \tag{4-23}$$

which, upon applying conservation of volume, reduces to

$$u_b = \sqrt{\frac{g'(H - h_b - h_t) + \int_{h+\frac{D}{2}}^{H-h_t} \Delta_{a,o} dz - \int_{h+\frac{D}{2}}^{h_b} \Delta_{a,c} dz}{\frac{1}{2}\left(1 + \left(\frac{a_b}{a_t}\right)^2\right)}} \tag{4-24}$$

Here $\Delta_{a,o}$ and $\Delta_{a,c}$ are the characteristic reduced gravities of the dense and light zones, respectively, and are defined as

$$\Delta_{a,0} = g \frac{\rho_{a,0} - \rho_0}{\rho_0} \leq 0 \tag{4-25a}$$

$$\Delta_{a,c} = g \frac{\rho_{a,c} - \rho_0}{\rho_0} \leq 0 \tag{4-25b}$$

Now, the exchange flow rate using (4-1) and (4-24) is given by

$$Q_e = A^* \sqrt{g'(H - h_b - h_t) + \int_{h+\frac{D}{2}}^{H-h_t} \Delta_{a,o} dz - \int_{h+\frac{D}{2}}^{h_b} \Delta_{a,c} dz} \tag{4-26}$$

where A^* is defined by (4-7).

When the dense and light zone stratification is due to the filling-box process, it is impossible to solve (4-8) and (4-9) along with (4-26) analytically. Rather, a numerical solution is sought. Complicating matters is the fact, discussed in further detail below, that h_b and h_t depend on the interaction of the vertical plume(s) and the surrounding ambient.

4.2.2.2 Buoyancy

Due to the source, the total buoyancy is now not conserved. To wit

$$b = -\left(1 - \frac{\ell}{L}\right) + b_s \tag{4-27}$$

where the first term on the right hand side of (4-27) is the initial buoyancy and b_s, the non-dimensional buoyancy added to the system by the source at any instant, is characterized by the parameter

$$b_s = -\frac{F_s t}{g' W H L} \tag{4-28}$$

The dense and light zone buoyancy can be written as

$$b_0 = \left(\int_{h+\frac{D}{2}}^{H-h_t} \frac{\Delta_{a,o}}{g'} \frac{dz}{H} - \left(\frac{h_t}{H}\right)\right)\left(\frac{\ell}{L}\right) \tag{4-29a}$$

$$b_c = \left(\int_{h+\frac{D}{2}}^{h_b} \frac{\Delta_{a,c}}{g'} \frac{dz}{H} - \left(1 - \frac{h_b}{H}\right)\right)\left(1 - \frac{\ell}{L}\right) \tag{4-29b}$$

respectively. Applying (4-10), it can therefore be shown that

$$b_s = \left[\int_{h+\frac{D}{2}}^{H-h_t} \frac{\Delta_{a,o}}{g'} \frac{dz}{H}\right]\left(\frac{\ell}{L}\right) + \left[\int_{h+\frac{D}{2}}^{h_b} \frac{\Delta_{a,c}}{g'} \frac{dz}{H}\right]\left(1 - \frac{\ell}{L}\right) \tag{4-30}$$

and, by extension,

$$Q_e = A^* \sqrt{g'(H - h_b - h_t) + \frac{g'HL}{\ell} b_s - \frac{L}{\ell} \int_{h+\frac{D}{2}}^{h_b} \Delta_{a,c} dz} \tag{4-31}$$

Equation (4-31) expresses the exchange flow rate as a function of the buoyancy added to the system.

The final buoyancy in each zone can be decomposed into two components at any moment in time: that associated with the displacement ventilation illustrated schematically in Figure 4-1 and that due to the buoyant plume rising from the source. Note, however, that the buoyancy increases in the dense zone only for $t > t_3$ after which the first front falls below the top of the bottom vent.

We now define Π_s, the source strength, as

$$\Pi_s = \frac{F_s t_s}{g'HW(L - \ell)} \geq 0 \tag{4-32}$$

Equation (4-27) indicates that Π_s is the ratio of the buoyancy added by the source over time t_s and the total buoyancy of the system at t =0.

Two flow regimes can be discerned on the basis the magnitude of Π_s: 1) a ventilation-dominated regime with $0 < \Pi_s \leq 1$ and 2) a source-dominated regime with $\Pi_s > 1$. In this study, particular attention is focused on the former. Note that, Π_s=0 is a special limiting case where there is no buoyancy source in the system. For $\Pi_s > 0$, one can further divide the ventilation dominated regime into regions where the influence of the source is weak, moderate and strong. Somewhat arbitrarily, we assign these regions to Π_s values in the respective ranges $0 < \Pi_s < 0.1$, $0.1 \leq \Pi_s \leq 0.5$ and $0.5 < \Pi_s \leq 1$.

4.2.2.3 Plume/ambient interaction

1- **Stratification in the light zone**:

The interface height in the light zone, h_b, is simultaneously a function of Q_e and the stratification in each zone. In order to determine the details of this stratification, we solve (3-7) and (3-8) subject to the following source conditions:

$$Q = 0 \tag{4-33-a}$$

$$M = 0 \tag{4-33-b}$$

$$F = F_s \tag{4-33-c}$$

at $z = 0$. Note that here the advection velocity of individual layers within the light zone, U, employed in (3-8) to describe the filling-box process, is defined as

$$U = \frac{Q_e - Q}{L - \ell} \tag{4-34}$$

The physical meaning of U remains the same, i.e. it prescribes the rate at which individual layers within the continuously stratified ambient are advected downwards.

2- **Stratification in the dense zone**:

The plume(s) that rise through the dense zone issue from circular vents along the bottom of the interior wall. Provided the vent spacing is sufficiently large, it is reasonable to assume that the rising plumes do not directly interact one with the other in which case the evolution of the volume flux with z is given by

$$\frac{\partial Q}{\partial z} = 2\alpha_d\sqrt{\pi M} \tag{4-35}$$

The entrainment coefficient for axisymmetric plumes is 0.082 and this is the value that we assign to α_d here [19]. Moreover, the layer advection velocity, U, in case of multiple plumes is given by [19]:

$$U = -\frac{N_b Q}{\ell} \tag{4-36}$$

Regarding the dense zone source conditions, at $z = h + D$ the volume, momentum and buoyancy fluxes are given by their counterpart quantities associated with the advecting layers in the light zone. For $t > t_3$ (3-7b), (3-7c) and (3-8), along with (4-35) and (4-36) should be solved over $0 < z < H - h_t$ so as to describe the ascending plume in the dense zone. For this purpose, the aforementioned numerical scheme of Germeles [21] is used.

4.2.3 Time scales

Based on the previous discussion, the two time scales of most relevance to the flows illustrated schematically in Figures 4-1 and 4-2 are: (i) the ending time t_E, a function of N_b and N_t, which is defined as the time when Q_e =0 or, equivalently, when $h_b/H = \ell/L$ and (ii) the time t_s during which the source is turned on. As noted earlier, values of t_s are chosen so that $t_2/t_s \ll 1$. This is a

reasonable assumption in real buildings provided the source is a heat source or solar gain where t_s is measured in hours and t_2 is measured in tens of seconds or possibly minutes.

For reasons that will become clear after we present and discuss Figure 4-10 below, t_E is the time-scale with which we choose to non-dimenionalize time t, unless otherwise stated. For this purpose a non-dimensional time-scale, τ, is defined as $\tau = t/t_E$.

4.2.4 Model predictions

In this sub-section, we combine the previous equations and present model predictions for both building zones of Figure 4-1. Because we have already discussed various features of the horizontal flows and stratification associated with the plume in Chapters 2 and 3, here attention is restricted to those new aspects and parameters associated with displacement ventilation. Most notably, the time evolution of the stratification and buoyancy in each zone (i.e. $\Delta_{a,c}$, $\Delta_{a,0}$, b_0, b_c) is presented and discussed.

Figure 4-3 shows the spatio-temporal evolution of the density in the light and dense zones. In Figure 4-3 the ambient stratification is shown only below the interface. Above the interface, there is unmodified light fluid, i.e. $-\Delta_{a,c}/g'$=$-\Delta_{a,0}/g'$=1 for $h_b/H<z/H<1$ and $1-h_t/H<z/H<1$. In Figure 4-3, $\Pi_s = 0.10$, $A^*/(\frac{\pi}{4}D^2) = 1.93$ and $\frac{\ell}{L}$ =0.5. The top of the bottom vent(s) extend 20% of the way up the common wall, i.e. $(h+D)/H$ =0.2. Also, $t_E = 118$ and $\tau_3 = \frac{t_3}{t_E}$ =1.45. Finally $\tau_2 = \frac{t_2}{t_E}$ =0.20, which is significantly smaller than the non-dimensional time the source is activated, i.e. τ_s =5.

Figure 4-3 confirms that the motion of the first front differs in a nontrivial way from that considered in Chapters 2 and 3. Here it follows a non-monotonic trend; up until τ =0.787, all the stratified layers in the light zone, including the first front, move upwards. Thereafter, the time rate of change of h_b is small enough that the layers, which always move downwards relative to the interface, now also move downwards relative to a fixed observer. Such behavior is also reflected by (4-34); initially $Q < Q_e$ and $U > 0$. Due to a progressive drop in the

hydrostatic pressure difference between the two zones, however, Q_e decreases so that, eventually, $Q > Q_e$ and U<0.

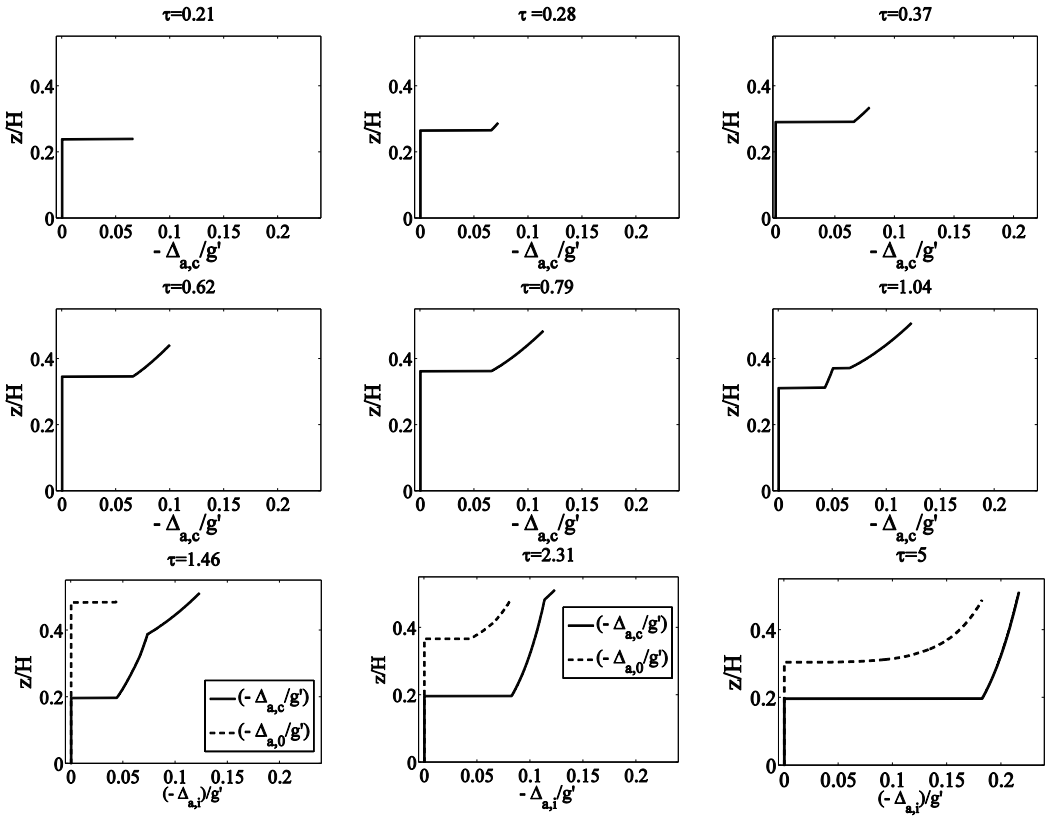

Figure 4-3. Dimensionless stratification profiles, scaled by $-g'$, with respect to elevation, scaled by H, at different dimensionless times, τ. The solid and dashed curves correspond to the stratification in the light and dense zones, respectively. The actual times are t =1, 10, 20, 50, 70, 100, 150, 250 and 568 sec. $\Pi_s = 0.10$, defined by (4-32), and $A^*/(\frac{\pi}{4}D^2) =$ 1.93.

Concerning the light zone stratification, at τ =1.01, when $U \leq 0$, we have $-\Delta_{a,c}/g' = 0$ for $0<z/H<0.37$ and $-\Delta_{a,c}/g' > 0$ for $0.37< z/H <1$. $-\Delta_{a,c}/g' = 0$ corresponds to the dense fluid density; therefore, due to entrainment of this dense fluid, density in the plume becomes comparable to that of the ambient at an elevation below the interface. At this elevation and, consistent with the approach taken in Chapters 2 and 3, we assume that the plume spreads in the lateral direction. For the panels with τ=1.04, 1.47 and 2.31 in Figure 4-3, this elevation is evident as the kink in the solid curve that appears at z/H=0.37, 0.39 and 0.48, respectively. As the filling-box process continues, a progressively larger fraction

of the ambient layer becomes density-stratified which results in smaller density within the plume and, as a result, the kink disappears in the stratification profile corresponding to τ =5 in Figure 4-3.

Regarding the dense zone stratification, for $\tau > \tau_3$=1.45, the first front reaches the top of the bottom vents, and there is a flow of stratified ambient fluid into the dense zone that is characterized by N_b =3 vertically rising plumes in Figure 4-3. In contrast to the light zone the layers in the dense zone move in the downwards direction for all τ (>τ_3).

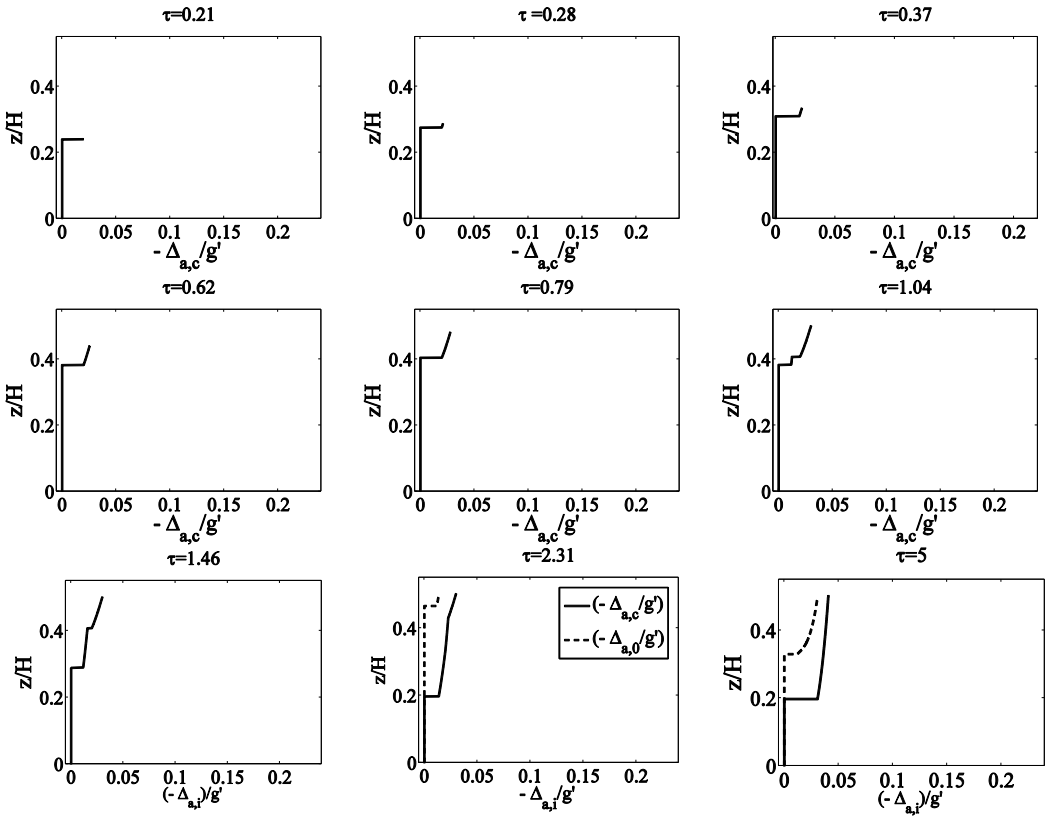

Figure 4-4. As in Figure 4-3 but with source strength of Π_s =0.017.

Figure 4-4 shows the evolution of density in the light and dense zones for Π_s = 0.017 representing a six-fold decrease of the source buoyancy flux as compared to Figure 4-3. Other parameters including t_E remain as in Figure 4-3. However, for this set of parameters, τ_3 =2.05, which is 2.27 times as large as the value reported for Figure 4-3. In fact τ_3 depends on dz_{ff}/dt, the advection velocity of the first front in the light zone, which is itself a function of Π_s. Also,

the non-dimensional density jump across the first front with the value of $-\Delta_{a,c}/g'$ =0.0199 in Figure 4-4 is smaller than that of Figure 4-3 where $-\Delta_{a,c}/g'$ =0.0657.

Figure 4-5 explores the dependence of non-dimensional time at which the first front reaches the top of the bottom vent with source strength and effective area. As Π_s decreases, τ_3 increases sharply: for weak sources of buoyancy larger times are required for the dense zone to feel the influence of the buoyant source in the adjacent light zone. Note, however, that for larger values of Π_s, τ_3 becomes less dependent on Π_s. Also characterized by Figure 4-5 is the influence of the effective area. For larger A^* values, the downward motion of the first front in the light zone begins more rapidly, leading to smaller values for t_3. However, t_E decreases by an even larger fraction so that $\tau_3 = t_3/t_E$ increases.

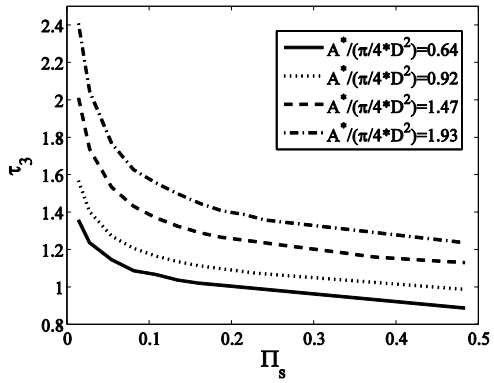

Figure 4-5. Variation of $\tau_3 = t_3/t_E$ with respect to Π_s for various $A^*/(\frac{\pi}{4}D^2)$.

By integrating the area confined by the vertical axis of Figure 4-3 or Figure 4-4, the buoyancy is obtained – see (4-19). Figure 4-6 shows the buoyancy divided by the initial total buoyancy, i.e. $b_{tot}(0)$ given by (4-21), versus non-dimensional time, τ, for various values of Π_s.

As shown by Figure 4-6a, the buoyancy in the light zone first decreases with time and then increases so that $db_c/d\tau$ =0 at a time close to τ =1. In particular, for Π_s =0.015, 0.075, 0.150 and 0.225, $b_c/b_{tot}(0)$ =0.5019, 0.5061, 0.5128 and 0.5197 as the local minimums at τ_{min} =1.01, 1.01, 1.00 and 1.00, respectively. The minimum occurs because by opening the top and bottom vents, light fluid is replaced by an equal volume of dense fluid, which results in a

decrease of buoyancy for $0<\tau<\tau_{min}$. At τ_{min}, Q_e has decreased to the point where negligible buoyancy is lost due to ventilation. As such, the buoyancy delivered by the source becomes increasingly more significant, so that it outweighs the buoyancy lost through the upper vent(s). Note from the four curves of Figure 4-6a, the slight change of slope that occurs when $\tau = \tau_3$ =2.06, 1.47, 1.29 and 1.21. When we have a source of buoyancy in the system, b_0 is not the mirror image of b_c (c.f. Chapters 2 and 3). For $\tau > \tau_3$, b_0 increases because the first front has now reached the top of the bottom vent, providing a further means by which buoyant fluid may enter the dense zone.

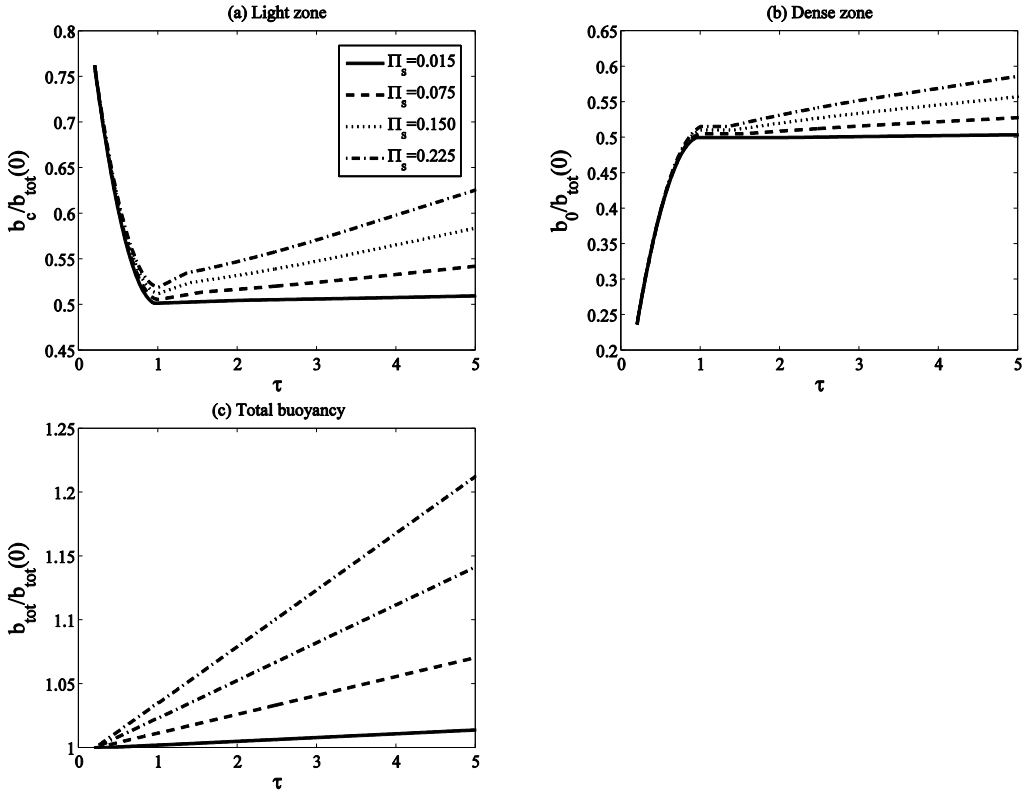

Figure 4-6. Buoyancy versus $\tau = t/t_E$ for ℓ/L = 0.5 and various Π_s; (a) light zone buoyancy, b_c, (b) dense zone buoyancy, b_0, and (c) total buoyancy, b_{tot}.

Note finally that the above analysis presumes the source to be ideal so that the source volume and momentum fluxes are zero. Given that we have reduced a distributed areal source to a line a source, this assumption is reasonable from the point of view of modelling solar gains in equator facing zone(s), but it is difficult to reproduce experimentally using a salt-bath system. For this reason, it is

necessary to extend the above model to include the case of a (weak) non-ideal source. In a real building, whose geometry is obviously fixed, a non-ideal source acts to increase the interior pressure, particularly along the ceiling. Even so provided $\Pi_s << 1$, one can assume the density deviation of any point from its initial value is small and that the system remains Boussinesq.

4.3 Laboratory experiments

The experiments were conducted in a 227.5 cm long, 25.0 cm wide and 34.5 cm deep glass tank. A 25.0 cm wide by 57.5 cm tall perforated divider 1.5cm in thickness was used to subdivide the tank. This divider was placed inside the tank to form a fixed ℓ =72.5 cm long space that served as the dense zone. A second divider was also used to limit the tank length to L=149 cm. In this way, the entire flow field could easily be captured using a single camera. Dividers were held in place using putty and silicon glue, which eliminated any leakage of fluid.

Density differences were produced by addition of sodium chloride and were measured using an Antor Paar DMA 4500 densitometer with a precision of ±0.00005 gcm^{-3}. Fresh ($\rho_c \simeq$0.9984 gcm^{-3}) and saline ($\rho_0 \simeq$1.0400 gcm^{-3}) water served as the light and dense fluids, respectively, and were replenished after each experiment. Whereas for most experiments g' =0.40±0.02 ms^{-2}, a limited number of experiments using 0.18<g'<0.49 ms^{-2} were also conducted to ensure that viscous effects played only a second-order role. More formally, a Reynolds number was defined as

$$\mathrm{Re} = \frac{\sqrt{g_0' H^3}}{2\nu_{water}} \tag{4-37}$$

Experiments were conducted in the range 1×10^4<Re<3×10^4 so that, as with the analogue flow in real buildings, transport is overwhelmingly due to turbulent, rather than molecular, effects [20]. Red food dye was added to the either the dense or light fluid for visualization purposes.

The tank was filled with fresh water to a depth of H =21±0.5 cm so that the distance (h=1.5 cm) from the top vent to the free surface matched the distance from the bottom vent to the bottom of the tank. The experiments were carried out for the range of $1\leq N_b \leq 3$ and $1\leq N_t \leq 3$, where N_b and N_t are the integer

number of open vents along the bottom and top of the dividing wall, respectively. The vents were circular with diameter 2.54 cm and were closed using rubber stoppers. At the beginning of a particular experiment, special care was taken to remove the stoppers simultaneously so as to avoid a two-layer exchange flow through any one vent.

A plume nozzle was placed at the bottom of the tank along the end wall of the light zone and was supplied by a constant-head pump consisting of fresh water that flowed from a bucket placed on the floor. The pump in question is a Masterflex L/S peristaltic device with an electric drive and an RPM range of 1 to 100. It supplied fresh fluid at a constant rate over the course of each experiment. Values of Q_s and t_s in the respective ranges of $1<Q_s<6$ ml s^{-1} and $600<t_s<5400$ s were used, which resulted in source strength values in the range $0.01\leq \Pi_s \leq 0.28$ according to which the flow was always ventilation-dominated. Larger values of Π_s were avoided because they either entail (i) large Q_s so that the plume is in actuality a buoyant jet (Hunt and Kaye [21]), (ii) large $\rho_0 - \rho_c$ so that the system is non-Boussinesq and/or (iii) large t_s over which there is an appreciable change of elevation of the free surface.

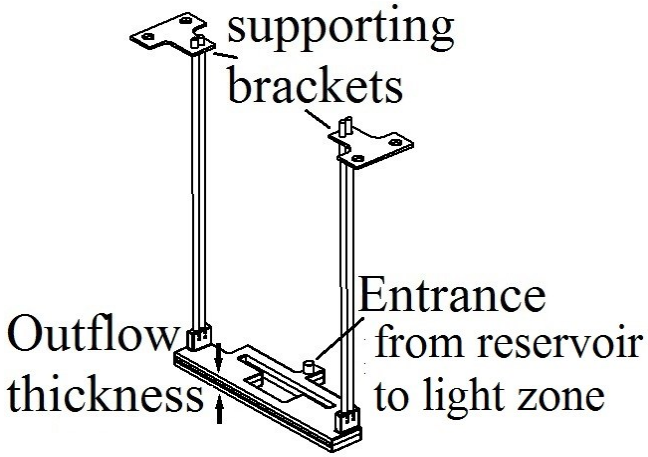

Figure 4-7. Schematic of the nozzle.

The plume nozzle was designed using SolidWorks and was manufactured by rapid prototyping. Using the current design, as confirmed by experimental observations, the outflow is a uniform horizontal line plume. Figure 4-7 shows a schematic of the nozzle (also see Appendix F for the details of dimensions),

which, as much as possible, was designed so as to produce a flow that was uniform along its length. The nozzle was fixed to the front and back face of the tank with special brackets manufactured using a water jet cutter. The plume nozzle was always positioned at $z = 0$. The plume fluid in the experiments exits from a slot just above this level; however, the 6 mm nozzle thickness (indicated in Figure 4-7) is small compared to the interface height, which measured approximately 40 and 105 mm at starting and ending time, respectively and, in theory we assumed the plume is originated at $z = 0$.

By employing a 30.5 cm in by 182.9 cm in light-sheet (Electric Vinyl, PNP1724), the tank was uniformly backlit. Images were recorded using a LaVision Imager E-lite camera with 35 mm Nikon AF Nikon lens. The linear gain of the CCD camera and direct recording to digital format reduced noise and simplified subsequent processing. A MATLAB code was developed and used for analysis of the experimental data in order to measure the velocity and depth of the horizontal flows as well as the time rate of change of interface height in both zones. By identifying the location of a sudden change of pixel intensity, we could straightforwardly estimate the front position and, by extension, the front speeds of either a gravity current or bore. A similar methodology was used to estimate the interface elevations in the dense and light zones. The ending time measured as the time the takes for the interface to reach 98% of its steady state value. Note, however, that the depths of the horizontal currents varied along their length achieving, in the case of the gravity current, a maximum at the raised head and a minimum between the head and the tail. To avoid such complications in the present analysis we only report interface heights for $\tau > \tau_2$.

We used a conductivity probe (Precision and Measurement Engineering, MSCTI) mounted on a vertical traverse (Velmex, X-Slide), whose translational speed was typically 5 mm/s, which was found to be small enough not to disturb the dense or light zone ambient fluid. Consistent with Chapters 2 and 3, a linear relationship between the measured voltage and the fluid density was assumed and five stock samples were used for calibration purpose. Density measurements using the conductivity probe were made only at the end of a particular

experiment, i.e. for $\tau > \tau_s$. For times smaller than τ_s, the stratification continued to evolve as a function of time. Because the probe had a finite vertical velocity, the associated measurement did not correspond to an instantaneous snapshot of the density field, but rather to an evolving field measured over a time interval of, say, ~ 40 s. On the other hand, by using image processing techniques, we were able to track the time evolution of the interface heights to a temporal resolution equal to the frame rate of the camera which was 17 Hz.

4.4 Results and discussion

4.4.1 Comparison between theory and experiment

Experimental snapshots of the propagation of the dense gravity current through the light zone are provided in Figure 4-8 in which N_b = N_t =1. Figure 4-8 through the light zone are provided in Figure 4-8 in which $N_b = N_t$ =1. Figure 4-8 also shows in panel f the corresponding front position of the gravity current, x_N as a function of time. The reason Figure 4-8 starts at 1 s on horizontal axis is that there is a starting phase during which there are both cross and along channel flows. Hence, we postponed the report of data until the cross channel flow diminishes so that the assumption of span-wise uniformity becomes reasonable.

Figure 4-9 shows the time evolution of the interface in the light zone for the same experiment as in Figure 4-8. For τ <1, the interface height increases appreciably; however, panel e indicates that as τ →1, dh_b/dt drops significantly. A similar trend is observed for the interface height in dense zone, h_t.

Error bars, indicated in Figure 4-9 and elsewhere, are based on the results of repeat experiments, conducted for select combinations of N_b, N_t, F_s and t_s. Uncertainty analyses are based on the standard deviation of an ensemble of measurements with a confidence limit of 68% [22].

(a) $\tau = 0.0049$

(b) $\tau = 0.0073$

(c) $\tau = 0.0097$

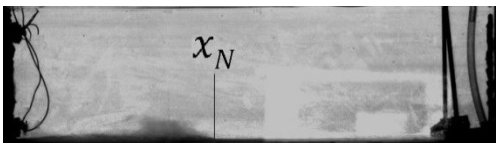

(d) $\tau = 0.0121$

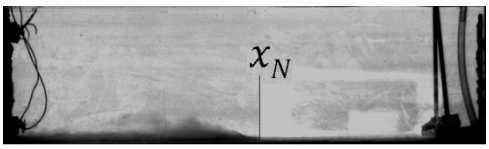

(e) $\tau = 0.0145$

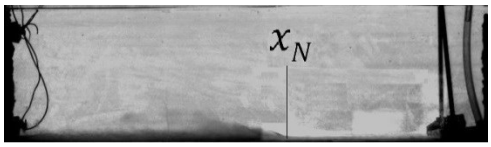

(f)

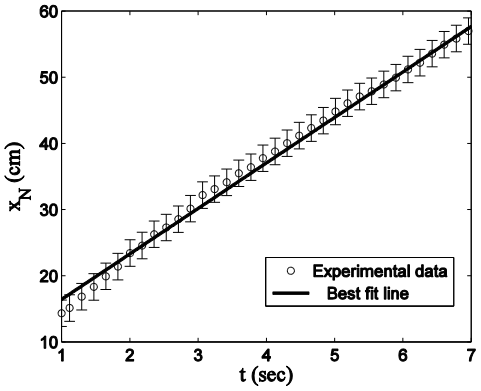

Figure 4-8. Time evolution and front position of the bottom gravity current when $N_b = N_t = 1$, $Re = 4520$ and $\ell/L = 0.49$. The field of view measures 22 cm tall by 77 cm long. Also $H = 21$ cm. The wires that appear on the left-hand side of the experimental images are connected to solid rubber stoppers and indicate closed vents. On the right-hand side of the images is the nozzle, which is not activated in this case. Only part of the field of view (measuring 22 cm tall by 77 cm long) is shown.

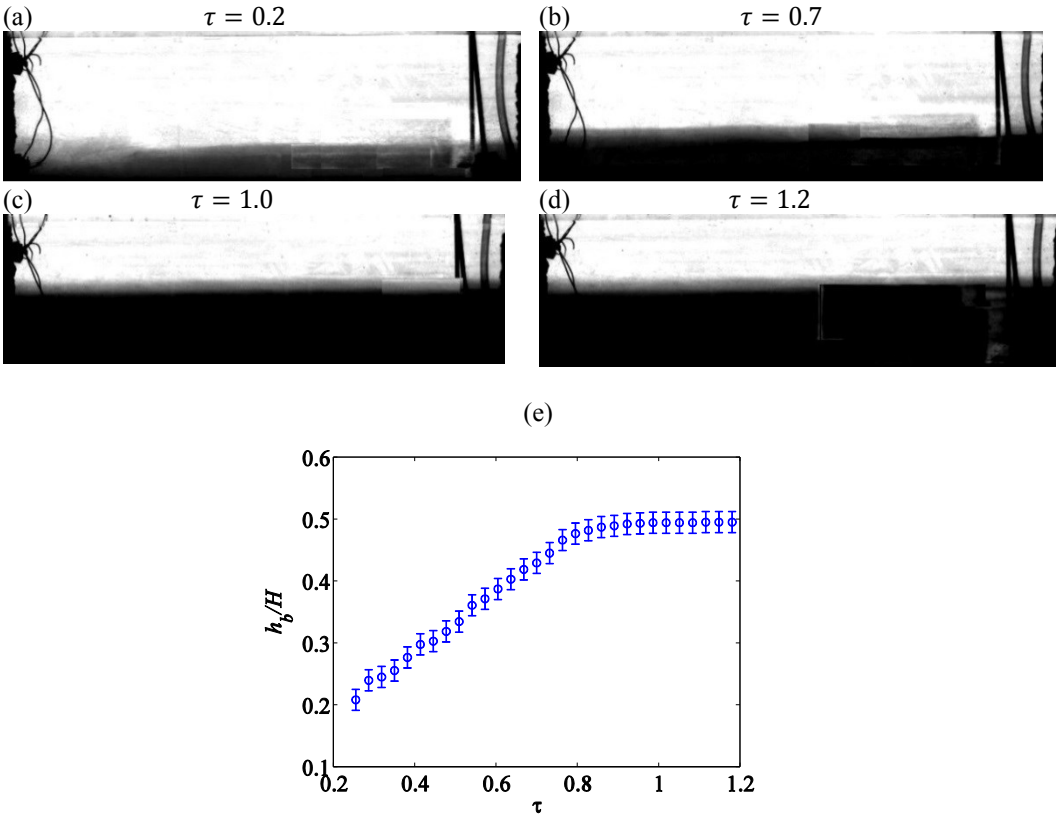

Figure 4-9. Time evolution of the interface height where, in contrast to Figures 4-1 and 4-2, the clear and dark fluid have respective densities ρ_0 and ρ_c. Only part of the field of view (measuring 22 cm tall by 77 cm long) is shown. These images show the later time evolution corresponding to the images presented in Figure 4-8.

Expanding on the results shown in Figure 4-9e, Figure 4-10 shows the variation of interface height in the light and dense zones as a function of time for various source buoyancy fluxes and effective vent areas. As expected, the rate of change of h_b and h_t is more substantial for $\tau \lesssim 0.6$. Conversely when $0.6 \leq \tau < 1$, the rate of increase is comparatively slow and for $\tau > 1$, it is identically zero. The eventual time independence of h_b and h_t is not only predicted by theory; it is also strongly suggested by the laboratory measurements where, in general, no distinguishable variation of interface height is observed for $\tau > 1$. Moreover, for larger values of the effective area, the depth of the internal bore at $\tau = \tau_2$ is larger, so that h_b or h_t start off with a larger value.

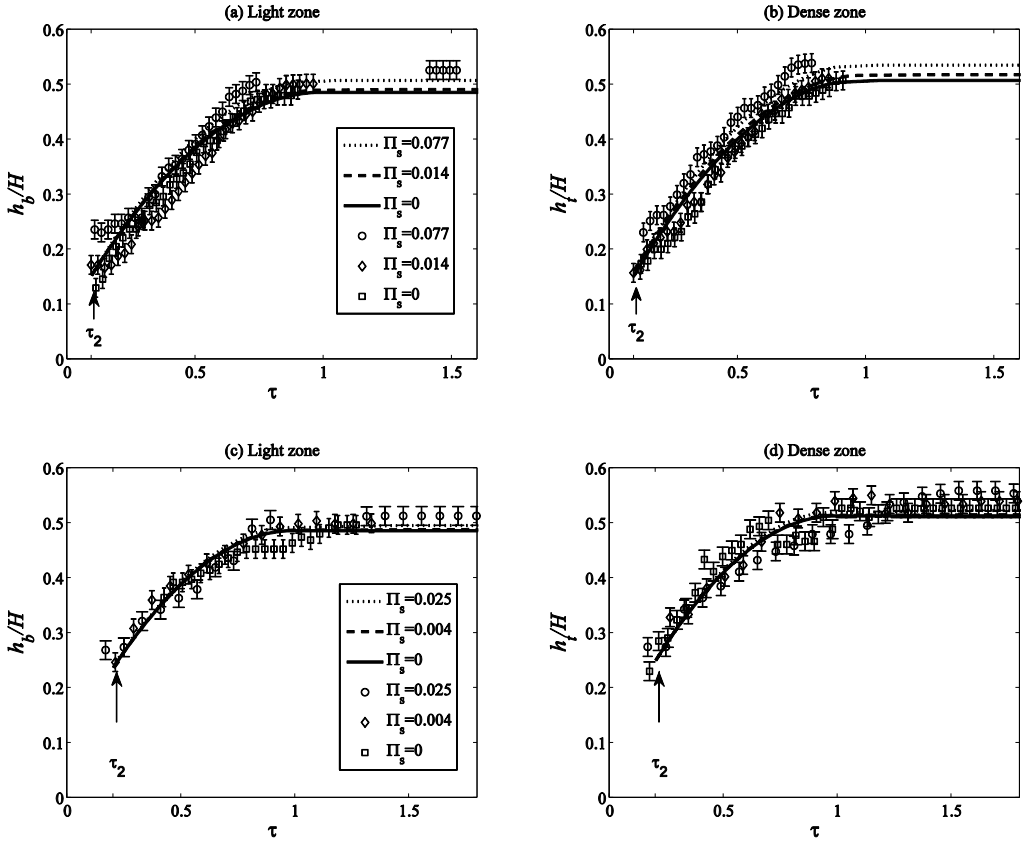

Figure 4-10. Interface height in the light (h_b/H) and dense (h_t/H) zones versus non-dimensional time τ. $A^*/(\frac{\pi}{4}D^2)$ =0.64 for panels (a) and (b), $A^*/(\frac{\pi}{4}D^2)$ =1.93 for panels (c) and (d). Symbols and lines correspond to experimental and analytical data, respectively. Data points in (b) and (d) are indicated in the legend of (a) and (c), respectively.

From the different panels of Figure 4-10, it can be shown that for $\tau > \tau_2$ and fixed source conditions, the interface height follows a universal trend for all values of $A^*/(\frac{\pi}{4}D^2)$, provided time is scaled by t_E. This observation affirms the physical importance of t_E, defined by (4-13), in displacement ventilation flows of the type illustrated schematically in Figure 4-2.

Figure 4-11 shows the variation of $t_E/t_{E,max}$ as a function of $A^*/(\frac{\pi}{4}D^2)$. (Similar results are obtained for other values of the source strength). Here, $t_{E,max}$ =361 s is the maximum ending time and, for this set of experiments, corresponds to the minimum value of A^*. As noted in connection with Figure 4-

10, the vent size has a significant effect on the starting value of h_b and h_t. A^* also determines how quickly the light zone exchanges fluid with the dense zone. Hence, by increasing A^* in Figure 4-11, $t_E/t_{E,max}$ decreases.

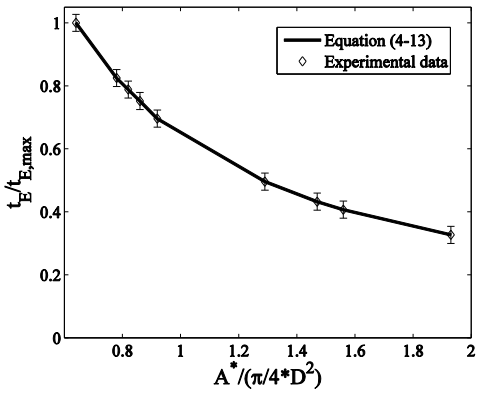

Figure 4-11. Variation of the ending time, $t_E/t_{E,max}$, as a function of effective area, $\frac{A^*}{\frac{\pi}{4}D^2}$. Here $t_{E,max}$ =361 s. The analytical data, shown by a solid line, is given by (4-13).

Regarding $-\Delta_{a.0}/g'$ and $-\Delta_{a,c}/g'$, there exists an extensive volume of experimental data. Therefore only select experiments are analyzed in detail, whereas in other cases the explicit interrogation of the data is less intensive. As mentioned in Section 4.3, only the final stratification is measured. The superscript f denotes such a final state, which is measured at τ_s. Figures 4-12 to 4-15 show the comparison between the experimental and theoretical results for both the light and dense zones. These figures are different from Figures 4-3 and 4-4 because the stratification is now shown as a function of z/H over the entire depth of the control volume. Consistent with Figures 4-3 and 4-4, however, $\tau_s = t_s/t_E$ is in 4-13 to 4-15 set to be large enough so that there develops a non-trivial stratification in the light zone as would be expected in most architectural scenarios of interest.

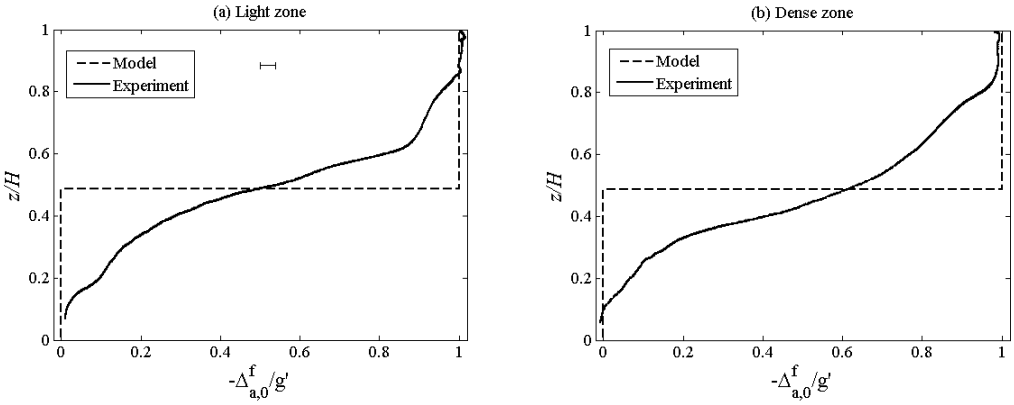

Figure 4-12. Experimental (solid) and theoretical (dashed) stratification profile in the (a) light and (b) dense zone as a function of z/H for Π_s=0 and $A^*/(\frac{\pi}{4}D^2)$=1.93. A representative error bar is shown in panel a.

In comparing theory and experiment, we must consider the role of Kelvin-Helmholtz instabilities and the turbulent mixing that follows there from. Such instabilities result in interfacial mixing which in turn causes a smearing of the sharp interface predicted, for example, in Figure 4-12. Thus even in the absence of a source of buoyancy there is in the experimental data a non-trivial stratification of density in each zone that is attributed to the turbulent mixing associated simply with the propagation of the horizontal currents. This mixing is not accounted for by our equations because, to our knowledge, no analytical model is able to describe such mixing in a straightforward manner.

Figure 4-13 makes apparent the influence of the source buoyancy flux, i.e. $F_s/F_e(0)$, where $F_e(0) = g'Q_e(0)$ is the buoyancy flux associated with the exchange flow at $t = 0$. For larger values of the source buoyancy flux, the average density in the light and dense zones below the interface increases in both the theoretical and experimental data. Also z/H =0.2, which corresponds to the top of the bottom vent, is the height at which stratified ambient fluid flows from the dense zone into the light zone. Hence, no further stratification is observed in the theoretical curves for $0 < z/H <$0.2 in Figure 4-13.

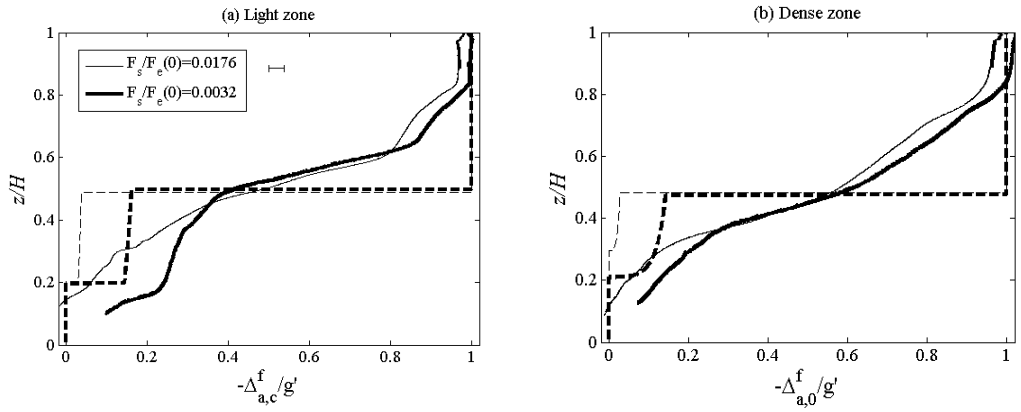

Figure 4-13. Experimental (solid) and theoretical (dashed) stratification profiles in the (a) light and (b) dense zones as a function of z/H for two different values of $F_s/F_e(0)$ with $F_e(0) = g'Q_e(0)$. $A^*/(\frac{\pi}{4}D^2)$=1.93 and τ_s =5. Theoretical and experimental data are shown by the dashed and solid lines, respectively. A representative error bar is indicated in panel a.

The influence of τ_s is characterized by Figure 4-14. Not surprisingly, if the source is active over longer times, the stratification evolves to a greater extent in each zone. Also, for larger values of τ_s, there is greater opportunity for the entrainment of ambient fluid by the plume and, as a result, the stratification below the interface is predicted to be sharper. In both the theoretical and experimental data, a sharper stratification below the interface is evident for large τ_s.

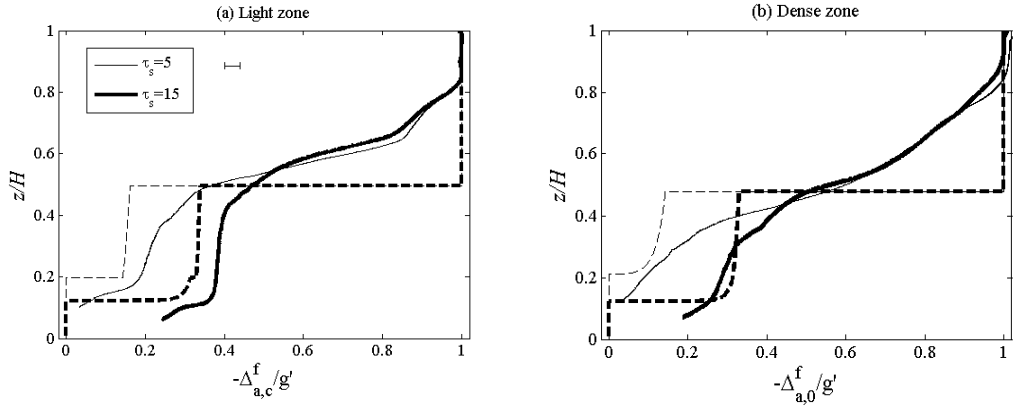

Figure 4-14. Experimental (solid) and theoretical (dashed) stratification profiles in the (a) light and (b) dense zones as a function of z/H for two different values of τ_s. $A^*/(\frac{\pi}{4}D^2)$=1.93 and $F_s/F_e(0)$ =0.0176.

Finally, Figure 4-15 shows the impact of the number of open vents on the stratification profiles in both zones. Clearly, A^* plays a minor role in the final stratification in either zone, a feature that is apparent from both the theoretical and the experimental data.

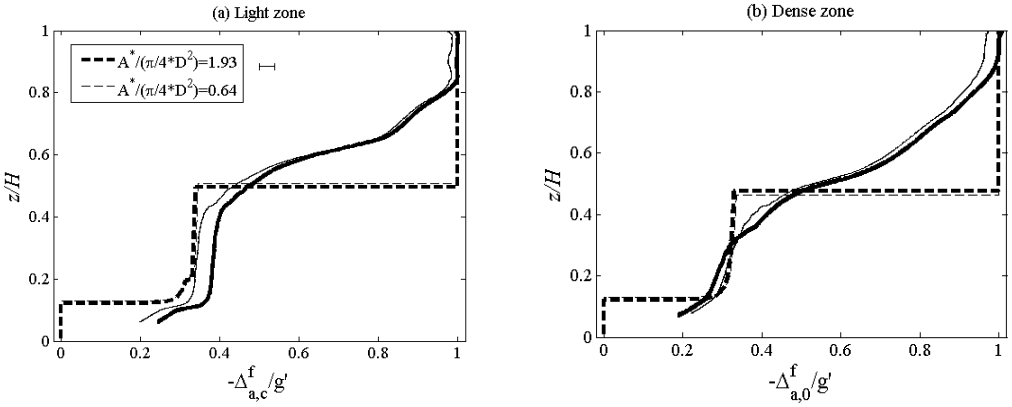

Figure 4-15. Experimental (solid) and theoretical (dashed) stratification profiles in the (a) light and (b) dense zones as a function of z/H for two different values of $A^*/(\frac{\pi}{4}D^2)$ and Π_s=0.28.

As explained previously, the analytical model ignores interfacial mixing. Therefore in all of Figures 4-13 to 4-15 a better agreement between prediction and measurement is observed in the lower stratified layer. The reason is the stratification caused by the source is confined to the region below the interface, an assumption that matches well our qualitative experimental observations. The process of forming this stratified layer includes entrainment into the plume, which acts to decrease the volume of the fluid resultant from mixing by Kelvin-Helmholtz billows. Better agreement for elevations below the interface is important because in buildings, the temperature distribution in the occupied region has the most direct impact on occupants' perceptions of thermal comfort.

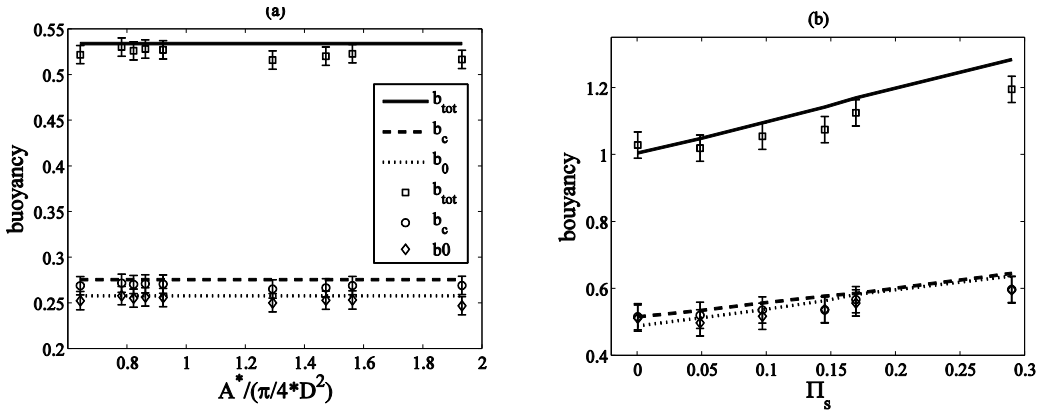

Figure 4-16. Total, light and dense zone buoyancy, i.e. b_{tot}, b_c and b_0, respectively, as functions of (a) $A^*/(\frac{\pi}{4}D^2)$ for $\Pi_s = 0.0483$ and (b) Π_s for $A^*/(\frac{\pi}{4}D^2)$ =1.93. The lines and markers correspond to analytical and experimental data, respectively.

By integrating the density profiles over height, one can determine the buoyancy of either zone. Figure 4-16a shows results of this calculation plotted against $A^*/(\frac{\pi}{4}D^2)$ for Π_s =0.0483. Clearly, the effective area is not expected to alter the final buoyancy provided $\tau_s > \tau_3$ and this prediction is in very good agreement with our laboratory measurements. To analyze the impact of the source strength on the final buoyancy and also to verify the accuracy of our experimental measurements in a different way, we carried out a further set of experiments with $A^*/(\frac{\pi}{4}D^2)$ =1.93 and different values of Π_s as shown in panel (b) of Figure 4-16. By increasing Π_s, the buoyancy, b_s, added by the source also increases. Therefore in Figure 4-16b, the buoyancy in each zone increases as a monotone function of the independent variable. A similar trend is expected for other values of $A^*/(\frac{\pi}{4}D^2)$. As Figure 4-16 makes clear, despite the fact that the point-by-point agreement between the solid and dashed curves of Figures 4-13 to 4-15 is sometimes lacking, the predicted final buoyancy may still agree well with laboratory measurements.

4.4.2 Applications to attached solarium design

Table 4-1 summarizes the impact of the geometrical parameter A^*, whose dependence on N_b and N_t is given by (4-7), as well as the source strength Π_s

whose dependence on F_s and t_s is given by (4-32) on various design parameters for displacement exchange flow.

Table 4-1. Summary of the influence of the source and vent parameters on various design quantities in the displacement ventilation exchange flow illustrated schematically in Figures 4-1 and 4-2. The quantitative influence in question can be assessed by making reference to the appropriate figure, indicated in parentheses.

Variable and range of values	$-\Delta^f_{a,c}/g'$: Light zone stratification (below the interface)	$-\Delta^f_{a,0}/g'$: Dense zone stratification (below the interface)	b^f_c / $b_{tot}(0)$: Light zone buoyancy	b^f_0 / $b_{tot}(0)$: Dense zone buoyancy	t_E: Ending time
$0.01<\Pi_s<0.28$	Strong (Fig. 4-14a)	Strong (Fig. 4-14b)	Weak (Fig. 4-16c)	Weak (Fig. 4-16c)	Weak (Fig. 4-10)
$0.64<\frac{A^*}{\frac{\pi}{4}D^2}<1.93$	Neutral (Fig. 4-15a)	Neutral (Fig. 4-15b)	Neutral (Fig. 4-16a)	Neutral (Fig. 4-16a)	Strong (Fig. 4-11)

For the case of non-interacting plumes considered here, the terminal stratification and buoyancy in either zone are not impacted by the number of open vents when $\tau_s > \tau_3$. However, the ending time, which is indicative of the evolution time-scale for h_b and h_t, is strongly influenced by N_b and N_t. These observations are especially important when buoyancy differences are due, not as we have assumed thus far to temperature differences, but rather to the presence of some noxious gas or harmful suspended particulate. In this case, knowledge of the temporal evolution of the interface heights and, equivalently, the variation of Q_e, is critical in estimating how long an occupant has to vacate a particular building zone. In terms of an attached solarium and adjacent building zone, it is obviously advantageous to have $\tau_s > \tau_3$ so as to derive the greatest possible benefit from the solar gains in the zone more likely to be inhabited by building occupants. Consistent with the results displayed in Figures 4-13 to 4-16, the impact of the source on the final buoyancy is weak for the range of parameters employed in our experiments. However, as shown by Figures 4-13 to 4-15 and consistent with Figures 4-3 and 4-4, the influence of the source parameters can be substantial even for $\Pi_s < 1$ in that the details of the density stratification can be non-trivially

altered by changing F_s or t_s and this may, in turn, non-trivially impact the degree of thermal comfort experienced by those inside the building.

In the context of occupant comfort, energy use and attached solaria, we briefly examine a simple case study whose results are summarized in Table 4-2. As a first design consideration, we assume that H =3.6m with a plan area of 10m×10m for each zone. Source strengths of $\Pi_s = 0.5$ and 0.1 are considered here, which correspond to $t_s = 3060$ and 15300 s, respectively, for F_s =2.0×10^{-3} m^{4}s^{-3}. Such a source of buoyancy mimics the daily-averaged solar gain for a typical day in April in a city located at 42.4° latitude in North America [25, 26]. Consistent with our experiments, it is further assumed that ℓ/L =0.50 with $A^*/(\frac{\pi}{4}D^2)$ =1.96 and 0.64. An initial temperature difference of 5ºC is assumed between the building zone and the attached solarium[3]. Note also that, $\tau_s > \tau_3$ so that there will develop stratification in the dense zone.

For this example, the temperature difference between the interface and the floor, ΔT_{IF}, may be one half of the initial temperature difference between the adjacent zones for Π_s=0.5. The corresponding value when Π_s=0.1 is only 10%, affirming that the degree of vertical temperature stratification is directly related to the source conditions as encapsulated by Π_s.

Also examined in Table 4-2, is the relative change of the average temperature of the air in the occupied portion of the building zone due to the exchange flow plus the heat added by the source. Consistent with Chapter 3, ΔT_{ave} is computed by spatial averaging the temperature confined to the lower 2m of the building zone, comparable to the height of a tall occupant. By increasing the source buoyancy flux, this average temperature increases as much as 50% of the initial temperature difference.

Finally, Table 4-2 shows the total amount of heat, as well as the fraction of heat due to the presence of the source, per unit volume of air space transferred from one building zone to the other. For a source with a larger source strength of

[3] Air properties are calculated at 17ºC.

Π_s =0.5 the amount of total heat transferred increases by 36% compared to the case with $\Pi_s = 0.1$.

Table 4-2. Comparison of select design parameters; a. Percent relative temperature difference between the interface and the floor (building zone), b. Percent relative increase of the terminal average temperature in the occupied portion (building zone).

source buoyancy flux	$\frac{A^*}{\frac{\pi}{4}D^2}$	τ_3/τ_s	$\frac{\Delta T_{IF}}{T_0-T_c}(\%)$[a]	$\frac{\Delta T_{ave}}{T_0-T_c}(\%)$[b]	Heat transfer solely associated with the source (kJ/m^3)	Total heat transfer (kJ/m^3)
Π_s =0.5	0.64	0.14	53.1	52.3	0.61	1.90
	1.93	0.07	51.2	52.5	0.61	1.90
Π_s =0.1	0.64	0.70	17.3	15.9	0.10	1.39
	1.93	0.33	17.7	16.2	0.11	1.39

4.5 Conclusions

The exchange flow between two adjacent confined zones of slightly different initial density, first developed by Nabi and Flynn [10-11], is extended to cases where there are top and bottom vents, which are opened simultaneously. Two scenarios are considered: the ventilation problem in the absence or presence of a source of buoyancy, which results in a plume that rises from the floor of the light zone. An analytical model is derived and similitude experiments are carried out to assess the validity of the theoretical results. Attention is focused on the influence of the effective area, the source buoyancy flux and the time during which the source is switched on.

In the absence of a source, it is shown that, by opening the vents, the pressure difference between the two zones drives the exchange flow, whose intensity, as measured by the volumetric exchange flux, Q_e, is a decreasing function of time. Two counterpart horizontal currents propagate along the bottom (top) of the light (dense) zone. Upon reflection from the end walls two internal

bores are generated and propagate back toward the vent(s). In our model, a horizontal interface in each zone divides the upper layer, which is comprised of fluid having the initial density of the light zone, from the lower layer, comprised of fluid whose density is larger than that of the light zone. The time rate of change of interface height is given as a function of the volumetric exchange rate, Q_e, in (4-8), which itself is a function of the effective area, A^*. After the ending time, t_E defined by (4-13), the interface elevations are steady and Q_e is zero.

We separately consider a more involved problem in which there is an isolated source of buoyancy located at the floor of the light zone and which supplies fluid of density ρ_c over a dimensional time interval t_s with (time-invariant) buoyancy flux F_s. The source strength Π_s, defined by (4-32), is the ratio of the buoyancy added by the source to the total buoyancy of the system at time t =0. Two distinct flow regimes are defined: a ventilation-dominated regime with Π_s <1 and a source-dominated regime with Π_s >1. Particular attention is here focused on the former. When a source is present, there remains an exchange of mass and buoyancy between the two zones for $t > t_E$. Indeed the flow into the dense zone is characterized by one or more ascending plumes so that a non-trivial stratification of density appears in both building zones for sufficiently large time.

As described more thoroughly in Table 4-1, the terminal stratification and buoyancy in either zone depends on Π_s, which is a function of t_s and F_s, although such dependence is weak for small values of source strength. In like fashion, the effective area has a minor impact on the final stratification profiles if t_s is larger than t_3, which is the time required for the first front in the light zone to advect downward and reach the top of the bottom vent. The results are compared with similitude experimental data in Section 4.4. Many predictions, such as the variation of interface height in the light (h_b/H) and dense (h_t/H) zones as functions of time, the presence and evolution of a nontrivial stratification below the interfaces, etc. are all reproduced in the laboratory. Regarding the stratification data, better agreement is observed below the interface where the stratification associated with the plume, which we do model, has a more long-lived influence than interfacial mixing, which we do not take into account. Also,

stratification evolves to a greater extent and becomes sharper for larger values of the source parameters τ_s and $F_s/F_e(0)$.

The current model is derived for relatively modest values of $(h+D)/H$ where h, D and H are defined by Figure 4-1. For larger values of h or D the flow is not completely horizontal, unidirectional and uniform. This does not necessarily limit the applicability of our model if one recalls that in systems that exploit displacement ventilation the vents should be located as near to the floor and ceiling as possible, so that the exchange of mass and buoyancy may occur over the broadest possible range of interface heights [27]. We only show experimental results for cases where ℓ/L =1/2, i.e. the two zones have the same size. This scenario is generally representative, however: for 0.10<ℓ/L<0.90, qualitatively similar results are expected and the model can be applied straightforwardly. Cases where $\ell \ll L-\ell$ or $\ell \gg L-\ell$ indicating a significant asymmetry in the size of adjacent zones are of less architectural relevance. In these strongly asymmetrical cases, one zone is thin and tall and overturning may occur, which is associated with large scale vertical circulation rather than the filling-box process, which is at the core of the analytical model presented in Section 4.2.

The fundamental understanding gained by the current study paves the way for further novel extensions. For instance, one may examine the exchange flow between two zones separated by both vents and one or more doorways. Further investigations are also worthwhile to analyze the impact of the orientation (vertical versus horizontal), shape (axisymmetric vs. rectilinear) and elevation of the buoyant source.

Appendix 4-A

Four scenarios of ventilation

As mentioned in Section 4.2.1, depending on the relative value of $\frac{h_{2,b}}{(h+D)}$ and $\frac{h_{2,t}}{(h+D)}$, four different scenarios may arise. Figure 4-A-1 depicts the associated schematics of each – see also Table A-1. In all cases, (4-5), (4-8) and (4-10) are valid. In other words, only the starting condition (4-9) is different in the four

scenarios and we have to integrate each case using the appropriate value of h_b and h_t at $t = t_2$.

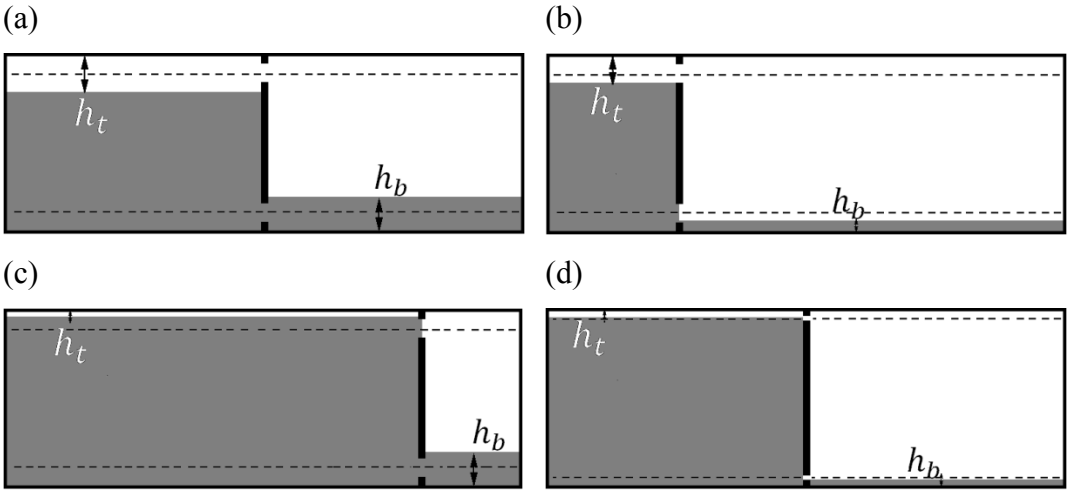

Figure 4-A-1. Schematic of the four scenarios of displacement exchange flow in the absence of a source (a) $\frac{h_{2,b}}{(h+D)} > 1$ and $\frac{h_{2,t}}{(h+D)} > 1$, (b) $\frac{h_{2,b}}{(h+D)} > 1$ and $\frac{h_{2,t}}{(h+D)} < 1$, (c) $\frac{h_{2,b}}{(h+D)} < 1$ and $\frac{h_{2,t}}{(h+D)} > 1$, (d) $\frac{h_{2,b}}{(h+D)} < 1$ and $\frac{h_{2,t}}{(h+D)} < 1$ at $t_{2,b}$ and $t_{2,t}$, respectively. The horizontal dashed lines indicate the position of mid-elevation of the vent at $z = h + D/2$.

As shown by panel (a), in the first scenario we have $\frac{h_{2,b}}{(h+D)} > 1$ and $\frac{h_{2,t}}{(h+D)} > 1$ at $t = t_{2,b}$ and $t = t_{2,t}$, respectively. Such a scenario results in starting conditions of the form of (4-9) and, therefore, the interface height is given by (4-11). This is the most common scenario considering the range of effective areas we considered in this study (Table 4-A-1).

Alternatively, we may have $\frac{h_{2,b}}{(h+D)} > 1$ at $t = t_{2,b}$ but $\frac{h_{2,t}}{(h+D)} < 1$ at $t = t_{2,t}$ when the area of the top vent is small. Panel (b) shows such a scenario. The appropriate equation for the interface height, valid for small t, then reads

$$\frac{h_b}{H - \left(h + \frac{D}{2}\right)} = \left[1 - \left(\sqrt{\left(1 - \frac{h_{2,b}}{H - \left(h + \frac{D}{2}\right)}\right)} - \frac{\left(t - t_{2,b}\right)}{t_E^*}\right)^2\right] \qquad \text{(4-A-1a)}$$

Table 4-A-1. Summary of the four possible flow scenarios in terms of the bottom and top vent areas or, equivalently, the interface elevations at $t = t_{2,b}$ and $t = t_{2,t}$. Note that $t_{2,b} = t_{2,t}$ when ℓ/L =1/2.

Flow scenario	$\frac{h_{2,b}}{(h+D)}$	$\frac{h_{2,t}}{(h+D)}$	$\frac{a_b}{\frac{\pi}{4}D^2}$	$\frac{a_t}{\frac{\pi}{4}D^2}$
I	>1	>1	≥0.5	≥0.5
II	>1	<1	≥0.5	≤0.5
III	<1	>1	≤0.5	≥0.5
IV	<1	<1	≤0.5	≤0.5

where

$$t_E^* = \sqrt{\frac{\left(H - \left(h + \frac{D}{2}\right)\right)}{g'}}\left(\frac{2(L-\ell)W}{A^*}\right) \tag{4-A-1b}$$

As summarized in Table 4-A-1, we may have $\frac{h_{2,t}}{(h+D)} > 1$ at $t = t_{2,t}$ but $\frac{h_{2,b}}{(h+D)} < 1$ at $t = t_{2,b}$ when the area of the bottom vent is small. Panel (c) shows such a scenario. The appropriate equation for the interface height, valid for small t, then reads

$$\frac{h_t}{H - \left(h + \frac{D}{2}\right)} = \left[1 - \left(\sqrt{\left(1 - \frac{h_{2,t}}{H - \left(h + \frac{D}{2}\right)}\right)} - \frac{\left(t - t_{2,t}\right)}{t_E^*}\right)^2\right] \tag{4-A-2a}$$

where

$$t_E^* = \sqrt{\frac{\left(H - \left(h + \frac{D}{2}\right)\right)}{g'}}\left(\frac{2\ell W}{A^*}\right) \tag{4-A-2b}$$

Finally, for small values of A^* we may have $\frac{h_{2,b}}{(h+D)} < 1$ and $\frac{h_{2,t}}{(h+D)} < 1$ at $t = t_{2,b}$ and $t = t_{2,t}$, respectively. Panel (d) shows such a scenario. The appropriate equation for the interface height, valid for small t, then reads

$$h_b = \frac{Q_e}{(L-\ell)W}\left(t - t_{2,b}\right) + h_{2,b} \qquad \text{(4-A-3)}$$

The interface elevations thus vary linearly with time.

In the scenarios described schematically by panels b through d, the interface height in each zone increases so that, in due course and for $t > t_2$, $\frac{h_{2,b}}{(h+D)} > 1$ and $\frac{h_{2,t}}{(h+D)} > 1$. Therefore, one may use the analysis of Section 4.2 directly in evaluating the longer time evolution of the two-zone system.

References

[1] Hunt GR, Van den Bremer TS. Classical plume theory: 1937–2010 and beyond. IMA J Appl Math 2011;76:424-448.

[2] Sandbach SD, Lane-Serff GF. Transient buoyancy-driven ventilation: Part 1. Modelling advection. Build Environ 2011;46:1578-1588.

[3] Mingotti N, Chenvidyakarn T, Woods AW. The fluid mechanics of the natural ventilation of a narrow-cavity double-skin facade. Build Environ 2011;46:807-823.

[4] Kaye NB, Flynn MR, Cook MJ, Ji Y. The role of diffusion on the interface thickness in a ventilated filling box. J Fluid Mech 2010;652:195-205.

[5] Merci B, Maele K. Numerical simulations of full-scale enclosure fires in a small compartment with natural roof ventilation. Fire Safety J 2008;43:495-511.

[6] Linden PF, Lane-serff GF, Smeed DA. Emptying filling boxes: the fluid mechanics of natural ventilation. J Fluid Mech 1990;212:309-335.

[7] Phillips JC, Woods AW. On ventilation of a heated room through a single doorway. Build Environ 2004;39:241-253.

[8] Caulfield CP, Woods W. The mixing in a room by localized finite-mass-flux source of buoyancy. J Fluid Mech 2002;471:33-50.

[9] Kuesters AS, Woods W. The formation and evolution of stratification during transient mixing ventilation. J Fluid Mech 2010;670:66-84.

[10] Nabi S, Flynn MR. The hydraulics of exchange flow between adjacent confined building zones. Build Environ 2013;59:76-90.

[11] Nabi S, Flynn MR. Influence of geometric parameters on the eventual buoyancy stratification that develops due to architectural exchange flow. Build Environ 2014;71:33-46.

[12] Gladstone C, Woods AW. On buoyancy-driven natural ventilation of a room with a heated floor. J Fluid Mech 2001;441:293–314.

[13] Kaye NG, Hunt GR. The effect of floor heat source area on the induced airflow in a room. Build Environ 2010;45:839–847.

[14] Kaye NG, Hunt GR. Time-dependent flows in an emptying filling box. J Fluid Mech 2004;520:135-156.

[15] Baines WD, Turner JS. Turbulent buoyant convection from a source in a confined region. J Fluid Mech 1969;37:51-80.

[16] Killworth PD, Turner JS. Plumes with time-varying buoyancy in a confined region. Geophys Astro Fluid 1982;20 (3-4):265-291.

[17] Morton BR, Taylor GI, Turner JS. Turbulent gravitational convection from maintained and instantaneous sources. J Fluid Mech 1956;234:1-23.

[18] Germeles AE. Forced plumes and mixing of liquids in tanks. J Fluid Mech 1975;71:601-623.

[19] Wong ABD, Griffiths RW. Stratification and convection produced by multiple turbulent plumes. Dynam. Atmos Ocean 1999;30:101-123.

[20] Tatcher TL, Wilson DJ, Wood EE, Craig MJ, Sextro RG. Pollutant dispersion in a large indoor space: Part 1 – Scaled experiments using a water-filled model with occupants and furniture. Indoor Air 2004;14: 258–271.

[21] Hunt GR, Kaye NG. Virtual origin correction for lazy turbulent plumes. J Fluid Mech 2001;435:377-396.

[22] Taylor JR. An introduction to error analysis: The study of uncertainties in physical measurements. 2nd ed. University Science Books; 1997.

[23] Kotsovinons NE. A study of the entrainment and turbulence in a plane buoyant jet. Report No. KH-R-32, California Institute of Technology, Keck Laboratory, Pasadena, Calif., Aug., 1975.

[24] Rouse H, Yih C, Humphreys H. Gravitational convection from a boundary source. Tellus 1952;4:200-210.

[25] ASHRAE Handbook of fundamentals. Chapter 15: Fenestration. New York: The American Society of Heating Refrigeration and Air Conditioning Engineers; 2009. p. 15.1–21.

[26] Online solar gain calculator: http://www.susdesign.com/windowheatgain/ (source: US Geological Survey. http://www.usgs.gov/)

[27] Rooney GG, Linden PF. Strongly Buoyant Plume Similarity and 'Small-fire' Ventilation. Fire Safe J 1997;29:235-258.

Chapter 5

Conclusions

This thesis considers Boussinesq exchange flow between two finite regions theoretically and experimentally. Such an exchange flow may arise between adjacent building zones that are separated by a doorway or by top and bottom vents. Our specific motivation is to investigate the physical affects that influence the exchange flow and to describe the interior stratifications that result there from.

Many researchers have studied the exchange flows between an interior and exterior that are mostly associated with steady state heat and mass transfer. My research has revealed that the less-studied problem involving two strictly interior building zones is much more complicated because the associated dynamics are highly coupled. As a result, the evolution of stratification evolution is non-trivial and time-varying plumes arise whose quantitative details depend on the exchange flow parameters.

Two scenarios are considered in-depth depending on the divider type; (i) two zones separated by a single common doorway, and, (ii) two zones separated by top and bottom vents. The former scenario is studied in Chapters 2 and 3 and is associated with a two-layer exchange flow at the doorway. The latter is examined in Chapter 4 and is characterised with two oppositely-directed single-layer exchange flows through the top and bottom vents.

In either case, the philosophy is to superpose various flow elements, e.g. turbulent plume(s), gravity currents, internal bores plus the exchange flow itself for purposes of deriving a composite model that can describe pertinent dynamical features such as the time-variable stratification in either zone and its connection to appropriate source conditions. For the most part, model results are successfully corroborated against measurements from similitude experiments.

In Section 5.1, we present a detailed summary of Chapters 2, 3 and 4. Thereafter in Section 5.2.1, we highlight key contributions stemming from the work as a whole. A number of limitations of the model are presented and discussed in Section 5.2.2. Finally, in Section 5.3 ideas for future research are identified.

5.1 Summary

Our analysis begins by considering two adjacent zones separated by a common doorway in Chapter 2. By opening the doorway, two qualitatively different kinds of flow are observed, namely a buoyant plume that rises through the dense zone and a horizontal gravity current that propagates along the bottom of the light zone. At early times the model proposed by Dalziel [1] and Dalziel and Lane-Serff [2] connects the two halves of the problem. The dense zone ambient fluid is entrained into the plume and, according to the filling-box process described by Baines and Turner [3], a stable ambient stratification results. Conversely, after a finite time, t_1, the gravity current will reflect back toward the opening in the form of an internal bore. When this internal bore reaches the doorway at $t = t_2$, the nature of exchange flow, which is previously time-invariant and critical, changes and becomes transient and sub-critical. This alters the source conditions for the plume and hence the subsequent evolution of

stratification in the dense zone for $t \geq t_2$. Most notably, the velocity and density jump across the first front steadily decrease once the exchange flow becomes transient.

We restrict our attention in Chapter 2 to cases where the terminal position of the first front is above the top of the doorway. Similitude experiments are carried out to assess the model validity. The connection of such salt-bath experiments to the full-scale flows within the real buildings is discussed in Section 2.3. We find that our predictions for the dense gravity current, internal bore and light gravity current speeds, match well with laboratory experiments in a broad region of the parameter space (Figure 2-11). We also examined the top gravity current, whose dynamics are ignored in many studies. The Froude number of the top gravity current depends on the entrainment coefficient and elevation of the plume source.

An extension of the investigation presented in Chapter 2 includes examining circumstances where, at $t = t_3$, the first front reaches then falls below the plume source, which is assumed to be located at the top of the doorway. Such a scenario introduces additional complexities compared to the problem studied in Chapter 2; this allows us to implement our model over a broader range of geometrical parameters, e.g. taller doorway heights (expressed in non-dimensional variables as h/H) and less voluminous dense zone (expressed in non-dimensional variables as ℓ/L). In aggregate, two regimes of exchange flow may be identified depending on the terminal elevation of the first front: an $R > 0$ regime where this terminal elevation lies above the top of the doorway, and an $R < 0$ regime for which the first front is advected below this point. As we document in Chapter 3, there exist significant differences between the two regimes. When $R > 0$, a two-layer stratification is expected in the light zone with lower and upper layers comprised of fluid from the dense and light zones, respectively. When $R < 0$, on the other hand, there develops a layer of continuously varying density below the top of the doorway implying a non-trivial stratification in both building zones. Two sub-scenarios therefore are admitted: $t_3/t_2 > 1$, for which the internal bore reaches the doorway before the first front,

and $t_3/t_2 < 1$, in which the opposite occurs and more dynamic deviations with $R > 0$ scenario arise.

The analytical results outlined above are compared with similitude experimental data in Section 3.4. Many predictions, such as a sharp change in the stratification below the top of the doorway, the near equality of the terminal dense and light zone stratification for large values of h/H, the presence of a nontrivial stratification in the intermediate layer of the light zone, etc. are all reproduced in laboratory experiments. Stratification profiles and the total buoyancy exchanged between the two zones are also predicted using a model that presumes both zones to be well mixed for all t. When h is large, both well-mixed and stratified models predict comparable terminal buoyancies, however, for smaller h there is up to an order of magnitude difference.

In Chapter 4, the exchange flow between two adjacent confined zones is extended to cases where there are top and bottom vents, which are opened simultaneously. Two scenarios are considered: the ventilation problem in the absence and in the presence of a source of buoyancy. In the latter case, the source is modelled as an ideal plume that rises from the floor of the light zone. A notable difference between the exchange flow of Chapter 4 with those considered in Chapters 2 and 3, is that the exchange flow discussed in Chapter 4 terminates after a finite time and there develops a steady-state interface in each zone. For early times, the interface in the light (dense) zone ascends (descends) rapidly. Thereafter their rate of growth steadily drops, before becoming time-independent when $t = t_E$. When a buoyancy source is present, a non-trivial stratification develops first in the light zone then in the dense zone.

Of particular importance is to categorize the details of this stratification in terms of the effective vent area, A^*, and the source strength, Π_s. The latter variable is defined as the ratio of the buoyancy added by the source to the total buoyancy of the system at $t = 0$. Particular attention is given to ventilation regimes with $\Pi_s < 1$. The results are compared against similitude experimental data in Section 4.4. Many predictions, such as the time evolution of the interface heights, the presence and evolution of nontrivial stratifications below the

interfaces, etc. are reproduced in the laboratory. Experiments confirm, moreover, that for larger values of the source buoyancy flux or the time over which the source is activated, the stratification is sharper and develops to a greater extent.

5.2 Thesis contributions and limitations of the model

5.2.1 Major contribution

A major purpose of this research is to make an assessment concerning the applicability of filling-box-type models compared to more complicated approaches such as CFD numerical simulations in the context of modelling the exchange flow between adjacent zones of different density. My results indicate that the filling-box models of the type introduced in Chapters 2-4 lead to quantitatively meaningful results even though they fall far short of resolving all of the length-scales associated with a high Reynolds number flow. Through a non-trivial modification and synthesis of existing models, the analytical results proved to be successful insofar as the prediction of bulk properties, such as the front speed of the dense or light gravity currents and the time variation of buoyancy in either zone. Regarding the stratification profiles, the success of the model depends on the geometrical parameters. For instance, in Chapters 2 and 3, and for large values of h/H there is only modest agreement between the composite analytical model and the results derived from similitude salt-bath experiments. Also in Chapter 4, because the model does not account for the interfacial mixing associated with the propagation of the horizontal currents and because there is no mechanism for redistributing this mixed fluid in the upper layer, differences again arise. However, even for the cases with more pronounced deviations of the theoretical results from the experimental data, many qualitative features, such as presence of a light zone intermediate layer or the near equality of the dense and light zone stratification when $R < 0$, are faithfully predicted.

A further contribution of this thesis was to point out some substantial limitations associated with well-mixed models wherein the details of the interior stratification in either zone are assumed to be unimportant. It was shown in Chapters 2 and 3 that such well-mixed models do not predict the dependence of

the terminal values of buoyancy and stratification on the doorway height. Moreover the well-mixed model results are in good agreement with measurements only for select geometrical parameters, e.g. large h/H values. The critical assessment of well-mixed models to buildings consisting of two (and, by extension, more) distinct zones is an important feature of this study because these well-mixed models enjoy widespread use by practitioners due to their relative simplicity.

Examples of modern buildings that rely on passive solar heating so as to minimize energy consumption are Net Zero Energy Buildings (NZEBs). NZEBs are defined as residential or commercial buildings that, in year-round, balance their energy needs (electrical plus thermal) with economical, locally available, clean, and renewable sources and, therefore, represent an efficient and advanced solution for reducing energy use within buildings [4]. A hallmark of NZEBs is the exploitation of freely-available solar gains. However, making efficient use of the heat collected in a solarium, say, requires a detailed understanding of convective heat transfer and architectural exchange flows.

We endeavored to identify combinations of design and operational variables for which adjacent building zones having a simple geometry are maximally efficient in terms of distribution of energy and temperature. For instance, in Chapter 2 it was shown that after the internal bore reaches the doorway, there is substantial drop in the exchange flow. This signifies that building zones separated by a single doorway exchange a considerable fraction of their buoyancy over a time-scale t_2. On the other hand, if the two zones are separated by both top and bottom vents the exchange of mass and buoyancy should be instead scaled by t_E. In this latter circumstance, moreover, and when there exists a source of buoyancy in one zone, the other zone will benefit from this added buoyancy only after t_3.

Returning to the flow scenario of Chapters 2 and 3, the terminal position of the first front is important insofar as thermal comfort or the distribution of energy between the two zones is considered. This position depends on the geometrical parameters h/H and ℓ/L as we indicate in the regime diagram

displayed in Figure 3-3. If the height of the dense zone far exceeds that of the doorway, the terminal position of the first front may lie well above the occupied region suggesting no change to the occupied region temperature in spite of the addition of buoyancy to the building zone from the adjacent warmer space. In the opposite limit where h/H is large, a saturation behaviour arises in terms of the terminal buoyancy as indicated graphically in Figures 3-12 and 3-A-1. For prescribed ℓ/L, therefore, increasing the doorway height does not significantly change the amount of heat that is transferred in the long time limit.

5.2.2 Limitations and discussion

Notwithstanding a generally positive agreement between theory and experiment in most cases of Chapters 2-4, it should be emphasized that there are, in the context of real architectural flows, a number of simplifying assumptions that have been applied whose relaxation provides a fruitful area for further inquiry.

For the exchange flow considered in Chapters 2 and 3, by increasing the doorway height, the exchange flow rate increases. Thus the dense gravity current travels faster, the reflected bore arrives more rapidly at the doorway and the transition to a transient flow regime occurs sooner. Similarly, the gravity current that forms along the upper boundary of the dense zone and that is comprised of fluid discharged from the ascending plume also travels more quickly. The plume meanwhile does not rise strictly vertically as is assumed by our model equations but rather becomes inclined, particularly in the neighborhood of the source. As a consequence, when h/H is relatively large, we typically see a less favorable comparison between the measured and predicted density stratification in the dense zone.

A second limitation is that we restricted attention to the cases where ℓ is comparable to $L-\ell$, cases where $\ell \ll L-\ell$ or $\ell \gg L-\ell$ being of less architectural relevance. For extreme values of ℓ/L the gravity current and bore speeds may not remain constant in time. Moreover, if the building zone in which the stratification evolves is made to be thin and tall, overturning may be possible instead of the filling-box scenario.

Thirdly, the doorway width, w, is, in real buildings, less than the width, W, of the building zone. When $w/W < 1$, the plume source conditions will be slightly different from those studied here. Moreover, the plume itself will be different, i.e. it will not then be a line (two-dimensional rectilinear) in shape. Also, the top and bottom gravity currents will initially propagate both along and across the width of the zone. Based on the analysis of Dalziel and Lane-Serff [2], we expect qualitatively similar flow behavior between the $w/W < 1$ and $w/W = 1$ cases, however, this remains to be verified through detailed experimentation, either at full- or reduced-scale.

Regarding the exchange flow considered in Chapter 4, the plume source density is assumed to match the initial density of the light zone. Also, the source buoyancy flux is assumed to be constant over the time that the source is active. In actuality, the source may have a density smaller than the density of the light zone. Moreover, we restrict attention to a ventilation-dominated regime where $\Pi_s < 1$. In real buildings, the buoyant plume source conditions may result in large values of source strength with $\Pi_s > 1$ and, hence, the exchange flow may become buoyancy-dominated.

Finally, and in cases where the plume(s) do not ascend all the way to the ceiling, it is assumed that the maximum rise height corresponds to the point of neutral buoyancy, not of zero momentum flux. Whereas this simplification is consistent with the analyses of Killworth and Turner [5] or Bolster and Caulfield [6], other studies, e.g. Lin and Linden [7], have more deliberately investigated the influence plume-top entrainment, i.e. the entrainment that occurs between the points of zero buoyancy and momentum flux. Whether plume-top entrainment is a significant factor for select combinations of, say, h/H and ℓ/L, has not been investigated here, however, one can address this question by incorporating analyses such as Lin and Linden [7]. At the very last, the entrainment of ambient fluid into the plume between two elevations of zero buoyancy flux and zero moment flux is associated with increasing of the density within the plume so that when it spreads out the new layer density is slightly larger than the one expected if the plume were spread out at the zero buoyancy flux level. Hence, the new

added layer into the environment spreads out at some height between the zero buoyancy flux and zero moment flux elevation. The penetrative entrainment [7] takes into account the mixing that occurs into the plume between the two mentioned elevations. Such penetrative entrainment is determined in the light of experimental data. At the very last, the entrainment of ambient fluid into the plume between the elevations of zero buoyancy flux and zero moment flux acts to decrease the density of the discharged fluid so that it then spreads above the neutral buoyancy level of the plume. Whether this difference of spreading height is a significant fraction of the interface height remains to be determined.

5.3 Future recommendations and further extensions of the model

As suggested by the discussion of Section 5.2.2, there exist a number of extensions to the present study whose examination may yield analytical models of improved physical realism. To reiterate, five direct extensions are

1. To supply some initial horizontal momentum to the plume based on the speed of the exchange flow. Germeles considered the inclined plume that ensues when a source of buoyancy is inclined [8]. The basic principles of plume entrainment and filling-box process of the ambient used in Chapters 2-4 are still valid but the boundary conditions are altered and an extra equation is needed to describe the trajectory of the plume.

2. To consider doorways with various shapes most immediately one whose width is less than that of the building.

3. To study, in the context of the analysis of Chapter 4, the buoyancy-dominated regime with large source strength values. Moreover, this analysis would be especially interesting to conduct for a building that contained one or more openings to the exterior so that it would be possible to achieve a steady state solution in the long time limit.

4. In either type of exchange flow considered in Chapters 2, 3 or 4, the problem can be extended by accounting for a time-varying source of buoyancy. The problem has a practical significance because solar radiation varies as the sun changes its position in the sky over the course of the day. We might also be able to consider a situation where there is a sudden change in the source buoyancy

flux, mimicking, say, a piece of electrical equipment that is turned on or off or the sudden arrival or departure of a large group of people.

5. To account for top plume entrainment when the plume reaches the negative buoyancy level. Approaches parameterizing penetrative entrainment, e.g. that one proposed by Lin and Linden [7], can be used to suitably adjust the entrainment coefficient according to the Richardson number associated with interface impingement.

More expansively, it would also be helpful to consider a number of extensions that follow less immediately from the present analysis. These include exploring the details of entrainment into the plume using either an advanced experimental method such Particle Image Velocimetry (PIV) or a numerical approach such as Direct Numerical Solution (DNS).

We may also consider a problem having multiple sources of buoyancy with unequal source strengths. In fact, the strength of heat sources within buildings may vary by at least an order of magnitude and range from weak to strong. Also, the heat sources may not all be activated at the same time. For instance, the building zone may first be exposed to the morning sun after which one or more occupants enter and active heat-generating equipment like computers. In such cases we know from the work of [9] that a multi-layer stratification is predicted to evolve in each zone where the precise stratification details depend on the ratio of source strengths.

The toxic combustion products from accidental fires in buildings are a major hazard, and efficient removal of smoke from populated sections of a building is essential for safe evacuation in the event of such a fire. One means of smoke removal is natural ventilation. Karlsson and Quintiere [11] showed that at a certain distance above the fire, a plume develops whose details are non-trivially similar to the buoyant plume dynamics considered in Chapters 2, 3 and 4. Rooney and Linden [12] proposed a modified entrainment relationship to address differences that arise for the case of non-Boussinesq, as compared to a Boussinesq, plume. Insofar as small fires are concerned, the interface height of the smoke layer “is little affected by departures from the Boussinesq value”. Thus

many of the dynamical features previously highlighted including the top gravity current (known in the fire literature as a ceiling jet) and the downwards advecting first front, have analogous properties to those features associated with the propagation of smoke through one or more building zones. Knowledge of the smoke temperature and velocity at the ceiling as well as mixing processes within the building is key for predicting the concentration of the contaminated air which may vent from the building and also for properly placing smoke detectors and sprinkler systems and developing sensible evacuation protocols.

Further investigation, which is also worthwhile to analyze, includes the study on the impact of the thermal storage units when the common wall or facades of either zone are not perfectly insulated. In this case, the conductive heat transfer through the wall should be also taken into account in addition to the convective heat transfer at the opening(s).

References

[1] Dalziel SB. Two-layer hydraulics: a functional approach. J Fluid Mech 1991;223:135-163.

[2] Dalziel SB, Lane-serff G. The hydraulics of doorway exchange. Build Environ 1991;26:2:121-35.

[3] Baines WD, Turner JS. Turbulent buoyant convection from a source in a confined region. J Fluid Mech 1969;37:51-80.

[4] Torcellini P, Pless S, Deru M, Crawley D. Zero Energy Buildings: A Critical Look at the Definition. ACEEE Summer Stud, Pacific Grove, California, USA (2006).

[5] Killworth PD, Turner JS. Plumes with time-varying buoyancy in a confined region. Geophys Astro Fluid 1982;20 (3-4):265-291.

[6] Bolster D, Caulfield CP. Transients in natural ventilation-A time-periodically-varying source. Building Serv Eng Res Technol2008;29,2:119-135.

[7] Lin YJP, Linden PF. The entrainment due to a turbulent fountain at a density interface. J Fluid Mech 2005;542:25-52.

[8] Germeles AE. Forced plumes and mixing of liquids in tanks. J Fluid Mech 1975;71:601-623.

[9] Shrinivas AB, Hunt GR. Transient ventilation dynamics induced by heat sources of unequal strength. J Fluid Mech, 2014;738:34-64.
[10] Bauman F and Webster T. Outlook for underfloor air distribution. ASHRAE J 2001;43(6):18-27.
[11] Karlsson B, Quintiere JG. Enclosure Fire Dynamics. CRC Press, 2000.
[12] Rooney GG, Linden PF. Strongly Buoyant Plume Similarity and 'Small-fire' Ventilation. Fire Safe J 1997;29:235-258.

Appendix A

Convection due to the heat flux and the buoyancy flux

In buoyancy-driven flows the velocity of the fluid is due to the action of buoyancy forces arising from variations in the density. This type of flow is usually produced by a heat source in the environment, but sometimes also by a finite source which injects a fluid of a lesser density from the environmental density and so also results in convective motions. Generally speaking, natural or free convection includes the convection flows induced by heat sources and buoyancy sources. The other type of convection, which includes inertial or mechanical driving forces in addition to those described previously, is categorized as forced convection.

At the large scale, heat convection manifests itself as atmospheric circulation near the earth surface. At small scale, one might alternatively consider the flow driven by a hot microchip in the CPU of a computer. Many researchers, e.g. Batchelor [1] and Linden [2], use the analogy between heat flux and buoyancy flux to investigate natural convection phenomenon and its influences on the environment. If a heat flux Θ is present, the equivalent buoyancy flux B imparted to the surrounding fluid is

$$B = \beta_{00} g \Theta / C_p \rho \tag{A-1}$$

where β_{00} is the thermal expansion coefficient, g is the gravitational acceleration, ρ is the density of the fluid and C_p is the specific heat capacity at constant pressure.

References

[1] Batchelor, GK. Heat convection and buoyancy effects in fluids. Quart J Roy Met Soc. 1954;80:339-358.

[2] Linden P. The fluid mechanics of natural ventilation. Annu Rev Fluid Mech, 1999;31:201–238.

Appendix B

One-sided line plume equations

Following a long line of earlier studies (Morton et al. [1], Baines and Turner [2], Germeles [3], Caulfield and Woods [4], Kaye and Hunt [5] and many others) the exchange flow analysis of Chapters 2, 3 and 4 employ the turbulent plume equations in parameterizing buoyant convection from internal heat sources. A rigorous derivation of these relations is given below.

B.1. Assumptions

The main assumptions are:

1) The effective width of the plume, b, is significantly smaller than the total area per unit width of the ambient, ℓ.
2) No large scale vertical circulation is established so that the ambient remains stratified from top to bottom. Baines and Turner [2] indicate that an overturning of the ambient is likely to be avoided provided that the base of the zone is larger than the height.
3) The buoyancy and velocity profiles of the plume are well-represented by Gaussian distributions

$$w_p = \overline{w} e^{-\frac{x^2}{b^2}} \tag{B-1}$$

$$g\frac{\rho_p - \rho_a}{\rho_{00}} = \Delta e^{-\frac{x^2}{\lambda^2 b^2}} \tag{B-2}$$

where $\Delta = g\frac{\overline{\rho}-\rho_a}{\rho_{00}}$. Baines and Turner [2] use the same profile for both velocity and density. However, Germeles [3] indicates that the density and velocity distributions may spread at different rates. Hence, λ defined in (B-2) is the Schmidt number. From Laser-Doppler Velocimetry (LDV) measurements by Kotsovinos [6] to recent Particle Image Velocimetry (PIV) measurements by Ezzamel, et al. [7], the Gaussian shape for time-averaged velocity profiles within the plume are reported in the literature.

4) The flow in both the plume and ambient is incompressible.
5) Taylor's hypothesis for entrainment applies so that the velocity of entrainment, u_e, is proportional to the local axial velocity at the center of the plume, $\overline{w}$, at that level. Symbolically, $u_e = \alpha\overline{w}$, where α is the entrainment coefficient (typically $0.08 < \alpha < 0.15$).
6) Only time-averaged velocity and density components are considered for the flow within the plume.
7) The flow is inviscid and diffusion in the scalar transport equation can be ignored. This is valid for large Reynolds and Peclet numbers, i.e. $Re \gg 1$ $Pe \gg 1$.
8) The Boussinesq approximation is applicable so that negatively and positively buoyant plumes are governed by the same set of equations [9]. Also density variations are omitted unless they are multiplied by gravity. Finally, we can re-write the energy equation in terms of buoyancy.
9) The flow within the plume is assumed to be one-dimensional, i.e. $u_p = 0$ if $x \neq b$ and $u_p = u_e$ for $x = b$.
10) The pressure distribution is hydrostatic.
11) A wall-bounded plume is assumed to be of half-width. Correspondingly, only one-half of the volume of ambient fluid is entrained into the plume as compared to a buoyant plume that is not wall bounded.

B.2. The governing equations

The governing equations for Boussinesq flows for both liquids and gases can be written as [10]:

$$\frac{\partial V_j}{\partial x_j} = 0 \tag{B-3a}$$

$$\frac{DV_i}{Dt} = -\frac{1}{\rho_{00}}\frac{\partial(p - p_{00})}{\partial x_i} + g_i\beta_{00}(T - T_{00}) + \nu_{00}\frac{\partial^2 V_j}{\partial x_j^2} \tag{B-3b}$$

$$\frac{DT}{Dt} = \kappa_{00}\frac{\partial^2 T}{\partial x_j^2} \tag{B-3c}$$

where ν_{00} and κ_{00} are respectively the kinematic viscosity and diffusivity and β_{00} is the volumetric expansion coefficient. Also V is the velocity, T is the temperature, ρ is the density and p is the pressure. Finally, x_i and t are independent spatial and temporal variables. Reference variables are denoted by subscript 00.

For the case of a line plume, we rewrite the equations (B-3) as

$$\frac{\partial u_p}{\partial x} + \frac{\partial w_p}{\partial z} = 0 \tag{B-4a}$$

$$\underbrace{\frac{\partial u_p}{\partial t}}_{=0;(6,9)} + \underbrace{\frac{\partial {u_p}^2}{\partial x} + \frac{\partial u_p w_p}{\partial z}}_{=0;(9)} = \underbrace{-\frac{1}{\rho_{00}}\frac{\partial (p-p_{00})}{\partial x}}_{=0;(10)} + g_x\beta_{00}(T-T_{00}) + \underbrace{\nu_{00}\frac{\partial^2 u_p}{\partial x_j^2}}_{=0;(7,9)} \tag{B-4b}$$

$$\underbrace{\frac{\partial w_p}{\partial t}}_{=0;(6)} + \underbrace{\frac{\partial u_p w_p}{\partial x}}_{=0;(9)} + \frac{\partial {w_p}^2}{\partial z} = \underbrace{-\frac{1}{\rho_{00}}\frac{\partial (p-p_{00})}{\partial z} + g_z\beta_{00}(T-T_{00})}_{=g\frac{(\rho_p-\rho_a)}{\rho_{00}};(8,10)} + \underbrace{\nu_{00}\frac{\partial^2 w_p}{\partial x_j^2}}_{=0;(7)} \tag{B-4c}$$

$$\frac{DT}{Dt} = \underbrace{\kappa_{00}\frac{\partial^2 T}{\partial x_j^2}}_{=0;(7)} \tag{B-4d}$$

Note that in writing (B-4), many terms are set to zero by making reference to the appropriate assumption, whose corresponding number is indicated in parentheses. Equation (B-4d) can be further simplified as

$$\frac{DB}{Dt} = \underbrace{\frac{\partial B}{\partial t}}_{=0;(5)} + \frac{\partial (Bu_p)}{\partial x} + \frac{\partial (Bw_p)}{\partial z} = 0 \tag{B-5}$$

where B is the buoyancy, which is proportional to the density deficiency defined as the density difference between the ambient and a reference fluid.

Equation (B-4) can be integrated with respect to x. According to assumption 11 the boundaries of integration are from 0 to ∞:

$$\int_0^\infty \frac{\partial u_p}{\partial x} dx + \int_0^\infty \frac{\partial w_p}{\partial z} dx = 0 \tag{B-6}$$

By using the Leibnitz integral theorem and applying assumption 3, one obtains

$$\frac{\sqrt{\pi}}{2} \frac{\partial (b\overline{w})}{\partial z} = \alpha \overline{w} \tag{B-7}$$

Similarly by integrating (B-4c) and (B-5) and also applying assumption 2, we find that

$$\frac{1}{\sqrt{2}} \frac{\partial \left(b\overline{w}^2\right)}{\partial z} = \lambda b \Delta \tag{B-8}$$

and

$$\frac{\lambda}{\sqrt{1+\lambda^2}} \frac{\partial (b\Delta\overline{w})}{\partial z} = -b\overline{w} \frac{\partial \Delta_a}{\partial z}, \tag{B-9}$$

respectively.

The above equations can be written in terms of the fluxes defined below

$$Q = \int_0^\infty w_p dx = \frac{\sqrt{\pi}}{2} b\overline{w} \tag{B-10a}$$

$$M = \int_0^\infty w_p^2 dx = \frac{\sqrt{\pi}}{2\sqrt{2}} b\overline{w}^2 \tag{B-10b}$$

$$F = \int_0^\infty \frac{g}{\rho_{00}} \left(\rho_p - \rho_a\right) w_p dx = \frac{\sqrt{\pi}\lambda}{2\sqrt{1+\lambda^2}} b\Delta\overline{w} \tag{B-10c}$$

Substituting (B-10) into (B-9), we find that

$$\frac{dQ}{dz} = \sqrt{2}\alpha \frac{M}{Q} \tag{B-11a}$$

$$\frac{dM}{dz} = \sqrt{\frac{1+\lambda^2}{2}} \frac{FQ}{M} \tag{B-11b}$$

$$\frac{dF}{dz} = Q \frac{\partial \Delta_a}{\partial z} \tag{B-11c}$$

B.3. Bounded environment

In a confined region, such as a building zone of depth H and cross sectional area A_t, integrating (B-4a) and (B-4d) provides an expression for the

evolution of the ambient stratification. The latter integration ensures that the downward volume flux in the environment at any elevation matches the upward volume flux in the plume, which yields

$$A_t U = Q \tag{B-12}$$

provided assumption (1) is valid. Secondly, integration of (B-4d), gives

$$\frac{\partial \Delta_a}{\partial t} + U \frac{\partial \Delta_a}{\partial z} = 0 \tag{B-13}$$

which implies that the density deficiency in the ambient at any elevation occurs only because of vertical advection, not because of any mixing or diffusive effects [2].

B.4. Analytical solution for the first front

Baines and Turner [2] exploited the fact that the first front of buoyant fluid advances through a uniform ambient. Hence, the properties of the plume below the front can be found analytically by setting Δ_a =0 for $z \leq z_{ff}$ where z_{ff} denotes the elevation of the first front. Doing so in (B-11c), gives $F = F_s$ for $z \leq z_{ff}$ with F_s as the source buoyancy flux per unit width of the ambient. In case of an ideal plume, whose source volume and momentum fluxes are zero, the fluxes within the plume for $z \leq z_{ff}$ can be expressed in terms of powers of z and the source buoyancy flux as follows

$$Q = (\beta^2 \gamma F_s)^{1/3} z \tag{B-14a}$$

$$M = (\beta \gamma^2 F_s^2)^{2/3} z \tag{B-14b}$$

$$F = F_s = \frac{\sqrt{\pi}\lambda}{2\sqrt{1+\lambda^2}} b w_p \Delta|_{z \to 0} \tag{B-14c}$$

$$\Delta = (\beta^{-2} \gamma^2 F_s^2)^{1/3} z^{-1} \tag{B-14d}$$

with $\beta = \sqrt{2}\alpha$ and $\gamma = \sqrt{\frac{1+\lambda^2}{2}}$. Using (B-14d), the density step at the front elevation is obtained by putting $z = z_{ff}$

$$\Delta_{ff} = (\beta^{-2} \gamma^2 F_s^2)^{1/3} z_{ff}^{-1} \tag{B-15}$$

The advection velocity of the first front, dz_{ff}/dt, is evaluated by combining (B-12) and (B-14). A further integration gives the following relationship between the first front elevation z_{ff} and time t:

$$\frac{t}{(\beta^2\gamma F_s)^{-1/3}A_t} = \ln\left(\frac{z}{H}\right)^{-1} \tag{B-16}$$

B.5. Analytical solution for the asymptotic state

Baines and Turner [2] present similarity solutions to (B-11), (B-12) and (B-13), i.e. the governing equations for filling box flows, in the long-time limit. They assume a linear relationship between Δ_a and t in (B-13) when $t \to \infty$. Furthermore they choose the following transformations to bring the governing equations to non-dimensional form:

$$\Delta_a = (\beta^{-2}\gamma^2 F_s^2)^{1/3} H^{-1}[f_0(\zeta - \tau)] \tag{B-17a}$$

$$\Delta_a = (\beta^{-2}\gamma^2 F_s^2)^{1/3} H^{-1}\, f(\zeta) \tag{B-17b}$$

$$w_p = (F_s\beta^{-1}/2)^{1/3} \tag{B-17c}$$

$$b = \pi^{-\frac{1}{2}}\beta H h(\zeta) \tag{B-17d}$$

$$U = (F_s^2\beta^2)^{\frac{1}{3}} H/A_t j(\zeta) \tag{B-17d}$$

$$t = (F_s^{-1}\beta^{-2})^{1/3} A_t \tau \tag{B-17e}$$

Here $\zeta = \frac{z}{H}$ and H is the depth of the environment. The non-dimensional ODEs then read

$$\frac{dj}{d\zeta} = -\psi \tag{B-18a}$$

$$\frac{d(\psi j)}{d\zeta} = -fh \tag{B-18b}$$

$$\frac{d(fj)}{d\zeta} = j\frac{df_0}{d\zeta} \tag{B-18c}$$

$$j\left(\frac{df_0}{d\zeta}\right) = 1 \tag{B-18d}$$

Baines and Turner [2] solved the above system of equations subject to a known source buoyancy flux F_s with $j = \psi = 0$ at $\zeta = 0$ by employing

perturbation techniques. They showed that the series solutions of (B-18) are of the form

$$j = \zeta^2 + \frac{1}{8}\zeta^2 + \frac{3}{160}\zeta^3 + \cdots \tag{B-19a}$$

$$j\psi = -\zeta + \frac{3}{8}\zeta^2 + \frac{7}{160}\zeta^3 + \cdots \tag{B-19b}$$

$$f_0 = 0.1422 - \log\zeta - \frac{1}{8}\zeta - \frac{11}{640}\zeta^3 \ldots \tag{B-19c}$$

along with the following two subsidiary algebraic equations: $j = -\psi h$ and $fj = -(1-\zeta)$. These results, despite their simplifying assumptions, are still insightful for practical situations.

B.6. Germeles scheme for the numerical solution of (B-11), (B-12) and (B-13)

In many instances related to building ventilation the source of buoyancy is also associated with a finite volume and momentum flux. An alternate (numerical) method to solve such non-ideal sources was proposed by Germeles [3], whose approach also describes the ambient stratification associated with discharged plume fluid as it is advected towards the source. At the heart of his algorithm is the assumption that the plume evolution, when marching forward in time, can be decoupled from the evolution of the ambient stratification. A series of layers with discrete density steps represent the ambient stratification. Hence, the Germeles scheme is sometimes called a "layering" method. For each instant of time, the equations are solved in the vertical direction while the ambient stratification is assumed frozen. This is equivalent to integrating (B-11) from the source origin till the top of the control volume to find the volume, momentum and buoyancy fluxes within the plume. Equations (B-12) and (B-13) are then solved so that volume and buoyancy conservation are satisfied.

References

[1] Morton BR, Taylor GI, Turner JS. Turbulent gravitational convection from maintained and instantaneous sources. J Fluid Mech 1956;234:1-23.

[2] Baines WD, Turner JS. Turbulent buoyant convection from a source in a confined region. J Fluid Mech 1969;37:51-80.

[3] Germeles AE. Forced plumes and mixing of liquids in tanks. J Fluid Mech 1975;71:601-623.

[4] Caulfield CP, Woods W. The mixing in a room by localized finite-mass-flux source of buoyancy. J Fluid Mech 2002;471:33-50.

[5] Kaye NB, Hunt GR. Time-dependent flows in an emptying filling box. J Fluid Mech, 2004;520:135-156.

[6] Kotsovinos NE, List EJ. Plane turbulent buoyant jets. Part 1. Integral properties. J Fluid Mech 1977;81:25-44.

[7] Hunt GR, Van den Bremer TS. Classical plume theory: 1937–2010 and beyond. IMA J Appl Math 2011;76:424-448.

[8] Fan LN, Brooks H. 1969 Numerical solutions of turbulent buoyant jet problems. W. M. Keclc Lab. of Hydraulics and Water Resources, Calij. Inst. Tech. Rep. KH-R-18.

[9] Spiegel EA, Veronis G. On the Boussinesq Approximation for a Compressible fluid. Astrophys J, 1960;131:442-447.

[10] Grey DD, Giorcini A. The validity of the Boussinesq approximation for liquids and gases. Int J Hear Mass Transfer, 1975;19:545-551.

Appendix C

Uncertainty analysis

The bound on the experimental error with a given confidence interval is defined as the uncertainty [1-3]. Here the experimental error is regarded as the difference between the measured value and the true value.

For a measured parameter y, two types of uncertainties are defined: bias, systematic or instrument uncertainty, $\epsilon_{y,B}$, and the precision or random uncertainty, $\epsilon_{y,p}$. The bias uncertainty is related to the inability of the equipment to measure the correct value and it cannot be determined by repeating the measurement. Usually the bias uncertainty of the equipment is reported in its specification. The precision uncertainty can be estimated statistically by duplicating experimental runs. The total uncertainty ϵ_y is given by

$$\epsilon_y = \sqrt{\Sigma\epsilon_{y,B}^2 + \epsilon_{y,p}^2} \tag{C-1}$$

The precision uncertainty for experiments with *n* independent measurement is given as [1-3]

$$\epsilon_{y,p} = t_{(1-c)/2,\nu}\frac{S_y}{\sqrt{n}} \tag{C-2}$$

where c is the confidence limit, $\upsilon = n - 1$ is the number of degrees of freedom, S_y is the standard deviation of the samples, and $t_{\alpha/2,\nu}$ is a one-tailed t-distribution value which can be found in literature, e.g. Wheeler and Ganji [1] or Beckwith et al. [3].

Equation (C-1) is used to determine the uncertainty of parameters that are measured directly. For this purpose, moreover, select experiments are repeated at least three times. The largest S_y is used in calculations.

Using propagation of uncertainty methods, one can estimate the uncertainty in a variable by using the known uncertainties in other measured variables. The uncertainty in $f = f(x_1, \ldots x_N)$ is given by the following

$$\epsilon_f^2 = \sum_{i=1}^{N} \left(\frac{\partial f}{\partial x_i}\right)^2 \epsilon_i^2 \tag{C-3}$$

assuming that each uncertainty is small [3]. For instance, for the Froude number, defined as

$$Fr = \frac{u}{\sqrt{g'H}} \tag{C-4}$$

with u as the front speed, the propagation of uncertainty can be written as

$$\frac{\epsilon_{Fr}}{Fr} = \sqrt{\left(\frac{\epsilon_u}{u}\right)^2 + \frac{1}{4}\left(\frac{\epsilon_{g\prime}}{g'}\right)^2 + \frac{1}{4}\left(\frac{\epsilon_H}{H}\right)^2} \tag{C-5}$$

In our experiments $\epsilon_{g\prime,B}$ =0.007 ms^{-2}, and $\epsilon_{H,B}$ =0.5 mm. We estimate the front speed as the slope of the measured front position versus time. The bias uncertainty in the velocity is estimated by

$$\frac{\epsilon_{u,B}}{u} = \sqrt{\left(\frac{\epsilon_{x,B}}{x}\right)^2 + \left(\frac{\epsilon_{t,B}}{t}\right)^2} \tag{C-6}$$

with x and t as the measured horizontal position of the first front and time, respectively. From our measured data, we assume $\epsilon_{t,B}$~0. Regarding the bias uncertainty of the measured position, the pixel-to-length calibration error is estimated as $\epsilon_{x,B}$ =0.79 mm.

There is also an error of regression associated with the curve fit described above, which is computed using [1]

$$S_{x,t} = \sqrt{\frac{\Sigma x_i^2 - b\Sigma x_i - a\Sigma x_i t_i}{m-2}} \tag{C-7}$$

where m is the number of processed images and $S_{x,t}$ is the standard fit error (also known as root mean squared error). Applying (C-7), we find that $S_{x,t}$ =2.9 mm for a typical experiment shown in Figure 2-9.

By repeating the experiments and using (C-2), the precision error can be found for each variable and then using (C-5) gives the precision error for the Froude number as $\epsilon_{Fr_1,p} = \pm 0.02$. By applying (C-1), the total uncertainty is therefore given by ϵ_{Fr_1}=$\pm$0.02. Not surprisingly, the total uncertainty is

dominated by the precision error due to the slight irregularities in the advance of the gravity current front (with $\epsilon_{Fr_1,B}$=±0.003). Moreover, the mean value is reported as the measured value.

Table C-1 lists the estimated uncertainty associated with key measured parameters in the present study.

Table C-1. Estimated uncertainty in various variables.

Parameter	(Maximum) Uncertainty
Fr_1	±0.02
Fr_2	±0.02
Fr_b	±0.04
$t_2\sqrt{\frac{g'}{H}}$	±6
$\Delta_{a,0}/g'$ or $\Delta_{a,c}/g'$	±0.0386
b_0 or b_c	±0.0392
h_b/H or h_t/H	±0.017
$t_E\sqrt{\frac{g'}{H}}$	±9

References

[1] Wheeler AJ, Ganji AR. Introduction to engineering experimentation. Prentice Hall; 1996.

[2] Taylor JR. An introduction to error analysis: The study of uncertainties in physical measurements. 2nd ed. University Science Books; 1997.

[3] Beckwith TG, Marangoni RD, Lienhard JHV. Mechanical measurements. 6th ed, Pearson Prentice Hall; 2007.

Appendix D

Mixing Exchange Flow Experimental Data Summary

Experimentally determined values for Fr_1, Fr_b, $t_2\sqrt{\frac{g'}{H}}$, $\frac{b_0^\infty}{b_{tot}(0)}$ and $\frac{b_c^\infty}{b_{tot}(0)}$ are presented in Table D-1 below. These data are used in Chapters 2 and 3. Individual stratification profiles are too numerous to present for each entry. Hence, select cases chosen so that they span a wide range of the experimental parameter space, and are presented in Chapters 2 and 3.

Table D- 1. Experimental data for the exchange flow of Chapters 2 and 3. Column labels are described in text.

$\frac{h}{H}$	$\frac{\ell}{L}$	$\frac{\rho_0}{\rho_c}$	$\frac{b_0^\infty}{b_{tot}(0)}$	$\frac{b_c^\infty}{b_{tot}(0)}$	Fr_1	Fr_b	$t_2\sqrt{\frac{g'}{H}}$	where (stratification profiles) located
0.12	0.27	1.0415	0.1225	0.8475	0.23	0.21	80	Fig. 3-11a
0.25	0.27	1.0408	0.1917	0.7994	0.29	0.28	54	Fig. 3-11b
0.38	0.27	1.0421	0.2323	0.7627	0.33	0.35	48	Fig. 3-11c
0.51	0.27	1.0407	0.2555	0.7448	0.43	0.39	43	Fig. 3-11d
0.63	0.27	1.0404	0.2684	0.7245	0.48	0.49	41	Fig. 3-11e

Continued on the next page ….

$\frac{h}{H}$	$\frac{\ell}{L}$	$\frac{\rho_0}{\rho_c}$	$\frac{b_0^{\infty}}{b_{tot}(0)}$	$\frac{b_c^{\infty}}{b_{tot}(0)}$	Fr_1	Fr_b	$t_2\sqrt{\frac{g'}{H}}$	where (stratification profiles) located
0.13	0.40	1.0417	0.1151	0.8801	0.24	0.20	61	
0.26	0.40	1.0411	0.2264	0.7676	0.27	0.23	49	Fig. 3-10a
0.38	0.40	1.0399	0.3216	0.6743	0.37	0.33	40	
0.51	0.40	1.0399	0.3714	0.6235	0.43	0.34	36	Fig. 3-10b
0.64	0.40	1.0409	0.4062	0.5918	0.45	0.35	34	
Continued on the next page ….								

$\frac{h}{H}$	$\frac{\ell}{L}$	$\frac{\rho_0}{\rho_c}$	$\frac{b_0^\infty}{b_{tot}(0)}$	$\frac{b_c^\infty}{b_{tot}(0)}$	Fr_1	Fr_b	$t_2\sqrt{\frac{g'}{H}}$	where (stratification profiles) located
0.13	0.50	1.0426	0.1211	0.8723	0.31	0.20	46	Fig. 2-12a
0.25	0.50	1.0420	0.2028	0.7924	0.34	0.29	39	Fig. 2-12b
0.38	0.50	1.0429	0.3361	0.6611	0.38	0.31	34	Fig. 2-12c
0.50	0.50	1.0421	0.4105	0.5823	0.43	0.32	30	
0.63	0.50	1.0410	0.4959	0.4989	0.46	0.35	29	
Continued on the next page ….								

$\frac{h}{H}$	$\frac{\ell}{L}$	$\frac{\rho_0}{\rho_c}$	$\frac{b_0^{\infty}}{b_{tot}(0)}$	$\frac{b_c^{\infty}}{b_{tot}(0)}$	Fr_1	Fr_b	$t_2\sqrt{\frac{g'}{H}}$	where (stratification profiles) located
0.75	0.50	1.0404	0.4952	0.4948	0.48	0.38	28	
0.88	0.50	1.0406	0.4945	0.5001	0.49	0.41	23	
0.14	0.61	1.0388	0.1224	0.8734	0.24	0.22	37	Fig. 3-10f
0.26	0.61	1.0400	0.2474	0.7508	0.30	0.28	30	
0.38	0.61	1.0397	0.3791	0.6187	0.33	0.31	27	
Continued on the next page ….								

$\frac{h}{H}$	$\frac{\ell}{L}$	$\frac{\rho_0}{\rho_c}$	$\frac{b_0^\infty}{b_{tot}(0)}$	$\frac{b_c^\infty}{b_{tot}(0)}$	Fr_1	Fr_b	$t_2\sqrt{\frac{g'}{H}}$	where (stratification profiles) located
0.50	0.61	1.0398	0.5035	0.4938	0.37	0.32	24	
0.63	0.61	1.0388	0.5472	0.4498	0.39	0.39	23	Fig. 3-10d
0.75	0.61	1.0417	0.6021	0.3949	0.42	0.37	21	
0.13	0.73	1.0414	0.1203	0.8744	0.19	0.17	29	Fig. 2-13a
0.27	0.73	1.0425	0.2609	0.7329	0.33	0.28	21	Fig. 2-13b
Continued on the next page ….								

$\frac{h}{H}$	$\frac{\ell}{L}$	$\frac{\rho_0}{\rho_c}$	$\frac{b_0^\infty}{b_{tot}(0)}$	$\frac{b_c^\infty}{b_{tot}(0)}$	Fr_1	Fr_b	$t_2\sqrt{\frac{g'}{H}}$	where (stratification profiles) located
0.37	0.73	1.0434	0.3788	0.6195	0.37	0.32	20	Fig. 2-13c
0.51	0.73	1.0394	0.5597	0.4398	0.41	0.32	18	Fig. 2-13d
0.63	0.73	1.0402	0.6473	0.3516	0.44	0.33	18	Fig. 2-13e
0.76	0.73	1.0341	0.7581	0.2408	0.45	0.41	15	

Appendix E

Displacement Exchange Flow Experimental Data Summary

Experimentally determined values for Fr_1, $t_2\sqrt{\frac{g'}{H}}$, $t_E\sqrt{\frac{g'}{H}}$, $\frac{b_0^\infty}{b_{tot}(0)}$ and $\frac{b_c^\infty}{b_{tot}(0)}$ are presented in Table E-1 below. These data are used in Chapter 4. Individual stratification profiles are too numerous to present for each entry. Hence, select cases chosen so that they span a wide range of the experimental parameter space, and are presented in Chapter 4.

Table E-1. Experimental data for the exchange flow of Chapter 4. Column labels are described in text.

N_b	N_t	$\frac{\rho_0}{\rho_c}$	$\frac{b_0^\infty}{b_{tot}(0)}$	$\frac{b_c^\infty}{b_{tot}(0)}$	$t_E\sqrt{\frac{g'}{H}}$	$t_2\sqrt{\frac{g'}{H}}$	Π_s	where (stratification profiles) located
1	1	1.0405	0.5027	0.5177	486	47	0.05	
1	1	1.0414	0.5050	0.5259	480	44	0.10	Fig. 4-14
1	1	1.0414	0.5474	0.5682	478	43	0.29	Fig. 4-15
1	2	1.0407	0.4992	0.5280	398	45	0.05	
1	3	1.0403	0.4998	0.5191	335	45	0.05	

Continued on the next page ….

N_b	N_t	$\frac{\rho_0}{\rho_c}$	$\frac{b_0^\infty}{b_{tot}(0)}$	$\frac{b_c^\infty}{b_{tot}(0)}$	$t_E\sqrt{\frac{g'}{H}}$	$t_2\sqrt{\frac{g'}{H}}$	Π_s	where (stratification profiles) located
2	1	1.0413	0.5035	0.5301	384	40	0.05	
2	2	1.0409	0.4984	0.5151	243	33	0.05	
2	3	1.0406	0.4992	0.5301	199	33	0.05	
3	1	1.0407	0.4998	0.5191	364	37	0.05	
3	2	1.0421	0.5085	0.5203	209	35	0.05	
Continued on the next page ….								

N_b	N_t	$\frac{\rho_0}{\rho_c}$	$\frac{b_0^\infty}{b_{tot}(0)}$	$\frac{b_c^\infty}{b_{tot}(0)}$	$t_E\sqrt{\frac{g'}{H}}$	$t_2\sqrt{\frac{g'}{H}}$	Π_s	where (stratification profiles) located
3	3	1.0397	0.4877	0.5024	150	29	0.01	Fig. 4-13
3	3	1.0405	0.4921	0.5159	155	31	0.05	
3	3	1.0408	0.5136	0.5398	150	35	0.10	Fig. 4-13
3	3	1.0425	0.5590	0.5892	146	31	0.29	Fig. 4-15

Appendix F

Technical drawings for the nozzle used in the experiments of Chapter 4

The drawing of the line-plume nozzle (including dimensions) fabricated by rapid prototyping is presented in this appendix.

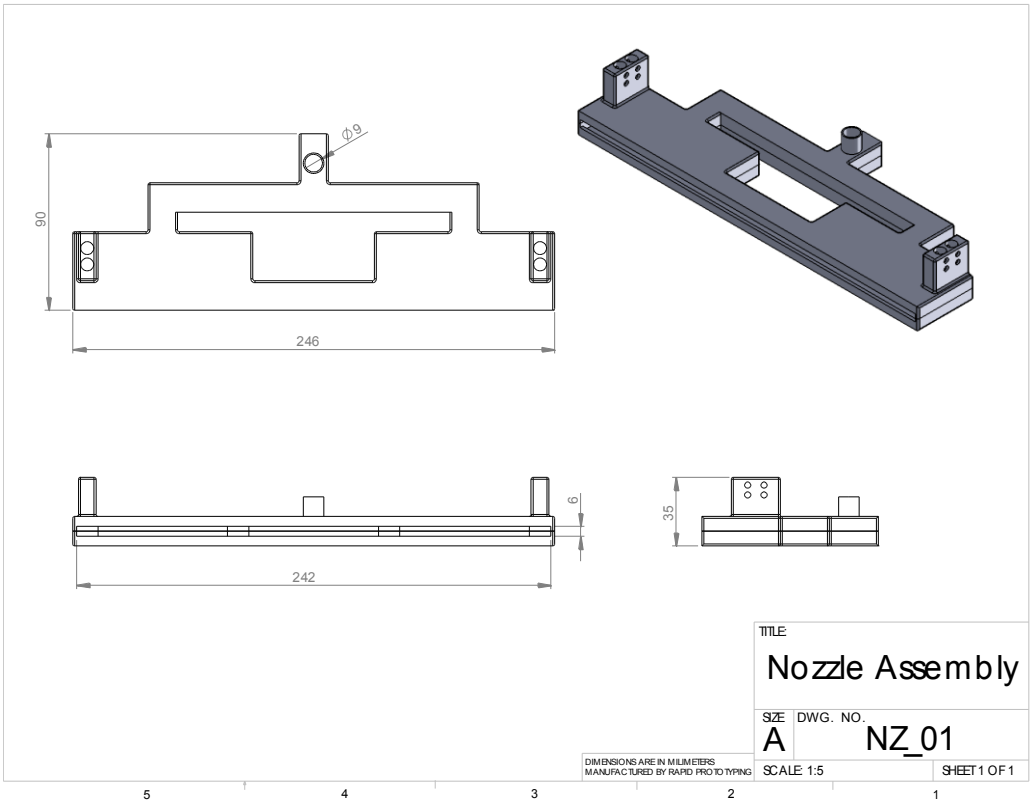

Figure F-1. Isometric, top, front and side views of the nozzle.

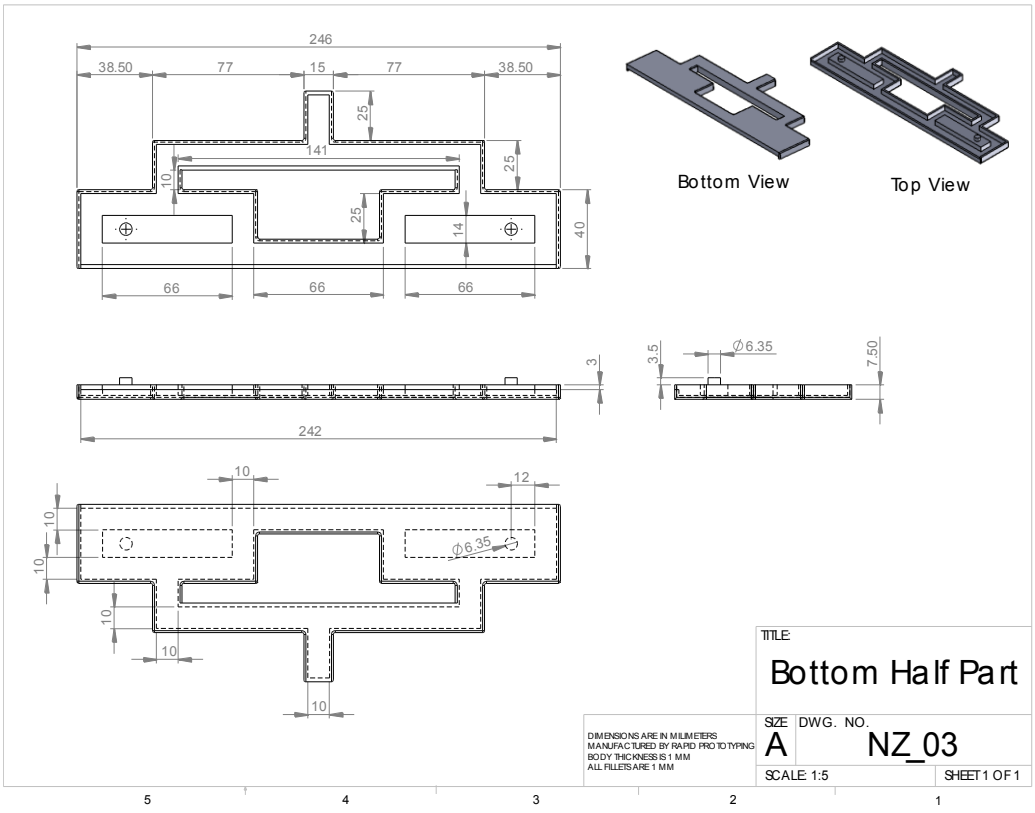

Figure F-2. Isometric, top, front, bottom and side views of the nozzle parts fabricated separately by rapid prototyping.

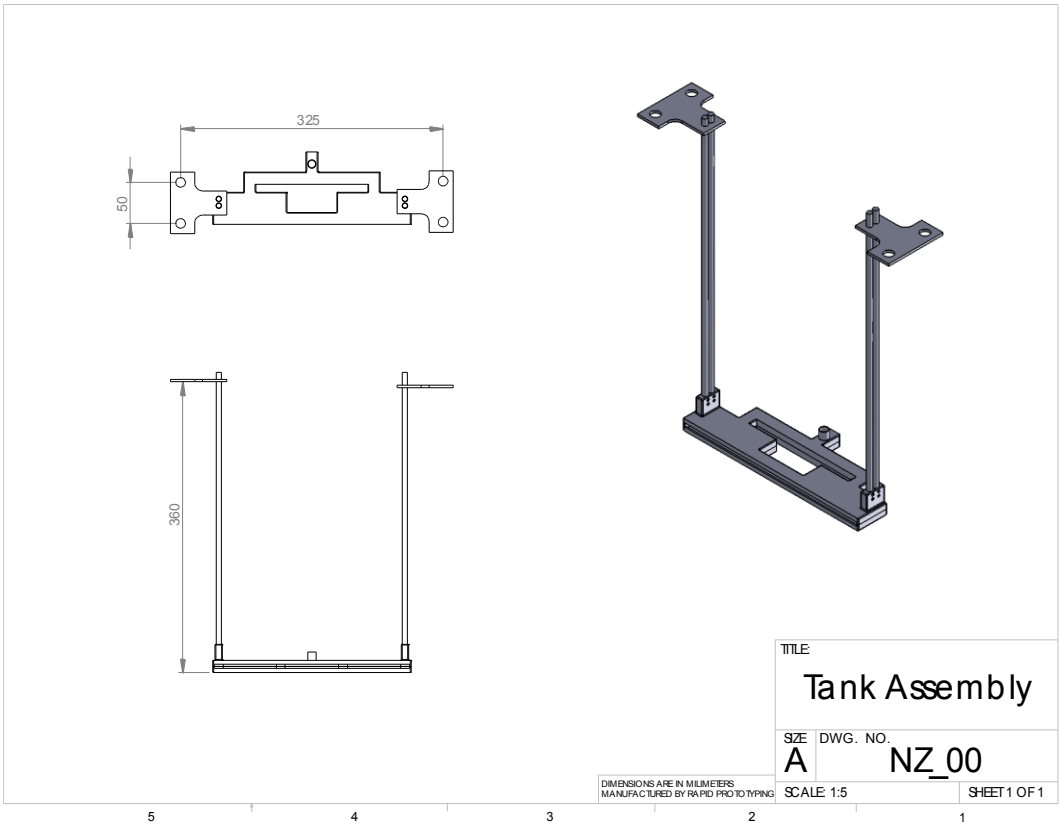

Figure F-3. Isometric, top and front views of the nozzle assembled with the supports.

References

[1] http://www.statcan.gc.ca/pub/16-002-x/2008004/article/10749-eng.htm

[2] Santamouris M. Energy in the urban built environment: The role of natural ventilation. Earthscan, 2005.

[3] CMHC, 2004. Analysis of ventilation system performance in new Ontario houses. Technical Series 04-117, Canada Mortgage and Housing Corporation.

[4] Spengler JD, Sexton K. Indoor air pollution: A public health perspective. Science, 1983;221:9–17.

[5] Heiselberg P, Svidt K, Nielsen PV. Characteristics of airflow from open windows. Build Environ 2001;36(7): 859-869.

[6] Torcellini P, Pless S, Deru M, Crawley D. Zero Energy Buildings: A Critical Look at the Definition. ACEEE Summer Stud, Pacific Grove, California, USA (2006).

[7] Parker DS. Very low energy homes in the United States: Perspectives on performance from measured data. Energ Build, 2009;41:512–520.

[8] Chen Y, Athienitis AK, Galal K. Modeling, design and thermal performance of a BIPV/T system thermally coupled with a ventilated concrete slab in a low energy solar house: Part 1, BIPV/T system and house energy concept. Solar Energy 2011;84:1892-1907.

[9] Linden P. The fluid mechanics of natural ventilation. Annu Rev Fluid Mech, 1999;31:201–238.

[10] Liu PC, Lin HT, Chou JH. Evaluation of buoyancy-driven ventilation in atrium buildings using computational fluid dynamics and reduced-scale air model. J Fluid Mech, 2009;44:1970-1979.

[11] Linden PF, Lane-serff GF, Smeed DA. Emptying filling boxes: the fluid mechanics of natural ventilation. J Fluid Mech 1990;212:309-335.

[12] Fang L, Clausen G, Fanger PO, Impact of temperature and humidity on the perception of indoor air quality, Indoor Air 1998;8:80–90.

[13] Fang L, Clausen G, Fanger PO, Impact of temperature and humidity on chemical and sensory emissions from buildings materials, Indoor Air 1999;9:193–201.

[14] Melikov AK, Cermak R, Majer M, Maele K. Personalized ventilation: evaluation of different air terminal devices. Energ and Build 2002;34:829–836.

[15] Caulfield CP, Woods W. The mixing in a room by localized finite-mass-flux source of buoyancy. J Fluid Mech 2002;471:33-50.

[16] Merci B, Maele K. Numerical simulations of full-scale enclosure fires in a small compartment with natural roof ventilation. Fire Safety J 2008;43:495-511.

[17] Baines WD, Turner JS. Turbulent buoyant convection from a source in a confined region. J Fluid Mech 1969;37:51-80.

[18] Roony GG, Linden PF. Similarity considerations for non-Boussinesq plumes in un-stratified environment. J Fluid Mech, 1996;318:237–50.

[19] Morton BR, Taylor GI, Turner JS. Turbulent gravitational convection from maintained and instantaneous sources. J Fluid Mech 1956;234:1-23.

[20] Worster MG, Huppert HE. Time-dependent density profiles in a filling box. J Fluid Mech, 1983;132:457–466.

[21] Germeles AE. Forced plumes and mixing of liquids in tanks. J Fluid Mech 1975;71:601-623.

[22] Kuesters AS, Woods W. The formation and evolution of stratification during transient mixing ventilation. J Fluid Mech 2010;670:66-84.

[23] Lin YJP, Linden PF. Buoyancy-driven ventilation between two chambers. J Fluid Mech, 2002;463:293–312.

[24] Benjamin TB. Gravity currents and related phenomena. J Fluid Mech 1968;31:209-248.

[25] Klemp JB, Rotunno R, Skamarock WC. On the propagation of internal bores. J Fluid Mech 1997;331:81-106.

[26] Chen Q. Ventilation performance prediction for buildings: A method overview and recent applications. Build Environ 2009;44:848-858.

[27] Sandberg H, Lindstrom S. A model for ventilation by displacement. Proc. Roomvent'87, Stockholm, Sweden.

[28] Sandberg H, Lindstrom S. Stratified flow in ventilated rooms—a model study. Proc. Roomvent'90, Oslo, Norway.

[29] Linden PF, Cooper P. Multiple sources of buoyancy in a naturally ventilated enclosure. J Fluid Mech, 1996;311:177–92

[30] Caulfield CP. Stratification and buoyancy in geophysical flows. PhD thesis. Cambridge Univ., UK, 1991.

[31] Kaye NB, Hunt GR. Time-dependent flows in an emptying filling box. J Fluid Mech, 2004;520:135-156.

[32] Gorton RL, Sassi MM. Determination of temperature profiles in a thermally stratified air-conditioned system: Part 2. Program description and comparison of computed and measured results. Trans. ASHRAE, 1982;88(2), paper 2701.

[33] Jacobsen J. Thermal climate and air exchange rate in a glass covered atrium without mechanical ventilation related to simulations. 13th Natl. Solar Conf. MIT, Cambridge, MA, 1988,4:61–71.

[34] Cooper P, Mak N. Thermal stratification and ventilation in atria. Proc. ANZSES Conf., Adelaide, Australia, 1991:pp. 385–91.

[35] Shrinivas AB, Hunt GR. Transient ventilation dynamics induced by heat sources of unequal strength. J Fluid Mech, 2014;738:34-64.

[36] Brown WG, Solvason KR. Natural convection heat transfer through rectangular openings in partitions-I. Int J Heat Mass Transf 1962a;5:859–68.

[37] Brown WG, Solvason KR. Natural convection heat transfer through rectangular openings in partitions-II. Int J Heat Mass Transf 1962b;5:869–78.

[38] Shaw BH, Whyte W. Air movement through doorways—the influence of temperature and its control by forced airflow. J Inst Heat Vent Eng 1974;42:210–18.

[39] Linden PF, Simpson JE. Buoyancy driven flows through an open door. Air Infiltration Rev. 1985;6:4–5.

[40] Dalziel SB, Lane-serff G. The hydraulics of doorway exchange. Build Environ 1991;26:2:121-35.

[41] Chenvidyakarna T, Woods A. Multiple steady states in stack ventilation. Build Environ 2005;40:399–410.

[42] Fitzgerald SD, Woods A. On the transition from displacement to mixing ventilation with a localised heat source. Build Environ 2007;42:2210–2217.

[43] Coffey CJ, Hunt GR. Ventilation effectiveness measures based on heat removal: part 2. Application to natural ventilation flows. Build Environ 2007;42(6):2249–62.

[44] Hunt GR, Coffey CJ. Emptying boxes – classifying transient natural ventilation flows. J Fluid Mech 2010; 646:137–168.

[45] Holford JM, Woods AW. On the thermal buffering of naturally ventilated buildings through internal thermal mass. J Fluid Mech, 2007;580:3–29.

[46] Bassiouny R, Koura NSA. An analytical and numerical study of solar chimney use for room natural ventilation. Energ Buildings, 2008;40(5):865–73.

[47] Bolster DT, Linden PF. Particle transport in low-energy ventilation systems. Part 1: theory of steady states. Indoor Air 2009; 19: 122–129.

[48] Bolster DT, Linden PF. Particle transport in low-energy ventilation systems. Part 2: Transients and experiments. Indoor Air 2009; 19: 130–144.

[49] Shearer D, Porteous CDA. Winter performance of 2-storey solar buffer spaces in Glasgow demonstration houses. EuroSun 2012.

[50] Mottard JM, Fissore A. Thermal simulation of an attached sunspace and its experimental validation. Sol Energ 2007; 81: 305-315.

[51] Oliveti G, Arcuri N, De Simone M, Bruno R. Solar heat gains and operative temperature in attached sunspaces. Renew. Energy 2012, 39, 241–249.

[52] Stathopoulou OI, Assimakopoulos VD, Flocas HA, Helmis CG. An experimental study of air quality inside large athletic halls. Build Environ 2008;43:834–48.

[53] Baker N, Linden PF. Physical modelling of airflows—a newdesign tool. Atrium Build Archit Eng a991;13–22, Ed. F. Mills. CICC Publications, Welwyn, England

[54] Lane-Serff GF. Heat flow and air movement in buildings. PhD thesis, University of Cambridge, UK 1989.

[55] Kaye NB, Flynn MR, Cook MJ, Ji Y. The role of diffusion on the interface thickness in a ventilated filling box. J Fluid Mech 2010;652:195-205.

[56] Howell SA, Potts I. On the natural displacement flow through a full-scale enclosure and the importance of the radiative participation of the water vapour content of the ambient air. Build Environ 2002;37: 817–823.
[57] Zhang Z, Chen X, Mazumdar S, Zhang T, Chen Q. Experimental and numerical investigation of airflow and contaminant transport in an airliner cabin mockup. Build Environ 2009;44(1):85–94.
[58] Melikov AK, Popiolek Z, Silva MCG, Care I, Sefker T. Accuracy limitations for low-velocity measurements and draft assessment in rooms. HVAC&R Research 2007;13(6):971–86.
[59] Batchelor GK, Heat convection and buoyancy effects in fluids. Quart J Roy Met Soc, 1956;80:339-358.
[60] Rottman JW, Linden PF. Gravity Currents. In: Grimshaw R, editor. Environmental stratified flows. Dordrecht: Kluwer Academic Publishers; 2003, p. 89-118.
[61] Chenvidyakarn T, Woods A. Stratification and oscillations produced by precooling during transient natural ventilation. Build Environ 2007;42(1):99–112.
[62] Livermore SR, Woods AW. Natural ventilation of a building with heating at multiple levels. Build Environ 2007;42(3):1417–30.
[63] Morsing S, Strøm JS, Zhang G, Kai P. Scale model experiments to determine the effects of internal airflow and floor design on gaseous emissions from animal houses. Biosyst Eng 2008;99(1):99–104.
[64] Phillips JC, Woods AW. On ventilation of a heated room through a single doorway. Build Environ 2004;39:241-253.
[65] Mott RW, Woods AW. Quasi-steady states in natural displacement ventilation driven by periodic gusting of wind. J Fluid Mech 2012;707:1-23.
[66] Fitzgerald SD, Woods AW. Transient natural ventilation of a room with a distributed heat source. J Fluid Mech 2007;591:21–42.
[67] Norton T, Sun DW. Computational fluid dynamics (CFD) – an effective and efficient design and analysis tool for the food industry: a review. Trends Food Sci Tech 2006;17:600–20.

[68] http://www.ansys.com/Products/Simulation+Technology/Fluid+Dynamics/Fluid+ Dynamics+Products/ANSYS+Fluent

[69] http://www.ansys.com/Products/Simulation+Technology/Fluid+Dynamics/Fluid+ Dynamics+Products/ANSYS+CFX

[70] Abantoa J, Barreroa D, Reggioa M, Ozella B. Air flow modelling in a computer room. Build Environ 2004;39:1393–1402.

[71] Pope SB. Turbulent flows. Cambridge University Press; 2000.

[72] Launder BE, Spalding DB. The numerical computation of turbulent flows. Comput Method Appl Mech Eng1974;3:269–89.

[73] Yakhot V, Orszag SA. Renormalization group analysis of turbulence. J Sci Comp 1986;1(1):3–51.

[74] Maele K, Merci B. Application of RANS and LES field simulations to predict the critical ventilation velocity in longitudinally ventilated horizontal tunnels. Fire Safety J 2008;43(8):598-609.

[75] Hu CH, Ohba M, Yoshie R. CFD modelling of unsteady cross ventilation flows using LES. J Wind Eng Indust Aero 2008;96 (10-11):1692-1706.

[76] Zhai Z, Zhang Z, ZhangW, Chen Q. Evaluation of various turbulence models in predicting airflow and turbulence in enclosed environments by CFD: part 1 – summary of prevalent turbulence models. HVAC&R Research 2007;13(6):853–70.

[77] Chung W, Devaud CB. Buoyancy-corrected k–ε models and large eddy simulation applied to a large axisymmetric helium plume. Int J Numer Meth Fluids 2008; 58:57–89.

[78] Versteeg HK, Malalasekera W. An Introduction to Computational Fluid Dynamics: The Finite Volume Method. McGraw-Hill, 1st edition, 1995.

[79] Amsallem D, Cortial J, Farhat C. Toward Real-Time Computational-Fluid-Dynamics-Based Aeroelastic Computations Using a Database of Reduced-Order Information. AIAA JOURNAL 2010; 48(9):2029–2037.

[80] Malkawi AM, Srinivasan RS. A new paradigm for Human-Building Interaction: the use of CFD and Augmented Reality. Automat Constr 2005; 14:71–84.

[81] Nabi S, Flynn MR. The hydraulics of exchange flow between adjacent confined building zones. Build Environ 2013;59:76-90.

[82] Nabi S, Flynn MR. Influence of geometric parameters on the eventual buoyancy stratification that develops due to architectural exchange flow. Build Environ 2014;71:33-46.

[83] Hunt GR, Van den Bremer TS. Classical plume theory: 1937–2010 and beyond. IMA J Appl Math 2011;76:424-448.

[84] Sandbach SD, Lane-Serff GF. Transient buoyancy-driven ventilation: Part 1. Modelling advection. Build Environ 2011;46:1578-1588.

[85] Mingotti N, Chenvidyakarn T, Woods AW. The fluid mechanics of the natural ventilation of a narrow-cavity double-skin facade. Build Environ 2011;46:807-823.

[86] Kaye NB, Flynn MR, Cook MJ, Ji Y. The role of diffusion on the interface thickness in a ventilated filling box. J Fluid Mech 2010;652:195-205.

[87] Merci B, Maele K. Numerical simulations of full-scale enclosure fires in a small compartment with natural roof ventilation. Fire Safety J 2008;43:495-511.

[88] Linden PF, Lane-serff GF, Smeed DA. Emptying filling boxes: the fluid mechanics of natural ventilation. J Fluid Mech 1990;212:309-335.

[89] Baines WD, Turner JS. Turbulent buoyant convection from a source in a confined region. J Fluid Mech 1969;37:51-80.

[90] Phillips JC, Woods AW. On ventilation of a heated room through a single doorway. Build Environ 2004;39:241-253.

[91] Caulfield CP, Woods W. The mixing in a room by localized finite-mass-flux source of buoyancy. J Fluid Mech 2002;471:33-50.

[92] Kuesters AS, Woods W. The formation and evolution of stratification during transient mixing ventilation. J Fluid Mech 2010;670:66-84.

[93] Germeles AE. Forced plumes and mixing of liquids in tanks. J Fluid Mech 1975;71:601-623.

[94] Benjamin TB. Gravity currents and related phenomena. J Fluid Mech 1968;31:209-248.

[95] Shin JO, Dalziel SB, Linden PF. Gravity currents produced by lock exchange. J Fluid Mech 2004;521:1-34.

[96] Klemp JB, Rotunno R, Skamarock WC. On the propagation of internal bores. J Fluid Mech 1997;331:81-106.

[97] Dalziel SB. Two-layer hydraulics: a functional approach. J Fluid Mech 1991;223:135-163.

[98] Dalziel SB, Lane-serff G. The hydraulics of doorway exchange. Build Environ 1991;26:2:121-35.

[99] Wilson DJ, Kiel DE. Gravity driven counter flow through an open door in a sealed room. Build Environ 1990;25:379-388.

[100] Holford JM, Hunt GR. The dependence of the discharge coefficient on density contrast - experimental measurements. 14th Australian Fluid Mechanics Conference, Adelaide University, Adelaide, Australia, 2001.

[101] Hunt GR, Kaye NG. Virtual origin correction for lazy turbulent plumes. J Fluid Mech 2001;435:377-396.

[102] Simpson JE. Gravity Currents: in the environment and the laboratory.2nd ed. Cambridge University Press;1999.

[103] Yih CS, Guha CR. Hydraulic jump in a fluid system of two layers. Tellus 1955;7:358-366.

[104] Wood IR, Simpson JE. Jumps in layered miscible fluids. J Fluid Mech 1984;140:329-342.

[105] Morton BR, Taylor GI, Turner JS. Turbulent gravitational convection from maintained and instantaneous sources. J Fluid Mech 1956;234:1-23.

[106] Kotsovinos NE. A study of the entrainment and turbulence in a plane buoyant jet. Report No. KH-R-32, California Institute of Technology, Keck Laboratory, Pasadena, Calif., Aug., 1975.

[107] Rouse H, Yih C, Humphreys H. Gravitational convection from a boundary source. Tellus 1952;4:200-210.

[108] Killworth PD, Turner JS. Plumes with time-varying buoyancy in a confined region. Geophys Astro Fluid 1982;20 (3-4):265-291.

[109] Bolster D, Caulfield CP. Transients in natural ventilation-A time-periodically- varying source. Building Serv Eng Res Technol2008;29,2:119-135.
[110] Linden P. The fluid mechanics of natural ventilation. Annu Rev Fluid Mech 1999;31:201-238, 1999.
[111] Tatcher TL, Wilson DJ, Wood EE, Craig MJ, Sextro RG. Pollutant dispersion in a large indoor space: Part 1 – Scaled experiments using a water-filled model with occupants and furniture. Indoor Air 2004;14: 258–271.
[112] Taylor JR. An introduction to error analysis: The study of uncertainties in physical measurements. 2nd ed. University Science Books; 1997.
[113] Lowe RJ, Linden PF, Rottman JW. A laboratory study of the velocity structure in an intrusive gravity current. J Fluid Mech 2000;456:33-48.
[114] Huppert HE, Simpson JE. The slumping of gravity currents. J Fluid Mech 1980;99:785-799.
[115] Rottman JW, Linden PF. Gravity Currents. In: Grimshaw R, editor. Environmental stratified flows. Dordrecht: Kluwer Academic Publishers; 2003, p. 89-118.
[116] Lane-Serff, GF, Linden PF, Hillel M. Forced angled plumes. J Haz Mat 1993;33:75-99.
[117] U.S. Department of Energy. http://apps1.eere.energy.gov/ buildings/ publications/ pdfs/ corporate/ bt_stateindustry.pdf.
[118] ENERGY STAR®. http://www.energystar.gov/ia/business/challenge/ learn_more/ FastFacts.pdf.
[119] Linden PF. The fluid mechanics of natural ventilation. Annu Rev Fluid Mech 1999;31:201-238, 1999.
[120] Parker DS. Very low energy homes in the United States: Perspectives on performance from measured data. Energ Buildings 2009;41:512–520.
[121] Parameshwarana R, Kalaiselvamb S, Harikrishnanb S, Elayaperumala A. Sustainable thermal energy storage technologies for buildings: A review. Renew Sust Energ Rev 2012;16: 2394–2433.
[122] Shearer D, Porteous CDA. Winter performance of 2-storey solar buffer spaces in Glasgow demonstration houses. EuroSun 2012.

[123] Heim D. Isothermal storage of solar energy in building construction. Renewable Energy 2010;35:788–96.

[124] Nabi S, Flynn MR. Architectural Exchange Flows and Their Influence on Interior Temperature Stratification and Building Ventilation, Clima 2013 : 11th REHVA World Congress and 8th International Conference on IAQVEC, Prague, Czech Republic, June 2013.

[125] Nabi S, Flynn MR. The hydraulics of exchange flow between adjacent confined building zones. Build Environ 2013;59:76-90.

[126] Sandbach SD, Lane-Serff GF. Transient buoyancy-driven ventilation: Part 2. Modelling heat transfer. Building and Environment 2011;46(8):1589e99.

[127] Chen Q. Ventilation performance prediction for buildings: A method overview and recent applications. Build Environ 2009;44:848-858.

[128] Sandbach SD, Lane-Serff GF. Transient buoyancy-driven ventilation: Part 1. Modelling advection. Build Environ 2011;46:1578-1588.

[129] Mingotti N, Chenvidyakarn T, Woods AW. The fluid mechanics of the natural ventilation of a narrow-cavity double-skin facade. Build Environ 2011;46:807-823.

[130] Kaye NB, Flynn MR, Cook MJ, Ji Y. The role of diffusion on the interface thickness in a ventilated filling box. J Fluid Mech 2010;652:195-205.

[131] Merci B, Maele K. Numerical simulations of full-scale enclosure fires in a small compartment with natural roof ventilation. Fire Safety J 2008;43:495-511.

[132] Linden PF, Lane-serff GF, Smeed DA. Emptying filling boxes: the fluid mechanics of natural ventilation. J Fluid Mech 1990;212:309-335.

[133] Caulfield CP, Woods W. The mixing in a room by localized finite-mass-flux source of buoyancy. J Fluid Mech 2002;471:33-50.

[134] Kuesters AS, Woods W. The formation and evolution of stratification during transient mixing ventilation. J Fluid Mech 2010;670:66-84.

[135] Bolster D, Caulfield CP. Transients in natural ventilation-A time-periodically- varying source. Building Serv Eng Res Technol 2008;29,2:119-135.

[136] Baines WD, Turner JS. Turbulent buoyant convection from a source in a confined region. J Fluid Mech 1969;37:51-80.

[137] Morton BR, Taylor GI, Turner JS. Turbulent gravitational convection from maintained and instantaneous sources. J Fluid Mech 1956;234:1-23.

[138] Dalziel SB, Lane-serff G. The hydraulics of doorway exchange. Build Environ 1991;26:2:121-35.

[139] Benjamin TB. Gravity currents and related phenomena. J Fluid Mech 1968;31:209-248.

[140] Klemp JB, Rotunno R, Skamarock WC. On the propagation of internal bores. J Fluid Mech 1997;331:81-106.

[141] Rottman JW, Simpson JE. Gravity currents produced by instantaneous releases of a heavy fluid in a rectangular channel. J Fluid Mech 1983;135:95-110.

[142] Rouse H, Yih C, Humphreys H. Gravitational convection from a boundary source. Tellus 1952;4:200-210.

[143] Dalziel SB. Two-layer hydraulics: a functional approach. J Fluid Mech 1991;223:135-163.

[144] Holford JM, Hunt GR. The dependence of the discharge coefficient on density contrast - experimental measurements. 14th Australian Fluid Mechanics Conference, Adelaide University, Adelaide, Australia, 2001.

[145] Wilson DJ, Kiel DE. Gravity driven counter flow through an open door in a sealed room. Build Environ 1990;25:379-388.

[146] Germeles AE. Forced plumes and mixing of liquids in tanks. J Fluid Mech 1975;71:601-623.

[147] Tatcher TL, Wilson DJ, Wood EE, Craig MJ, Sextro RG. Pollutant dispersion in a large indoor space: part 1-scaled experiments using a water-filled model with occupants and furniture. Indoor Air 2004;14:258e71.

[148] Taylor JR. An introduction to error analysis: The study of uncertainties in physical measurements. 2nd ed. University Science Books; 1997.

[149] ANSI/ASHRAE Standard 55-2010, Thermal Environmental Conditions for Human Occupancy.

[150] Hunt GR, Van den Bremer TS. Classical plume theory: 1937–2010 and beyond. IMA J Appl Math 2011;76:424-448.

[151] Sandbach SD, Lane-Serff GF. Transient buoyancy-driven ventilation: Part 1. Modelling advection. Build Environ 2011;46:1578-1588.

[152] Mingotti N, Chenvidyakarn T, Woods AW. The fluid mechanics of the natural ventilation of a narrow-cavity double-skin facade. Build Environ 2011;46:807-823.

[153] Kaye NB, Flynn MR, Cook MJ, Ji Y. The role of diffusion on the interface thickness in a ventilated filling box. J Fluid Mech 2010;652:195-205.

[154] Merci B, Maele K. Numerical simulations of full-scale enclosure fires in a small compartment with natural roof ventilation. Fire Safety J 2008;43:495-511.

[155] Linden PF, Lane-serff GF, Smeed DA. Emptying filling boxes: the fluid mechanics of natural ventilation. J Fluid Mech 1990;212:309-335.

[156] Phillips JC, Woods AW. On ventilation of a heated room through a single doorway. Build Environ 2004;39:241-253.

[157] Caulfield CP, Woods W. The mixing in a room by localized finite-mass-flux source of buoyancy. J Fluid Mech 2002;471:33-50.

[158] Kuesters AS, Woods W. The formation and evolution of stratification during transient mixing ventilation. J Fluid Mech 2010;670:66-84.

[159] Nabi S, Flynn MR. The hydraulics of exchange flow between adjacent confined building zones. Build Environ 2013;59:76-90.

[160] Nabi S, Flynn MR. Influence of geometric parameters on the eventual buoyancy stratification that develops due to architectural exchange flow. Build Environ 2014;71:33-46.

[161] Gladstone C, Woods AW. On buoyancy-driven natural ventilation of a room with a heated floor. J Fluid Mech 2001;441:293–314.

[162] Kaye NG, Hunt GR. The effect of floor heat source area on the induced airflow in a room. Build Environ 2010;45:839–847.

[163] Kaye NG, Hunt GR. Time-dependent flows in an emptying filling box. J Fluid Mech 2004;520:135-156.

[164] Baines WD, Turner JS. Turbulent buoyant convection from a source in a confined region. J Fluid Mech 1969;37:51-80.

[165] Killworth PD, Turner JS. Plumes with time-varying buoyancy in a confined region. Geophys Astro Fluid 1982;20 (3-4):265-291.

[166] Morton BR, Taylor GI, Turner JS. Turbulent gravitational convection from maintained and instantaneous sources. J Fluid Mech 1956;234:1-23.

[167] Germeles AE. Forced plumes and mixing of liquids in tanks. J Fluid Mech 1975;71:601-623.

[168] Wong ABD, Griffiths RW. Stratification and convection produced by multiple turbulent plumes. Dynam. Atmos Ocean 1999;30:101-123.

[169] Tatcher TL, Wilson DJ, Wood EE, Craig MJ, Sextro RG. Pollutant dispersion in a large indoor space: Part 1 – Scaled experiments using a water-filled model with occupants and furniture. Indoor Air 2004;14: 258–271.

[170] Hunt GR, Kaye NG. Virtual origin correction for lazy turbulent plumes. J Fluid Mech 2001;435:377-396.

[171] Taylor JR. An introduction to error analysis: The study of uncertainties in physical measurements. 2nd ed. University Science Books; 1997.

[172] Kotsovinons NE. A study of the entrainment and turbulence in a plane buoyant jet. Report No. KH-R-32, California Institute of Technology, Keck Laboratory, Pasadena, Calif., Aug., 1975.

[173] Rouse H, Yih C, Humphreys H. Gravitational convection from a boundary source. Tellus 1952;4:200-210.

[174] ASHRAE Handbook of fundamentals. Chapter 15: Fenestration. New York: The American Society of Heating Refrigeration and Air Conditioning Engineers; 2009. p. 15.1–21.

[175] Online solar gain calculator: http://www.susdesign.com/windowheatgain/ (source: US Geological Survey. http://www.usgs.gov/)

[176] Rooney GG, Linden PF. Strongly Buoyant Plume Similarity and 'Small-fire' Ventilation. Fire Safe J 1997;29:235-258.

[177] Dalziel SB. Two-layer hydraulics: a functional approach. J Fluid Mech 1991;223:135-163.

[178] Dalziel SB, Lane-serff G. The hydraulics of doorway exchange. Build Environ 1991;26:2:121-35.

[179] Baines WD, Turner JS. Turbulent buoyant convection from a source in a confined region. J Fluid Mech 1969;37:51-80.

[180] Torcellini P, Pless S, Deru M, Crawley D. Zero Energy Buildings: A Critical Look at the Definition. ACEEE Summer Stud, Pacific Grove, California, USA (2006).

[181] Killworth PD, Turner JS. Plumes with time-varying buoyancy in a confined region. Geophys Astro Fluid 1982;20 (3-4):265-291.

[182] Bolster D, Caulfield CP. Transients in natural ventilation-A time-periodically- varying source. Building Serv Eng Res Technol2008;29,2:119-135.

[183] Lin YJP, Linden PF. The entrainment due to a turbulent fountain at a density interface. J Fluid Mech 2005;542:25-52.

[184] Germeles AE. Forced plumes and mixing of liquids in tanks. J Fluid Mech 1975;71:601-623.

[185] Shrinivas AB, Hunt GR. Transient ventilation dynamics induced by heat sources of unequal strength. J Fluid Mech, 2014;738:34-64.

[186] Bauman F and Webster T. Outlook for underfloor air distribution. ASHRAE J 2001;43(6):18-27.

[187] Karlsson B, Quintiere JG. Enclosure Fire Dynamics. CRC Press, 2000.

[188] Rooney GG, Linden PF. Strongly Buoyant Plume Similarity and 'Small-fire' Ventilation. Fire Safe J 1997;29:235-258.

[189] Batchelor, GK. Heat convection and buoyancy effects in fluids. Quart J Roy Met Soc. 1954;80:339-358.

[190] Linden P. The fluid mechanics of natural ventilation. Annu Rev Fluid Mech, 1999;31:201–238.

[191] Morton BR, Taylor GI, Turner JS. Turbulent gravitational convection from maintained and instantaneous sources. J Fluid Mech 1956;234:1-23.

[192] Baines WD, Turner JS. Turbulent buoyant convection from a source in a confined region. J Fluid Mech 1969;37:51-80.

[193] Germeles AE. Forced plumes and mixing of liquids in tanks. J Fluid Mech 1975;71:601-623.

[194] Caulfield CP, Woods W. The mixing in a room by localized finite-mass-flux source of buoyancy. J Fluid Mech 2002;471:33-50.

[195] Kaye NB, Hunt GR. Time-dependent flows in an emptying filling box. J Fluid Mech, 2004;520:135-156.

[196] Kotsovinos NE, List EJ. Plane turbulent buoyant jets. Part 1. Integral properties. J Fluid Mech 1977;81:25-44.

[197] Hunt GR, Van den Bremer TS. Classical plume theory: 1937–2010 and beyond. IMA J Appl Math 2011;76:424-448.

[198] Fan LN, Brooks H. 1969 Numerical solutions of turbulent buoyant jet problems. W. M. Keclc Lab. of Hydraulics and Water Resources, Calij. Inst. Tech. Rep. KH-R-18.

[199] Spiegel EA, Veronis G. On the Boussinesq Approximation for a Compressible fluid. Astrophys J, 1960;131:442-447.

[200] Grey DD, Giorcini A. The validity of the Boussinesq approximation for liquids and gases. Int J Hear Mass Transfer, 1975;19:545-551.

[201] Wheeler AJ, Ganji AR. Introduction to engineering experimentation. Prentice Hall; 1996.

[202] Taylor JR. An introduction to error analysis: The study of uncertainties in physical measurements. 2nd ed. University Science Books; 1997.

[203] Beckwith TG, Marangoni RD, Lienhard JHV. Mechanical measurements. 6th ed, Pearson Prentice Hall; 2007.